NONLINEAR CORRECTION OF SPECTRALLY RECOVERED, RF SPECTRAL FEATURES, READOUT WITH HIGH FREQUENCY-CHIRPED LASER FIELDS

by

Louis Joseph Oberto

A thesis submitted in partial fulfillment
of the requirements for the degree

of

Master of Science

in

Optics and Photonics

MONTANA STATE UNIVERSITY
Bozeman, Montana

November, 2017

ACKNOWLEDGEMENTS

Funding Acknowledgment

This research was sponsored by the Office of Naval Research.

TABLE OF CONTENTS

TABLE OF CONTENTS – CONTINUED

TABLE OF CONTENTS – CONTINUED

LIST OF TABLES

LIST OF FIGURES

LIST OF FIGURES – CONTINUED

Figure Page

LIST OF FIGURES – CONTINUED

Figure Page

LIST OF FIGURES – CONTINUED

Figure Page

LIST OF FIGURES – CONTINUED

Figure Page

ABSTRACT

Frequency-chirped readout of spectral features from spatial-spectral (S2) materials, as a result of spectral hole-burning, has been in use as a radio-frequency (RF) spectrum analyzer for well over a decade. Previously, a signal processing deconvolution algorithm had been developed that enabled faster chirping, such that the chirp rate κ could be much greater than the desired resolution bandwidth (RBW). This broke past conventional limits for spectroscopic detection, which states that one needs to dwell on a spectral feature of width Γ for a time $1/\Gamma$. For a chirp, this would mean that the square root of the chirp rate would need to be less than the RBW. For chirp rates on the order of Γ^2 or higher, nonlinearities begin to appear in detected signals depending on optical absorption depth, the chirp rate, and burned hole depths. Even with this algorithm, distortions still persist when very deep holes are burned in a high absorbing material, while the chirp rate is still very high. However, resolving spectral features under these conditions is desirable to increase the dynamic range of the SA. A new nonlinear signal processing technique that removes the nonlinearity has been developed, recovering the distorted signals. It was applied to RF signals spectrally absorbed in two different Tm^{3+}: YAG crystals, with measured absorption lengths of 1.9 and 2.5. The new algorithm is shown to work on multiple spectral holes simultaneously. Signals as wide as 1 MHz and as small as 300 kHz were recovered for a chirp rate of about 11.88 MHz/μs. These results show that very fast chirp rates could be used for highly absorbing materials, with deeply burned spectral holes. This could enable ultra-sensitive readout of a spectrum spanning hundreds of gigahertz, while pushing the dynamic range higher.

1

INTRODUCTION

The radio-frequency spectrum spans upwards of 3 THz in bandwidth [1, 2]. Typically, the range up to about 100 GHz is of most interest. The ability for radar, tracking, and communications to operate over as much of this bandwidth as possible is increasingly important. Real-time detection, without prior knowledge of signals or their content, is a requirement for electronic support (ES) and signals intelligence (SIGINT) [3]. In addition to the ability to monitor extremely broad bandwidths (> 100 GHz) of the RF spectrum, a receiver needs to have high dynamic range (DR). This enables small signals of interest (SOI) to not be mistaken for false signals – spurs – that can be generated by other large signals, like those that come from jammers or other large SOIs. Finally, a spectrum monitoring system should have low latency to ensure detection.

Such a system, capable of achieving these results, had been devised using spectral hole-burning (SHB) technologies for use as an RF spectrum analyzer using spatial-spectral (S2) materials and frequency-chirped laser fields for readout [4]. However, it has limitations. Namely, if a material has high absorption, mixed with a high chirp rate and deep spectral holes, distortions persist. This thesis presents an advanced signal processing algorithm, which corrects for this distortion and restores the spectrum. This should enable future systems using this technology to chirp at higher rates, permitting larger instantaneous bandwidth detection, in crystals with high absorption–yielding a higher dynamic range.

Beyond its use in RF spectrum monitoring, any application that uses SHB technology may benefit from this new algorithm. For example, atomic frequency

comb (AFC) quantum memories require precise measurement of their structure to determine their spectral characteristics [5]. Using this algorithm, measurements could be increased, without sacrificing resolution. Other applications may include frequency references, laser line narrowing, nuclear magnetic resonance imaging, and ultrasonic-optical tissue imaging [6, 7]. This algorithm could be employed for use in other spectroscopic applications, as well.

Spectral Hole Burning Technology

In the 2000's, SHB technologies began to progress for use as an alternative RF spectrum analyzer [4, 8–15]. At the heart of SHB technologies are rare-earth doped crystals. Some typical crystal hosts include YAG (yttrium aluminum garnet, $Y_3Al_5O_{12}$), YSO (yttrium orthosilicate, Y_2SiO_5), or lithium niobate ($LiNbO_3$). Common dopants include thulium (Tm^{3+}), erbium (Er^{3+}), and europium (Eu^{3+}), among others. For this thesis, thulium doped YAG was used, commonly referred to simply as "thulium-yag" and written as Tm^{3+}: YAG. It has a well-measured spectral resonance wavelength of 793.374 nm [6].

One of the main characteristics of these unique materials is their large bandwidths, spanning from a few hundred MHz up to hundreds of GHz depending on the material used [6]. This large spectral bandwidth is due to the inhomogeneous broadening of the material, discussed in Ch. 2. For reference, Tm^{3+}: YAG can have a bandwidth of between 10-30 GHz, depending on the doping and crystal growth process [9, 16, 17]. As important is the homogeneous spectral resolution within the material bandwidth. It has been shown that, by cooling these crystals down to 3-4 K, spectral resolution can be narrowed lower than 100 kHz [18]. That is, individual atomic linewidths smaller than 100 kHz can be detected in the material. This effectively gives up to 3,000,000 resolvable spectral channels (for TM^{3+} doped

materials), where the number of channels is defined as

$$\text{channels} \equiv \frac{\text{material bandwidth}}{\text{individual atomic linewidth}}. \tag{1.1}$$

The number of channels is, thereby, the number of signals you could see across the material's bandwidth. It's easy to see that the number of channels is reduced, when the resolvable individual atomic linewidth is increased.

Rare-earth doped crystals are used as RF spectrum analyzers by "engraving" or "burning" "spectral holes" into the materials' spectral bandwidths [10–13]. The technology employed in this thesis is as follows. An RF signal is captured by an antenna and sent to an electro-optic modulator (EOM), where it modulates a laser sent through the EOM, thereby up-converting the RF signal. In the frequency domain, this places the RF signal on sidebands of the optical carrier frequency. Then the laser beam is sent through the rare-earth doped material, where most of the light is absorbed by the material. This changes the crystal absorption profile, as some of the electrons are promoted temporarily to excited states, where they don't absorb. The new absorption profile is directly related to the RF signal having been burned into the material's spectrum–thus, spectral hole-burning. This can be read out by sending in a low-powered, chirped laser, which scans over and is modulated by the material's absorption profile before being sent to a detector for recording with an analog-to-digital converter. A detailed explanation of this setup and how it works is covered in Ch. 5.

Benefits, Applications, and Limiting Factors

In truth, the engraved spectrum only persists in the material for as long as the atoms are excited [15]. Thus, the spectrum has a finite lifetime, and so it needs to be readout within this time limit. This is the reason for chirping rapidly across the

material. The measured spectral hole lifetime for Tm^{3+}: YAG is around 10 ms [6]. So, by chirping with the appropriate chirp rate, one can scan across the material bandwidth in much less time. For example, say you use a chirp rate of $\kappa = 1$ MHz/μs (chirp rates are typically given units of frequency over time), and you need to scan a material bandwidth of $\Gamma_I = 10$ GHz. Then, the time it would take to scan across this would be $t = \Gamma_I/\kappa = 10$ GHz/(1 MHz/μs) = 10 ms. The subscript I refers to the inhomogeneously broadened material bandwidth. So, you would be able to see the entire spectrum, all at once, by doing so within the time limit imposed by the excited state lifetime of the atoms. Note that if you chirp even faster, it would take less time to read over it.

Another major benefit is what one can see. Since the medium records any signal that hits it, there is a 100% probability of detection of any incoming signal [19]. This lies within stark contrast with more traditional spectrum analyzers, based on scanning filters or digitizers. They can miss signals that are not within the narrow band of the instantaneous frequency of the scanner. For example, a 100 MHz measurement bandwidth, real-time spectrum analyzer will miss 99.5% of all incoming signals, when scanning over a 20 GHz range [19]. The S2 spectrum analyzer can easily record transient pulses, as well as hopper signals, since all frequencies are being recorded all the time by the material. This simply cannot be done on other RF spectrum analyzers, and is a property intrinsic to this technology.

Because of the nature of the system, taking in RF spectral features and up-converting them to optical frequencies, this system works like a hybrid spectrum analyzer. It has all the benefits of OSA and RFSA systems, without the drawbacks. Therefore, it is ideal for many applications, such as electronic warfare (EW) and SIGINT, analog signal processing and data mining, geolocation of transmitters by time difference of arrival (TDOA) or direction finding (DF), adaptive and covert RF

communications, and true-time delay to name a few [19, 20].

Beyond the physical limitation presented by the excited state lifetime, there is another issue that becomes apparent by chirping fast. While one can easily record the entire spectrum of the material within the required time limit, you scan faster than is necessary to accurately readout the signals. Typically, a spectrum analyzer requires that you dwell on a signal of some bandwidth for a time equal to one over that bandwidth [21]. If a signal has a bandwidth of $\Gamma = 1$ MHz, for example, then a typical spectrum analyzer must dwell on it for a time much greater than 1 μs to resolve it. To resolve this, you want the resolution bandwidth to be $\delta\nu_{\mathrm{RBW}} \approx 2\Gamma$. In terms of chirp rate, the requirement is for $\kappa \lesssim \delta\nu_{\mathrm{RBW}}^2$ [4]. If you go past this limit, then you get a ring out distortion response due to the phenomenon of free induction decay (FID) [22], which is explained in Ch. 2. This can also be thought of as being caused by the Kramers-Kronig relations, which determine the material dispersion [23].

Fig. 1.1 shows what one can expect for varying chirp rates scanning across a 1 MHz wide spectral hole. The amplitudes are normalized to the original spectral hole. It is evident that for increasing chirp rates, the distortion gets worse. Each ring has spread itself out, spectrally, for a bandwidth given by $\kappa/\delta\nu_{\mathrm{RBW}}$ [8].

Spectral Recovery

The ringing out effect seen in Fig. 1.1 is, of course, a problem. This was thought to have imposed a speed limit on how fast one could chirp across the material [15, 24, 25]. For example, a 1 MHz resolution would require a chirp rate of less than 1 MHz/μs. This would imply it would take greater than 10 ms to chirp across a 10 GHz bandwidth, which is much longer than the population lifetime of the material.

A novel solution was invented in 2005 by Chang et al [4]. One can deconvolve the ringout in post-processing, after the signal has been detected. The procedure is

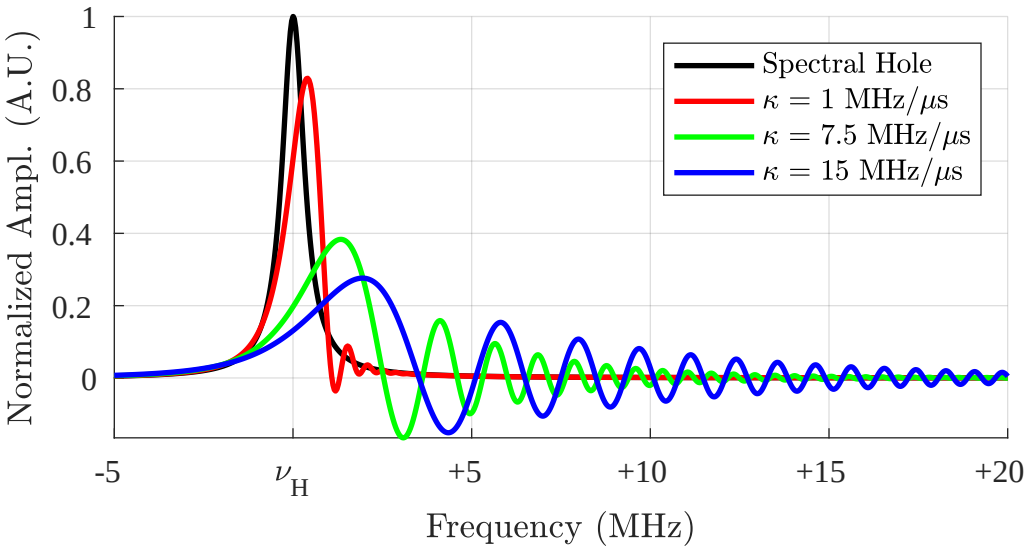

Figure 1.1: Example of the ring-out, distortion effect caused by different chirp rates for a pulsed laser beam reading over a 1 MHz wide signal.

rather simple. By taking the Fourier transform of the recorded signal, the chirp term is removed by multiplying by its complex conjugate. This is possible, because, while one is not in control of what RF signals are going to be detected, one is in control of the chirped laser that reads out the signal. Thus, you know the chirp rate, and you can remove it. The resultant spectrum is said to have been "recovered."

This algorithm enables spectral features to be recovered with arbitrarily fast readout chirp rates, provided that the chirp bandwidth covers the full spectrum of interest plus a little bit extra. This little bit extra is so that a hole near the end can be fully recovered. Now, the limit on spectral resolution is governed by the detector bandwidth $\delta\nu_{\text{det}}$, which is a combination the detector and digitizer that captures the signal–taking the lower of the two sample rates [4]. To see why this is true, imagine a spectral hole of width Γ. If the spectral hole occurs at time location t_H, then the ringing will last for a time $\tau = 1/\Gamma$. So, the frequency bandwidth this corresponds to is $\nu = \kappa\tau = \kappa/\Gamma$. Therefore, if the maximum frequency bandwidth able to be detected is $\nu = \delta\nu_{\text{det}}$, then the minimum resolvable spectral feature is $\Gamma_{\text{min}} = \kappa/\delta\nu_{\text{det}}$.

For this thesis, the detector, as oppose to the digitizer, was the limiting factor, having a resolution of 40 MHz, which ends up corresponding to a minimum resolvable spectral feature width of just over 297 kHz. Therefore, the spectral resolution of the recovery algorithm is determined by the chirp duration instead of by the chirp rate. However, even this method provides limitations to what kinds of chirp rates one would want to use. This is because problems still exists for highly absorbing crystals, deep holes, with fast readout. To see this, the algorithm is applied to the example from Fig. 1.1. The result is shown in Fig. 1.2. One can see that the algorithm does, indeed, remove the ring-out distortions from all three tests scans, and restores a single peak for all three chirps. Yet, a nonlinearity still persists.

Nonlinearities in Spectral Recovery

Fig. 1.2 shows that the recovered signals are not restored completely to the original spectral hole, given $\alpha_0 L = 4$. First, the peak heights on the recovered signals are reduced. In the most extreme case of this example, when $\kappa = 15$ MHz/μs, the peak height is restored to being about 40% less of where it should be, on the linear scale. Secondly, the higher chirped readouts leave a non-symmetric shape, as opposed to a Lorentzian shape that the spectral holes are known to have. In fact, both the loss in signal strength and nonlinearity increase as the chirp rate increases. On a logarithmic scale, the nonlinearity becomes glaring. The 7.5 and 15 MHz/μs chirp rates produce high nonlinearities, beginning to really separate around 1 MHz away from the main peak. On this scale, however, the smaller chirp rate seems to line up well with the original spectral hole. The nonlinearity is referred to as a "tail," because it is most prominent after the detected hole peak in time. It can be thought of being caused by higher-order FID terms, discussed in Ch. 3.

One can check the amplitude differences between the three peaks and the original

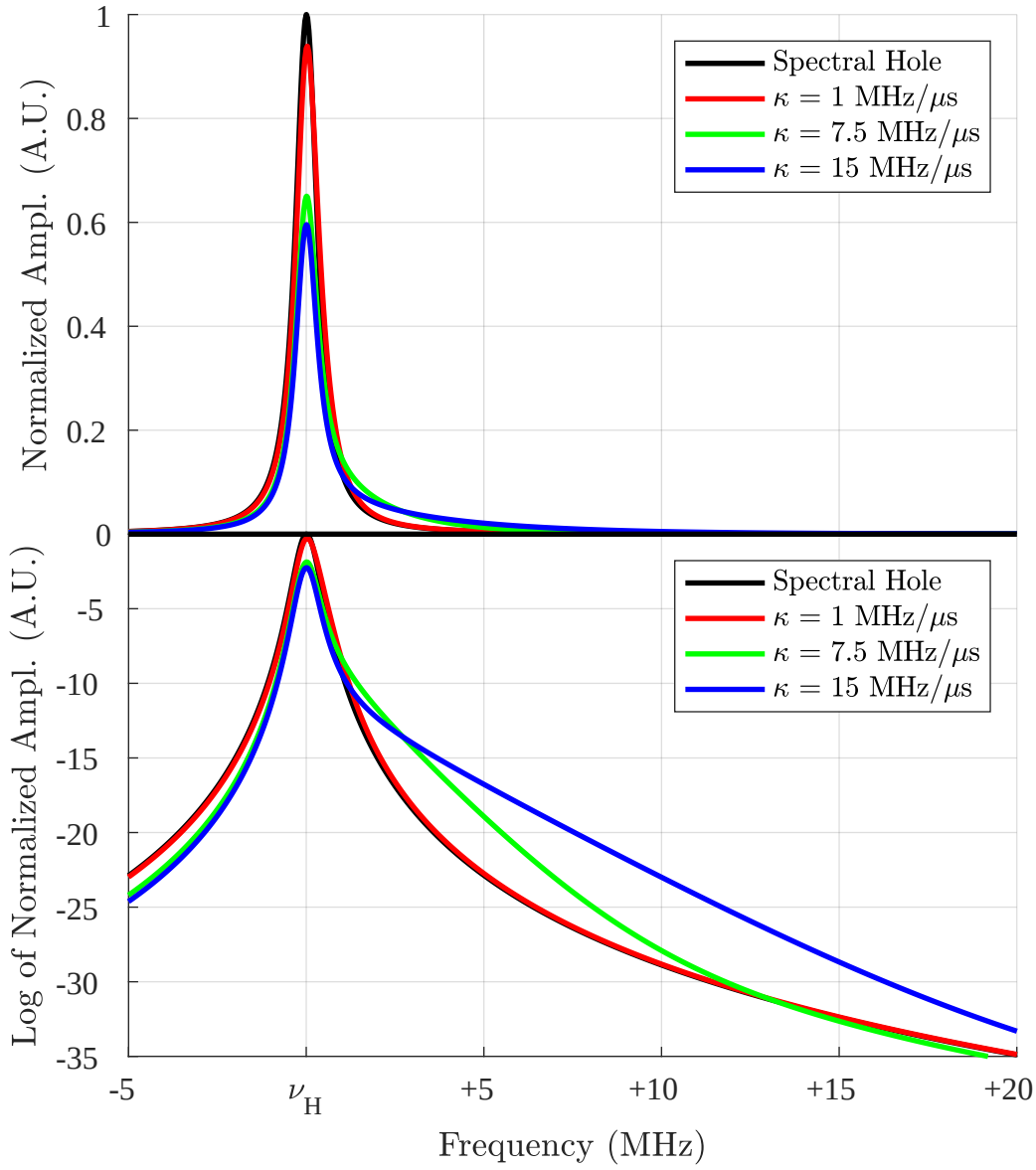

Figure 1.2: Linear and logarithmic scaling of spectral recovery for distorted signals from the previous example, seen in Fig. 1.1, for various chirps rates applied to a readout laser scanning a 1 MHz wide signal, with a hole depth $\beta = 0.3$.

hole, which would be a metric as to how large the tail is. As expected, the higher chirp rates stray away from the original hole shape, reaching a maximum amplitude difference of about 4 and 6 dB for the 7.5 and 15 MHz/μs chirps, respectively. This is seen in Fig. 1.3. Interestingly, the 1 MHz/μs chirp has a similar shape as the others, it is just much smaller. This does tell you that the small chirp follows the hole quite well compared to the others, but that it, too, has a nonlinearity to it. In all cases, the difference between chirped signals and the original hole do eventually return to zero, as it should, after the hole. It just happens much further for higher chirp rates.

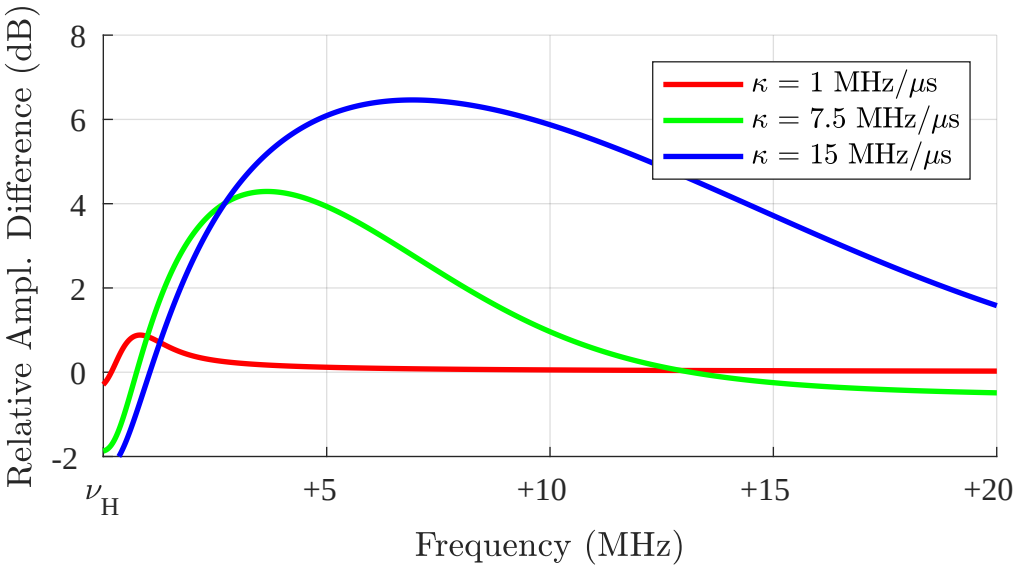

Figure 1.3: Relative amplitude differences for the various chirps, where the difference is taken from the original spectral hole seen in the logarithmic scale from Fig. 1.2.

This motivates the need for a new, nonlinear recovery algorithm that can remove this distortion from happening. By doing so, the dynamic range of the S2SAs should be able to increase even further than they currently are, while maintaining all the desirable features they contain.

Consideration of Alternative Nonlinear Recovery Algorithms

While discovering the path to a new nonlinear recovery algorithm, an approach was suggested from work done previously by Dr. W. R. Babbitt and Aaron Dalbey an undergraduate student [26]. The algorithm was designed to work using an iterative method. It works by first taking the recovered spectrum and normalizing it to the background spectrum. The log of this result is taken, with a minus sign, to yield the change in absorption length spectrum. This is added onto the background absorption, yielding an estimated absorption spectrum profile. Then, a new causal transfer function and output electric field are simulated using similar techniques that provided Fig. 1.1. The output electric field is subtracted by the background field. This forms the basis for a change in output intensity, which is then subtracted from the actual output intensity, giving a "corrected" output intensity, which gets linearly recovered.

The process could have been repeated several times to improve results, but typically only one iteration was sufficient. It was shown that it could be improved further by adding another step, which was to include a sort of power expansion of the first step, where the natural log term is given a pseudo power series expansion out to 3 terms.

The main reason why this approach was not pursued in this thesis, as a practical update to the linear recovery algorithm, is the computation complexity (though the complexity is comparable to within an order of magnitude to the method pursued in this thesis) of simulating the full chirp field (which is actually not required, as this code could easily be rewritten with complex fields) and causal absorption transfer function several times in an iterative fashion (though only one iteration is needed). The original version of this method used simulation of real fields, which increases

the number of required points by at least an additional factor of 4. While use of carrier elimination and complex fields can reduce this factor, for each iteration, a full Nyquist sampled $f_s \approx B_{\text{chirp}}$ chirp field must be simulated resulting in many more points to process than just the original data collection rate of $\sim 100 - 200$ Msamp/s. Finally, as an iterative algorithm, the computational load is variable (though typically not), to achieve the same level of tail removal as demonstrated in this thesis. For sensor systems, a fixed, hopefully low cost computational approach is preferred. The approach presented in this thesis appears to achieve this over a range of absorption lengths, hole depths and widths, and chirp rates, but requires calibration of a "$\mathcal{L}$" parameter, unlike the previous approach.

BACKGROUND

Spectral Line Broadening

Spectral lines occur as a result of either the absorption or emission of light by atoms. While they are colloquially called lines, they actually have some width to them. If the spectral line width is spread out by any mechanism, it is called broadening. There are two categories of line-broadening mechanisms discussed in this section. The first is homogeneous broadening, in which all individual atoms are effected the same way. There are several causes of homogeneous broadening, but they all do the same thing: take the natural atomic spectral linewidth and broaden it by some mechanism. Relevant mechanisms for this discussion will be natural broadening, non-radiative broadening in solid structures, and broadening from phase decoherence. The second type of broadening is inhomogeneous broadening, where atoms are shifted by different amounts and contribute to different parts of the overall spectrum. This section follows from sections 4.1, 4.4, and 4.5 of Fox [27], and 3.4 from Allen & Eberly [22].

Homogeneous Broadening

In a two-level atomic system, an atom can move from a ground state to an excited state and back, by interacting with the optical field. The difference in energy between the ground and excited states is given by

$$h\nu_0 = E_2 - E_1. \tag{2.1}$$

The process of going from ground to excited state is called absorption, and occurs when an atom absorbs a photon. Going from the excited to the ground state is

called emission, and occurs when emitting a photon. If this happens when no other photons are present, the process is called spontaneous emission. The rate by which spontaneous emission occurs is proportional to the number of atoms in the excited state. Given as

$$\frac{\mathrm{d}n_2}{\mathrm{d}t} = -A_{21}n_2, \tag{2.2}$$

where A_{21} is a coefficient for the rate at which atoms go from excited to ground states, known as an Einstein coefficient. The solution to (2.2) is

$$n_2(t) = n_2(0)\exp(-A_{21}t). \tag{2.3}$$

It is for this reason that

$$\tau_{21} \equiv \frac{1}{A_{21}} \tag{2.4}$$

is defined to be the radiative lifetime of the excited state. A similar relationship exists for absorption.

The ions that get emitted or absorbed are not perfectly monochromatic, however. The shape of the emission line can be represented using a spectral lineshape function, most commonly denoted by $g(\nu)$. The value ν_0 defines the peak of $g(\nu)$. It is also normalized so that

$$\int_0^\infty g(\nu)\mathrm{d}\nu = 1. \tag{2.5}$$

The other defining parameter in the lineshape function is the full-width at half-max (FWHM), which is defined here to be Γ_H. It is a measure of the width of the spectral

line.

Natural Broadening Sometimes called radiative broadening or lifetime broadening, natural broadening is a result of spontaneous emission. If the intensity coming from the burst of light due to an ensemble of photons is considered as a decaying exponential, given as

$$I(t) \propto \exp(-t/\tau_{21}), \tag{2.6}$$

it can be shown that this would translate to the frequency dependent lineshape function

$$g(\nu) \propto \frac{1}{1 + \left(\frac{\nu - \nu_0}{\Gamma_H/2}\right)^2}, \tag{2.7}$$

where $\Gamma_H = 1/\pi\tau_{21}$. The functional form given in (2.7) is called a Lorentzian, and is the typical shape for homogeneous spectra. Fig. 2.1 graphically displays (2.6), while Fig. 2.2 shows what the function (2.7) looks like.

Non-Radiative Broadening Another type of homogeneous broadening is non-radiative broadening. For example, in solids, the atoms are locked in place, but they can still be excited by absorbing photons. The difference is that they can transition back down to the ground state in a non-spontaneous way, in addition to the spontaneous process. This can be due to vibrational motion from the lattice structure, called a phonon, that carries the energy out. Since the transition is not caused by a radiative process, it is known as a non-radiative transition. To account

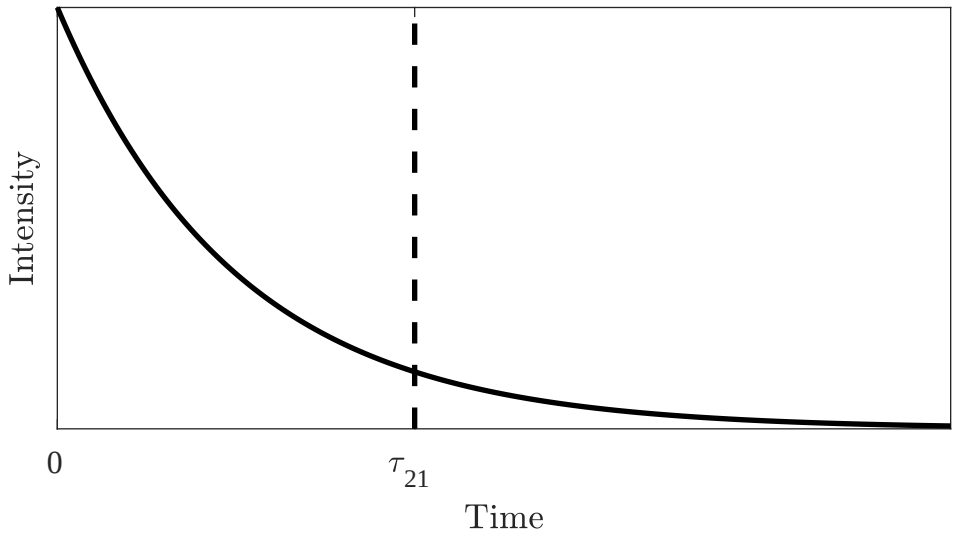

Figure 2.1: Intensity as a function of time, resulting from an ensemble of photons with decay rate τ_{21}.

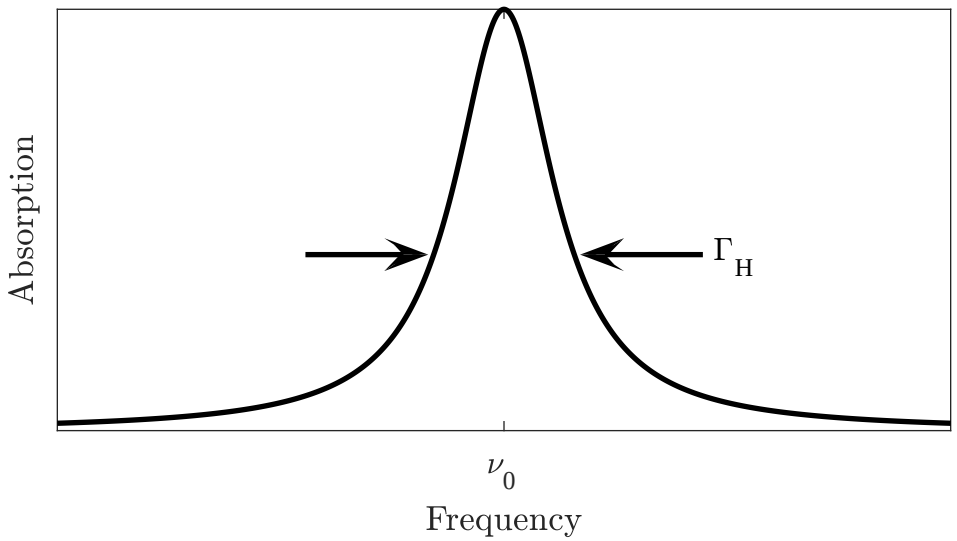

Figure 2.2: Spectral shape given by (2.7), with a resonant frequency ν_0 and FWHM $\Delta\nu \equiv \Gamma_H$, as a result of an emitted photon.

for this, (2.2) is adapted to be

$$\frac{\mathrm{d}n_2}{\mathrm{d}t} = -\left(A_{21} + \frac{1}{\tau_{\mathrm{NR}}}\right) n_2, \tag{2.8}$$

where τ_{NR} is the non-radiative relaxation time. Now, (2.4) is adjusted to be

$$\frac{1}{\tau_{21}} \equiv \frac{1}{\tau_{\mathrm{R}}} + \frac{1}{\tau_{\mathrm{NR}}}. \tag{2.9}$$

This will shorten the lifetime of the excited state, causing even more broadening.

Phase Decoherence In addition to the radiative and non-radiative broadening, in crystals, the atoms also exhibit homogeneous broadening from phase decoherence through interactions of phonons in the host material. At temperatures that go as low as 3 K, this is the dominant homogeneous broadening in rare-earth materials [28]. There are two dephasing times to consider when discussing phase decoherence [29]. The first is $T_1 \equiv \tau_{21}$, which encompasses all forms of population decay. The other is T_2', which is a pure dephasing term, which can be thought of as a phase modulation of an optical transition. They may be combined to form a dephasing time, to define a homogeneous width as

$$\Gamma_H \equiv \frac{1}{\pi T_2} = \frac{1}{2\pi T_1} + \frac{1}{\pi T_2'}. \tag{2.10}$$

To think about why dephasing leads to a linewidth, imagine a single ion that is dephasing over time. The dephasing leads to a frequency change over time. So, this causes the linewidth to spread out.

Inhomogeneous Broadening

Now, think about a collection of N atoms in a crystal lattice structure. If all the atoms were arranged in an identical fashion, then it would be expected that they all resonate at the same frequency ν_0. However, during the growth process of crystals, defects and imperfections occur, which cause the atoms to have different local fields around them. What this means is that their resonant frequencies change slightly, due to Stark shifts. The collection of these shifts will spread out the lineshape. The process of spreading out resonant frequencies for otherwise identical atoms is called inhomogeneous broadening. The linewidth of this is taken as the envelope of the collection of atoms, and it can be thought of as a superposition of Lorentzians. The inhomogeneous linewidth is denoted Γ_I. A simple model for what shape the envelope may take on would be a Gaussian shape that is a result of the Central Limit Theorem [30]. From statistics, it briefly states that when N independent, random variables are added together, their sum tends towards a normal distribution, i.e. a Gaussian. In this case, the ions at each resonance are the random variables. This superposition is displayed in Fig. 2.3. Finally, the inhomogeneous decay time is denoted as T_2^*, so that

$$\Gamma_I = \frac{1}{\pi T_2^*}. \tag{2.11}$$

In the temperature regime of interest for this thesis, $\Gamma_I > \Gamma_H$, implying that $T_2 > T_2^*$.

Free Induction Decay Optical free induction decay, sometimes called "free polarization decay" (FPD), was first described in the field of nuclear magnetic resonance (NMR) [22, 31, 32]. The general idea of FID is that when a brief pulse, with a pulse duration of the order of one over the total linewidth (including

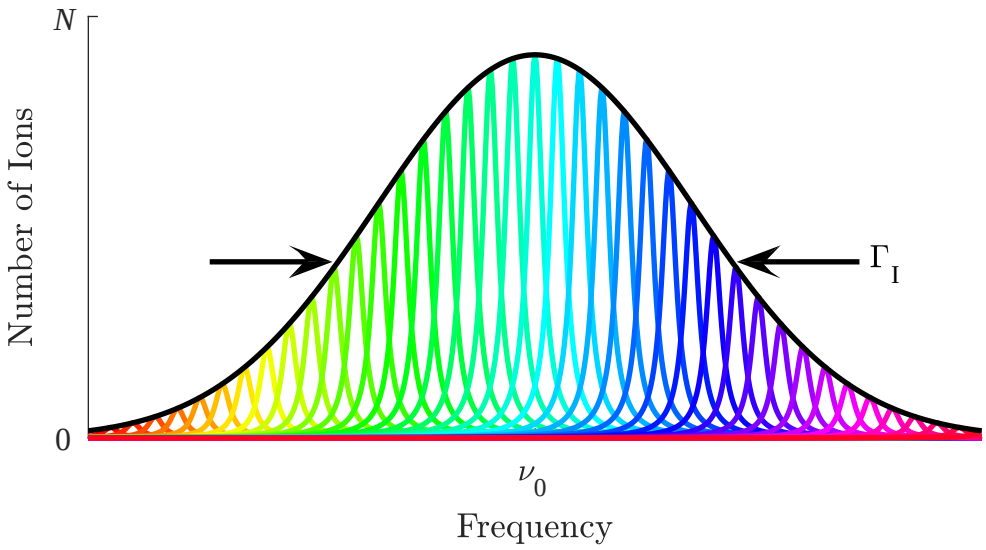

Figure 2.3: Spectral lineshape due to inhomogeneous broadening.

inhomogeneous linewidth) or shorter, is applied to an ensemble of atoms, the atoms will become excited all at once and then dephase over time. One way to think about this is the pulse excites a phased array of atomic dipoles, which begin to radiate coherently. However, due to the broadening, these atoms radiate at different frequencies. Eventually, all the atoms become dephased. The dephasing process occurs at a rate that is one over the inhomogeneous width, T_2^*. Furthermore, the FID behavior is related to the Fourier transform of the lineshape function, which allows lineshapes to be determined from measuring the time domain FID decay. If narrow spectral holes are burned into an inhomogeneous line, there will be fast and slow decay terms in an FID measurement related to the broad inhomogeneous line and the narrow homogeneous line (spectral holes), respectively. The stronger fast terms die out quickly, but the weaker and the slower terms will dominate at long time scales.

The reason that this is important for this work is that it is one interpretation for the ring out that is observed when fast chirp scans across the spectral holes in the inhomogeneous line. If a single homogeneous line is scanned across by a fast chirp, the chirp will be resonant with the homogeneous line for a very short amount

of time, thus a brief pulse (roughly given by a time $t = \Gamma_H/\kappa$). Thus, this causes FID like effects to appear, despite dealing with a spectral hole (absence of atoms to excite), rather than a sharp spectral line. Because this chirp effect is slow compared to the inhomogeneous line, only the slow FID decays related to the holes are observed. This FID like concept was used to motivate the approach to the nonlinear recovery algorithm.

Voigt Profile

Most treatments assume that the general profile due to inhomogeneous broadening should be a Gaussian. However, we often observe spectrum to be somewhere between a Gaussian and a Lorentzian [30]. Defined as a convolution between the two profiles, the Voigt profile may more accurately describe the observed behavior. The definition is given here as

$$V(\nu;\sigma,\gamma) \equiv \int_{-\infty}^{\infty} G(\nu';\sigma)L(\nu-\nu';\gamma)\mathrm{d}\nu', \tag{2.12}$$

where G is a Gaussian of width σ and L is a Lorentzian of width γ. It will be observed in Ch. 5 that the Voigt profile fits the material spectrum more accurately than a Gaussian alone does. However, it is also found that a Lorentzian profile fits the data best. An example of what a Voigt profile looks like, compared to both a Gaussian and Lorentzian, is seen in Fig. 2.4.

The Inhomogeneous Absorption Spectrum

In the experiments and results of this chapter, one quantity that is of importance is the absorption length of the material $\alpha_0(\nu)L$. This provides the inhomogeneously broadened spectrum. In general, once this quantity is obtained, the laser fields are

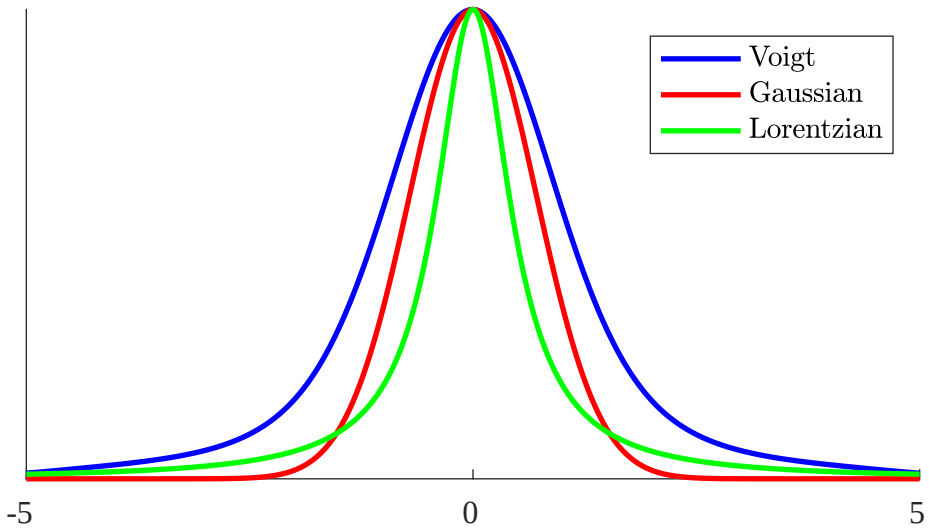

Figure 2.4: The Voigt profile compared to a Gaussian and Lorentzian profiles that were used to create the Voigt shape.

frequency tuned to the maximum absorption length of the material. This is denoted as $\alpha_0 L$. To obtain this quantity, one may employ the use of Beer's Law. However, in the lab we used a technique called optical nutation, which allows the measurement of and the intensities from Beer's law.

Beer's Law

The full derivation of the Maxwell picture for electric field propagation through an absorbing material is covered in Ch. 3. For this discussion, consider that electric-field propagation through a collection of atoms, given as an intensity, may be described by Beer's law [32]. It states that for some laser frequency ν_0, propagating through a homogeneous, isotropic medium, the intensity in the medium is given by

$$I_{\nu_0}(z) = I_{\nu_0}(0)e^{-\alpha_{\nu_0} z}, \tag{2.13}$$

where α_{ν_0} is the absorption coefficient for the given frequency ν_0. The other assumption being made, here, is that the laser power is weak. If the length of the

material is L, then Eqn. (2.13) may be rearranged so that

$$\alpha_{\nu_0} L = -\ln\left(\frac{I_{\nu_0}(L)}{I_{\nu_0}(0)}\right). \tag{2.14}$$

Therefore, the absorption length may be calculated if the intensity at both points $z = 0$ and $z = L$ are known. If the laser frequency is tuned across the absorption line, then the absorption length would also change as

$$\alpha_0(\nu) L = -\ln\left(\frac{I_{\nu}(L)}{I_{\nu}(0)}\right). \tag{2.15}$$

This provides an avenue upon which the absorption spectrum of a material may be mapped out, assuming these intensities can be known.

Optical Nutation

For a discussion on how a quantum-mechanical two-level system works, see [27, 33]. Tm^{3+}: YAG crystals can be described as an ensemble of such atoms. When taken as a collection, the same behavior needs to be defined macroscopically. If a sample rare-earth material is suddenly hit with an optical field, ions that are in their ground state configuration will be sent to their upper state. Then, they emit radiation, as a result of stimulated emission. Thus, they are sent back their lower state. Once, they are in the lower state, however, they are free to absorb more incoming photons, driving them back up to the excited stated, again. This back and forth is called absorption and emission. The behavior is, then, damped due to dephasing effects. What this means is that the ions eventually settle into an equilibrium, where the same number of ions that are being absorbed are also emitting radiation. Thus, 100% of the incident optical beam is transmitted through the medium. This process is called optical nutation.

This is different from Rabi flopping and damping effects, alone, that can describe a single two-level atom. First, this is for a collection of ions, being hit with a field that has some with generalized Rabi frequency Ω. The intensity of the beam hitting the material is low-powered enough, such that there is also dephasing effects. In this sense, optical nutation is like a combination of Rabi flopping with damping. Moreover, Rabi flopping describes the change in probability amplitude for a single atom, whereas optical nutation describes the transmission of the optical field through the material.

The intensity of a transmitted laser due to a collection of inhomogeneously broadened two-level atoms can be described by

$$I(t) \propto I_0 - Ae^{-\gamma(t-\tau_1)} J_0(\Omega_R(t-\tau_1)), \tag{2.16}$$

adapted from Eqn. (3-113) in [34], where the term A represents a collection of constants and has units of intensity, γ is the damping rate due to dephasing, Ω_R is the Rabi frequency, I_0 is the intensity before interaction, J_0 is the Bessel function of the first kind, and τ_1 represents the time the pulse is turned on. This behavior mathematically describes optical nutation. It's also worth pointing out that the reference is for a gas, but the behavior is the same for a solid [35]. The assumption for (2.16) is that the laser field has an intensity that is low enough that it cannot overcome dephasing effects, but high-enough that it can change the medium. It is also being pulsed for time that is short compared to T_1, but can be long compared to T_2.

Linking the Bloch and Maxwell Pictures

To describe the exact equation that links the quantum interpretation of optical field propagation to the macroscopic one, it would be necessary to employ the

Maxwell-Bloch equations. However, this lies outside the scope of this thesis. Instead, the Maxwell aspect, alone, can be heuristically related to the Bloch picture. Namely, a link between Beer's law and optical nutation is needed.

Using the optical nutation picture, at the moment the pulse of light hits the material, spatially defined to be $z = 0$, the intensity should be at 100%. In other words, no part of the beam is being absorbed, as it has just touched the material. In the Beer's law view, this would be given by $I_\nu(0) = I_0$. In the optical nutation picture, $I(t \gg \tau_1) = I_0$, or 100% transmission, is the behavior after a long time has past. After the optical pulse has reached the end of the material, $z = L$, the maximum amount of absorption has taken place. In the Beer's law picture, this is described by $I_{\nu_0}(L) = I_0 e^{-\alpha_{\nu_0} L}$. In the optical nutation picture, maximum absorption occurs right after the pulse turns on $t = \tau_1$, $I(\tau_1) = I_0 - A$. Therefore, linking these concepts,

$$I_\nu(z = 0) = I(t \gg \tau_1), \tag{2.17}$$

and

$$I_{\nu_0}(L) = I(\tau_1). \tag{2.18}$$

Hence,

$$I_0 e^{-\alpha_{\nu_0} L} = I_0 - A. \tag{2.19}$$

This implies that,

$$A = I_0(1 - e^{-\alpha_{\nu_0} L}). \tag{2.20}$$

So, (2.16) may be written as

$$I(t) = I_0 \left[1 - \left(1 - e^{-\alpha_{\nu_0} L}\right) e^{-\gamma(t-\tau_1)} J_0(\Omega_R(t-\tau_1))\right]. \tag{2.21}$$

Moreover, (2.15) may now be written in terms of optical nutation, as well,

$$\alpha_0(\nu)L = -\ln\left(\frac{I(\tau_1)}{I(t \gg \tau_1)}\right). \tag{2.22}$$

By recording the optical nutation for different frequencies, and identifying these values, the absorption spectrum is, therefore, determined by utilizing (2.22). In the lab, this convenient technique also eliminates the need to calibrate out the losses from the windows of the chamber and the Fresnel reflections at the crystal faces. The intensity pattern described in this subsection is recorded in the lab, with results presented in Ch. 5. It was used to map out the absorption spectrum for the two Tm^{3+}: YAG crystals that were used.

As an example of what to expect from (2.21), if $A = .9I_0$ (implying $\alpha_0 L \approx 0.1$) and $\tau_1 = 0$, then the normalized intensity would be given by

$$I(t)/I_0 = 1 - 0.9e^{-\gamma t} J_0(\Omega_R t), \tag{2.23}$$

This behavior is described in Fig. 2.5, for a Rabi frequency of $\Omega_R = 0.7$ MHz and a damping rate $\gamma = 0.1$ MHz. One caveat to point out here, it may be alarming to see that the normalized intensity is pushing past 100%, implying more energy is being taken out than is being put in. However, what it is physically happening is the atoms are storing energy, and, over time, emitting this stored energy as radiation faster than they are simultaneously absorbing it. The reverse physical situation happens, as well. This is the cause of the oscillatory pattern.

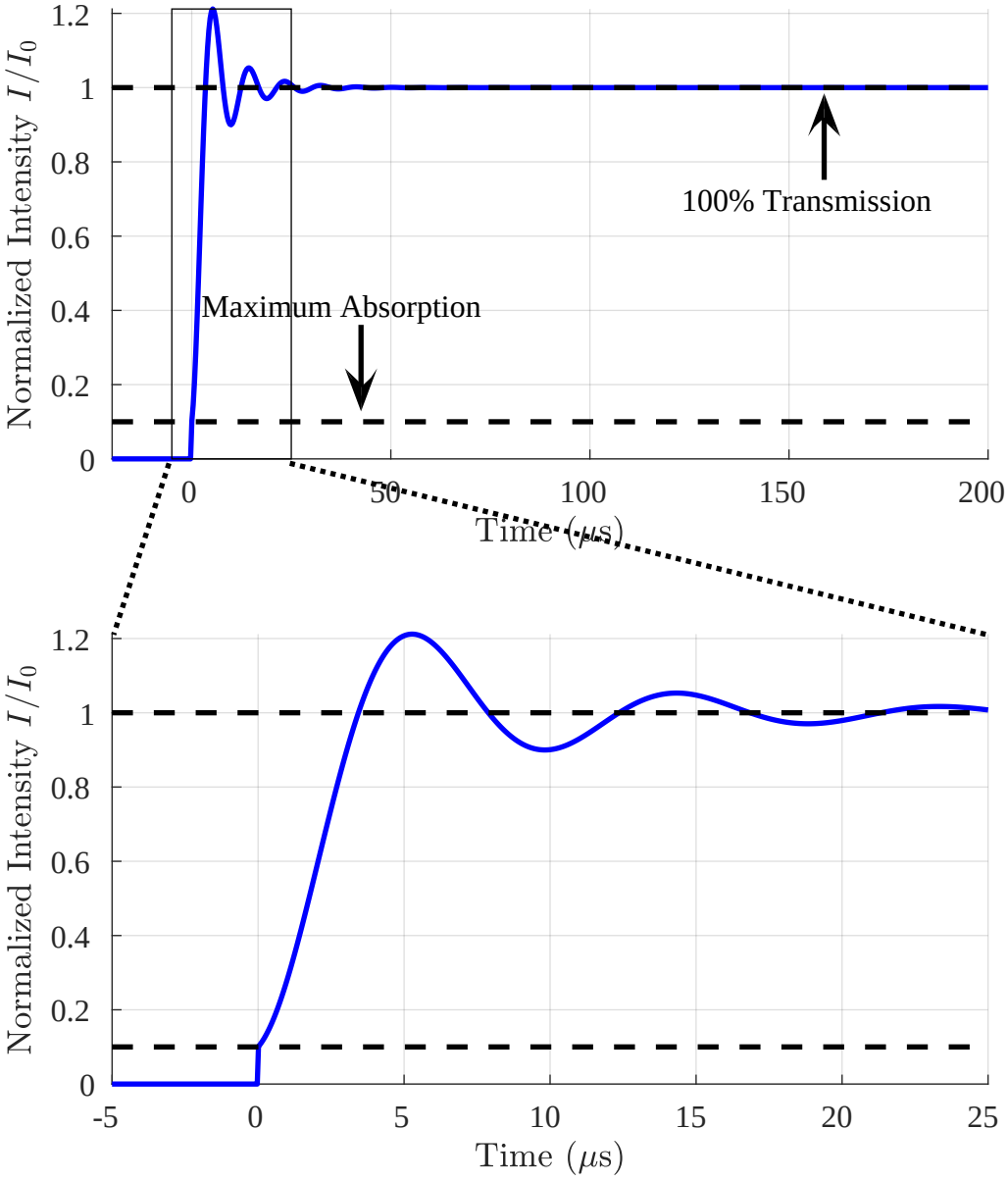

Figure 2.5: Example of optical nutation for the damping rate $\gamma = 0.1$ MHz, with $\Omega_R = 0.7$ MHz.

This method, by which the absorption length is determined, also helps with another lab issue: laser drifting. The tunable laser's frequency is set on a computer, but the actual frequency the laser puts out can be different from that of which is put in. This can be attributed to laser drifting. For example, by setting different frequencies and using (2.22), the absorption spectrum for Tm^{3+}: YAG is mapped out. When the maximum absorption is hit, then that frequency corresponds to 793.374 nm. This can be used as a reference against what the laser is being set to on the computer, so that the difference between where the computer is saying the laser frequency is and what it actually is can be determined. This will also be seen in Ch. 5.

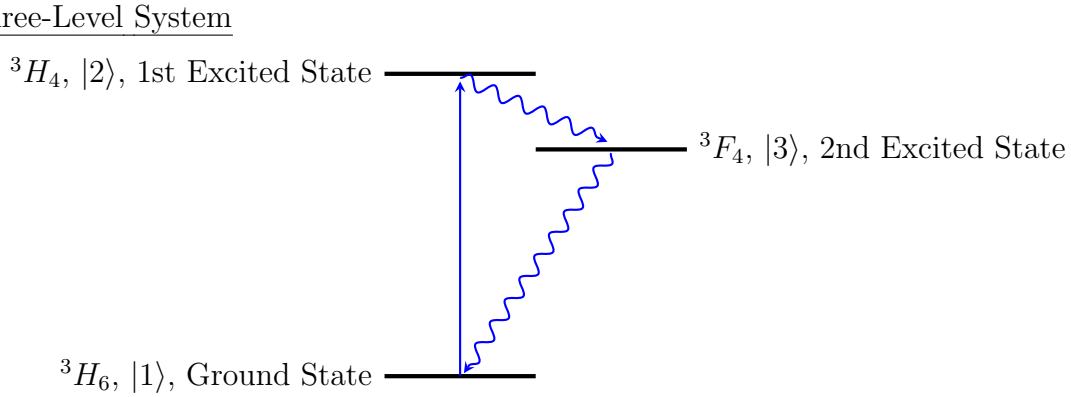

Figure 2.6: Three-level diagram of Tm^{3+}: YAG.

This subsection follows from Gorju et al. [16]. Treatment of a two-level system has been gone through thus far, but Tm^{3+}: YAG can be treated as a three-level system, too. That is, it permits electrons to be promoted to two different excited states from its ground state configuration. The electrons have several options of where they can go. Label the ground state, 1st excited state, and 2nd excited state as 1, 2 and 3, respectively. Then the electrons can go from $1 \to 2$, $2 \to 1$ or $2 \to 3$, and from $3 \to 1$, see Fig. 2.6. The amount of time spent in any of the three levels is finite. The population densities of these states are governed by the following incoherent rate

equations:

$$\frac{\mathrm{d}n_1}{\mathrm{d}t} = -\frac{\sigma I}{h\nu_0}(n_1 - n_2) + \frac{1}{\tau_{21}}n_2 + \frac{1}{\tau_{31}}n_3, \tag{2.24}$$

$$\frac{\mathrm{d}n_2}{\mathrm{d}t} = \frac{\sigma I}{h\nu_0}(n_1 - n_2) + \frac{1}{\tau}n_2, \tag{2.25}$$

$$\frac{\mathrm{d}n_3}{\mathrm{d}t} = \frac{1}{\tau_{23}}n_2 - \frac{1}{\tau_{31}}n_3, \tag{2.26}$$

where n_1, n_2, and n_3 are the population densities of the ground, 1st, and 2nd excited states, respectively, σ is the absorption cross section, h is Planck's constant, ν_0 is the resonance frequency, and I is the intensity of the light. The values $\tau_{21}^{-1}, \tau_{31}^{-1}$, and τ_{23}^{-1} represent the relaxation rates of the ions to fall from the state indicated in the first number to the second number. So, for example, τ_{21}^{-1} is the relaxation rate to go from the first excited state directly to the ground state. Lastly, $1/\tau = 1/\tau_{21} + 1/\tau_{23}$. The initial conditions on the system are that $n_1(0) = 1$, while $n_2(0) = n_3(0) = 0$.

This gives three, coupled differential equations to solve for. However, for many purposes, Tm^{3+}: YAG need only be treated as a two-level system, ignoring the second excited state. This is due to the fact that the material is only used within the lifetime of the atoms staying in the 1st excited state, and not going to the 2nd excited state. As stated, this is known to be around 800 μs. Therefore, only considering the physical effects of a two-level system, has been justified.

Spectral Hole-Burning

Spectral hole-burning is when a laser is used to change the absorption spectrum (see, for example, chapter 30 in [30]). A finite number of ions will absorb the incoming photons from the laser, corresponding to the resonance frequency of those ions who resonate with the photons. This cuts out a pieces of the inhomogeneous spectrum,

which is where the name spectral hole burning is derived. If the burned spectrum is defined by some $\Delta\alpha(\nu)L$, then the new inhomogeneous spectrum would be given by

$$\alpha(\nu)L = \alpha_0(\nu)L - \Delta\alpha(\nu)L. \tag{2.27}$$

An example of what this might look like for an arbitrary absorption pattern is given in Fig. 2.7. It is this pattern that is scanned over and read out by a low-powered, chirped laser, mentioned in Ch. 1.

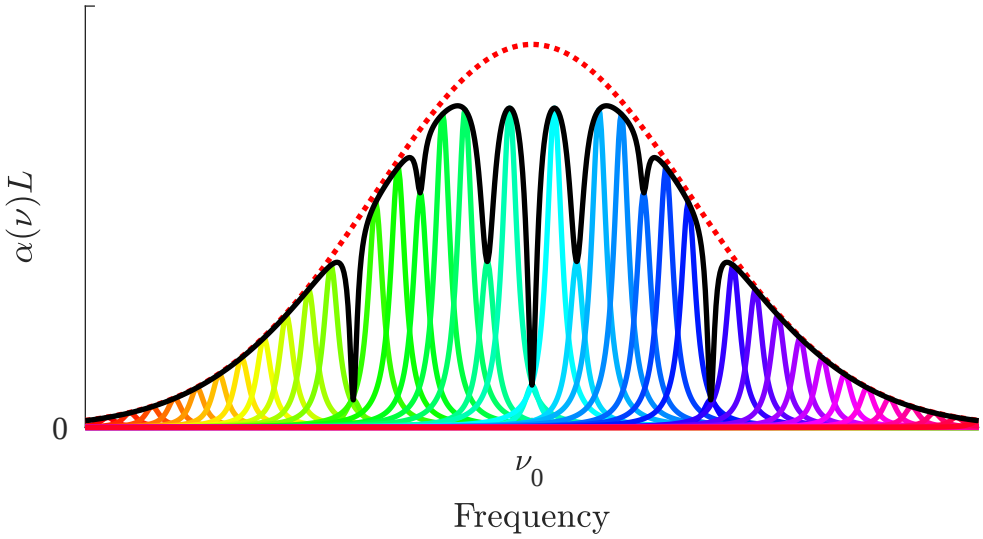

Figure 2.7: An arbitrary absorption pattern burned into an inhomogeneous spectrum (black), overlaid on the original inhomogeneous spectrum (dotted red).

The burned absorption pattern in the inhomogeneous spectrum is the desired outcome. It is easy to see that if the inhomogeneous spectrum is subtracted out, then what would be left is the absorption $\Delta\alpha(\nu)L$.

$$\Delta\alpha(\nu)L = \alpha_0(\nu)L - \alpha(\nu)L. \tag{2.28}$$

Subtracting out the unaltered spectrum from the SHB pattern in Fig. 2.7, the pattern in Fig. 2.8 would be seen. This can be achieved in the lab, by sending in an identical

beam through the crystal that covers the same length L through the crystal, but does not cross paths with either of the other two beams. This would provide the pattern that can then be subtracted out. This laboratory method is covered in Ch. 5.

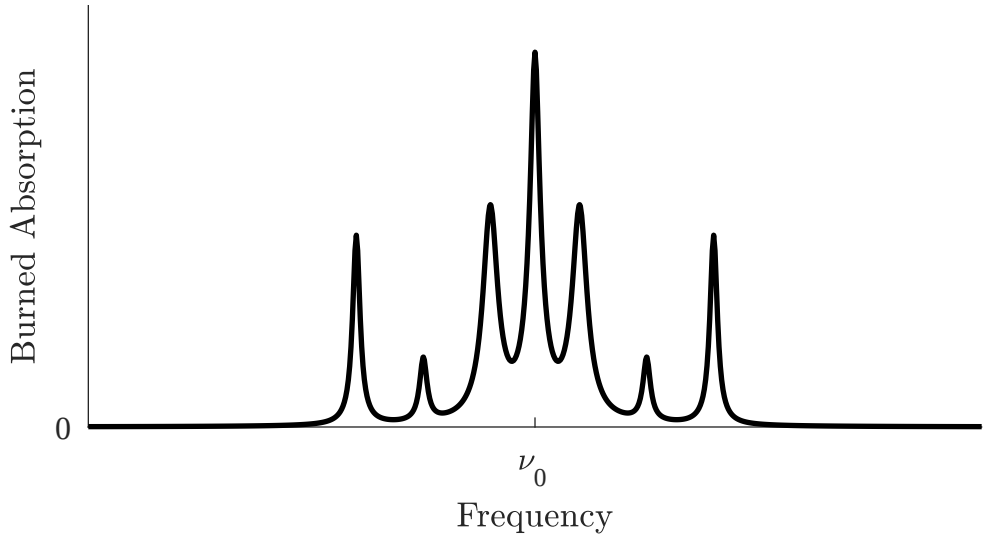

Figure 2.8: The arbitrary absorption pattern seen after the unaltered spectrum is subtracted out from SHB spectrum.

The Hilbert Transform

The next piece of background information that will be discussed is a mathematical tool that readers may not be familiar with: the Hilbert transform. The Hilbert transform is similar to the Fourier transform, in that it is an integral transform and a linear operator. It is used in signal processing. If you have a signal function $u(t)$, it produces the analytic representation of that signal, $\mathcal{H}[u(t)]$. In so doing, it extends the real signal $u(t)$ to the complex plane. Furthermore, $u(t)$ and $\mathcal{H}[u(t)]$ will also satisfy the Cauchy-Riemann equations. Finally, this transform will keep its output in the same domain as the input (i.e. the signal $u(t)$ and its transform $\mathcal{H}[u(t)]$ are both functions of time).

Definition

The Hilbert transform of a signal $u(t)$ is defined as (see [36])

$$v(t) \equiv \mathcal{H}[u(t)] = \frac{1}{\pi}\int_{-\infty}^{\infty}\frac{u(\tau)\mathrm{d}\tau}{t-\tau} = -\frac{1}{\pi}\int_{-\infty}^{\infty}\frac{u(t-\tau')\mathrm{d}\tau'}{\tau'}. \tag{2.29}$$

This can be written with a convolution representation,

$$v(t) = u(t) \otimes \frac{1}{\pi t}. \tag{2.30}$$

Where this becomes useful is in the frequency domain. Using the properties of Fourier transforms, the Fourier transform of (2.30) is

$$\tilde{v}(\nu) = i\tilde{u}(\nu)\,\mathrm{sgn}(\nu). \tag{2.31}$$

Therefore, the Hilbert transform doesn't change the magnitude of $\tilde{u}$. It only gives it a phase shift (and possible sign change). The inverse Hilbert transform is defined as

$$u(t) = \mathcal{H}^{-1}[v(t)] = -\frac{1}{\pi}\int_{-\infty}^{\infty}\frac{v(\tau)\mathrm{d}\tau}{t-\tau} = \frac{1}{\pi}\int_{-\infty}^{\infty}\frac{v(t-\tau')\mathrm{d}\tau'}{\tau'} \tag{2.32}$$

$$= -v(t) \otimes \frac{1}{\pi t}. \tag{2.33}$$

If two functions $u(t)$ and $v(t)$ satisfy (2.29) and (2.32), they are said to be Hilbert pairs of one another.

For an example on using the Hilbert transform, take the function

$$u(t) = \cos(2\pi\nu_0 t). \tag{2.34}$$

Using (2.30),

$$v(t) = \cos(2\pi\nu_0 t) \otimes \frac{1}{\pi t}. \tag{2.35}$$

Taking the Fourier transform

$$\tilde{v}(\nu) = \frac{i}{2}\,\mathrm{sgn}(\nu)(\delta(\nu - \nu_0) + \delta(\nu + \nu_0)). \tag{2.36}$$

Now, when $\nu = \nu_0$, $\mathrm{sgn}(\nu) = 1$, and when $\nu = -\nu_0$, $\mathrm{sgn}(\nu) = -1$. So,

$$\tilde{v}(\nu) = \frac{i}{2}(\delta(\nu - \nu_0) - \delta(\nu + \nu_0)) \tag{2.37}$$

$$= -\frac{1}{2i}(\delta(\nu - \nu_0) - \delta(\nu + \nu_0)). \tag{2.38}$$

Taking the inverse Fourier transform of (2.38),

$$v(t) = -\sin(2\pi\nu_0 t). \tag{2.39}$$

So, the Hilbert transform of a cosine is sine, and the two are Hilbert pairs of one another.

The Cauchy Principal Value

With either the definition from (2.29) or (2.32), an issue arises of mathematical significance–the integrals are improper. A singularity arises when $t = \tau$. To circumvent this technicality, the Cauchy principal value of the integrals is taken, when one exists. The Cauchy principal value (CPV) is defined here as

$$v(t) = \frac{1}{\pi} \lim_{\epsilon \to 0^+} \left(\int_{t-1/\epsilon}^{t-\epsilon} \frac{u(\tau)}{t-\tau} \mathrm{d}\tau + \int_{t+\epsilon}^{t+1/\epsilon} \frac{u(\tau)}{t-\tau} \mathrm{d}\tau \right). \tag{2.40}$$

The same argument applies for (2.32). It is possible for the CPV to exist, but the integral itself not converge. If a Hilbert transform is being performed, it will be taken to mean that the principal value (when it exists) of the limit defined in (2.40) is being taken. As an example of the CPV, evaluate the Hilbert transform of the function

$$\int_{-\infty}^{\infty} \frac{\mathrm{d}\tau}{\tau}. \tag{2.41}$$

This integral clearly has a singularity when $\tau = 0$. Taking the CPV approach, though, one instead finds

$$\int_{-\infty}^{\infty} \frac{\mathrm{d}\tau}{\tau} = \lim_{\epsilon \to 0^+} \left(\int_{t-1/\epsilon}^{t-\epsilon} \frac{\mathrm{d}\tau}{\tau} + \int_{t+\epsilon}^{t+1/\epsilon} \frac{\mathrm{d}\tau}{\tau} \right) \tag{2.42}$$

$$= \lim_{\epsilon \to 0^+} \left(\int_{t-1/\epsilon}^{t-\epsilon} \frac{\mathrm{d}\tau}{\tau} + \int_{-t-\epsilon}^{-t-1/\epsilon} \frac{\mathrm{d}\tau}{\tau} \right) \tag{2.43}$$

$$= \lim_{\epsilon \to 0^+} \left(\int_{t-1/\epsilon}^{t-\epsilon} \frac{\mathrm{d}\tau}{\tau} - \int_{t-1/\epsilon}^{t-\epsilon} \frac{\mathrm{d}\tau}{\tau} \right) \tag{2.44}$$

$$= 0. \tag{2.45}$$

Therefore, a CPV exists for this integral, despite the normal integral being unbounded. Consequently, this also proves that the Hilbert transform of a constant is zero. So, the Hilbert transform removes DC offsets.

Carrier Elimination

Spectral holes occur at frequencies relative to the carrier wave, due to the absorption properties in the crystal. Therefore, it is useful to translate to the carrier frequency, such that $\nu \to \nu - \nu_0$. In simulations, the zero point frequency is, therefore, set so that $\nu_0 = 0$ and it requires the use of complex fields to represent phase properly. However, it must be shown that this gets the same results as modeling the fields on

a carrier.

First, define the real-world input field to be the Fourier sum

$$E_{\text{in}}(t) = \sum_{n=1}^{N} E_{0,n}(t)\cos(\omega_n t + \varphi_n(t)), \tag{2.46}$$

where $\omega_n = 2\pi\nu_n$ is the nth frequency term, $\varphi_n(t)$ is any time-dependent function for the nth term, and $E_{0,n}(t)$ is the nth amplitude. In complex notation, this can be represented by

$$E_{\text{in}}(t) = \sum_{n=1}^{N} \frac{1}{2} E_{0,n}(t)\left(e^{+i(\omega_n t+\varphi_n(t))} + e^{-i(\omega_n t+\varphi_n(t))}\right). \tag{2.47}$$

To show a translation to the carrier frequency can be made, this signal gets multiplied by unity, $1 = e^{+i\omega_0 t}e^{-i\omega_0 t}$:

$$E_{\text{in}}(t) = \sum_{n=1}^{N} \frac{1}{2} E_{0,n}(t)\left(e^{+i\omega_n t}e^{+i\varphi_n(t)}e^{+i\omega_0 t}e^{-i\omega_0 t} + e^{-i\omega_n t}e^{-i\varphi_n(t)}e^{+i\omega_0 t}e^{-i\omega_0 t}\right), \tag{2.48}$$

where $\omega_0 = 2\pi\nu_0$ is the carrier frequency, defined as the zeroth term. Furthermore, define

$$\Delta_n \equiv \omega_n - \omega_0. \tag{2.49}$$

With this, the previous equation can simplify to

$$E_{\text{in}}(t) = \sum_{n=1}^{N} \frac{1}{2} E_{0,n}(t)\left(e^{i\varphi_n(t)}e^{i\Delta_n t}e^{i\omega_0 t} + e^{-i\varphi_n(t)}e^{-i\Delta_n t}e^{-i\omega_0 t}\right). \tag{2.50}$$

Finally, making one more definition, set

$$\tilde{A}_n(t) = E_{0,n}(t)e^{i\varphi_n(t)}e^{i\Delta_n t}, \tag{2.51}$$

$$\tilde{A}_n^*(t) = E_{0,n}(t)e^{-i\varphi_n(t)}e^{-i\Delta_n t}. \tag{2.52}$$

Therefore,

$$E_{\text{in}}(t) = \frac{1}{2}\sum_{n=1}^{N} \tilde{A}_n(t)e^{i\omega_0 t} + \tilde{A}_n^*(t)e^{-i\omega_0 t}. \tag{2.53}$$

Keep in mind that $\tilde{A}_n(t)$ is low-bandwidth.

The next step is to convert this to the frequency domain. Taking the Fourier transform of the input signal

$$E_{\text{in}}(\omega) = \int_{-\infty}^{\infty} E_{\text{in}}(t)e^{-i\omega t}\mathrm{d}t \tag{2.54}$$

$$= \frac{1}{2}\sum_{n=1}^{N}\left[\int_{-\infty}^{\infty} \tilde{A}_n(t)e^{-i(\omega-\omega_0)t}\mathrm{d}t + \int_{-\infty}^{\infty} \tilde{A}_n^*(t)e^{-i(\omega+\omega_0)t}\mathrm{d}t\right]. \tag{2.55}$$

Now, define the first term to be the result of the transform.

$$\tilde{A}(\omega-\omega_0) = \frac{1}{2}\sum_{n=1}^{N}\int_{-\infty}^{\infty} \tilde{A}_n(t)e^{-i(\omega-\omega_0)t}\mathrm{d}t. \tag{2.56}$$

The goal is to write the second integral in terms of (2.56). Taking the conjugate

$$\tilde{A}^*(\omega-\omega_0) = \left(\frac{1}{2}\sum_{n=1}^{N}\int_{-\infty}^{\infty} \tilde{A}_n(t)e^{-i(\omega-\omega_0)t}\mathrm{d}t\right)^* = \frac{1}{2}\sum_{n=1}^{N}\int_{-\infty}^{\infty} \tilde{A}_n^*(t)e^{+i(\omega-\omega_0)t}\mathrm{d}t, \tag{2.57}$$

and setting $\omega = -\omega$,

$$\tilde{A}^*(-\omega - \omega_0) = \frac{1}{2}\sum_{n=1}^{N}\int_{-\infty}^{\infty}\tilde{A}_n^*(t)e^{+i(-\omega-\omega_0)t}\mathrm{d}t = \frac{1}{2}\sum_{n=1}^{N}\int_{-\infty}^{\infty}\tilde{A}_n^*(t)e^{-i(\omega+\omega_0)t}\mathrm{d}t. \quad (2.58)$$

This is, precisely, the second term of (2.55). Hence,

$$E_{\mathrm{in}}(\omega) = \tilde{A}(\omega - \omega_0) + \tilde{A}^*(-\omega - \omega_0). \quad (2.59)$$

At this point, the input signal is finished being manipulated. Now, an output needs to be reached by introducing an arbitrary transfer function $H(\omega)$ as:

$$E_{\mathrm{out}}(\omega) = H(\omega)E_{\mathrm{in}}(\omega). \quad (2.60)$$

Returning back to the time domain by using the inverse Fourier transform,

$$E_{\mathrm{out}}(t) = \int_{-\infty}^{\infty} H(\omega)E_{\mathrm{in}}(\omega)e^{+i\omega t}\mathrm{d}\omega \quad (2.61)$$

$$= \int_{-\infty}^{\infty} H(\omega)\tilde{A}(\omega - \omega_0)e^{+i\omega t}\mathrm{d}\omega + \int_{-\infty}^{\infty} H(\omega)\tilde{A}^*(-\omega - \omega_0)e^{+i\omega t}\mathrm{d}\omega. \quad (2.62)$$

Now, when $\omega \approx \omega_0$, $\tilde{A}(\omega - \omega_0)$ is low bandwidth. Outside of this regime, the value of A is negligible. Similarly, when $\omega \approx -\omega_0$, $\tilde{A}^*(-\omega - \omega_0)$ is low bandwidth. Therefore, the integral does not need to be performed over infinite bounds. Rather, only a small portion of the bandwidth (BW), within a region surrounding ω_0, suffices. So,

$$E_{\mathrm{out}}(t) = \int_{\omega_0-\mathrm{BW}}^{\omega_0+\mathrm{BW}} H(\omega)\tilde{A}(\omega - \omega_0)e^{+i\omega t}\mathrm{d}\omega + \int_{-\omega_0-\mathrm{BW}}^{-\omega_0+\mathrm{BW}} H(\omega)\tilde{A}^*(-\omega - \omega_0)e^{+i\omega t}\mathrm{d}\omega. \quad (2.63)$$

Making the change of variable

$$\Delta = \omega - \omega_0 \tag{2.64}$$

on the first integral, and

$$\Delta' = \omega + \omega_0 \tag{2.65}$$

on the second. Then,

$$\begin{aligned} E_{\text{out}}(t) = &\int_{-\text{BW}}^{+\text{BW}} H(\Delta + \omega_0)\tilde{A}(\Delta)e^{+i(\Delta+\omega_0)t}\text{d}\Delta \\ &+ \int_{-\text{BW}}^{+\text{BW}} H(\Delta' - \omega_0)\tilde{A}^*(-\Delta')e^{+i(\Delta'-\omega_0)t}\text{d}\Delta'. \end{aligned} \tag{2.66}$$

Finally, the fact that the transfer function is related to the susceptibility, which contains the useful property

$$H(-\omega) = H^*(\omega), \tag{2.67}$$

is now used. This is easily verified when applied to the transfer function in (3.45) in Ch. 3. Thus,

$$H(\Delta' - \omega_0) = H^*(-\Delta' + \omega_0). \tag{2.68}$$

This allows (2.66) to be written as

$$\begin{aligned} E_{\text{out}}(t) = &\int_{-\text{BW}}^{+\text{BW}} H(\Delta + \omega_0)\tilde{A}(\Delta)e^{+i(\Delta+\omega_0)t}\text{d}\Delta \\ &+ \int_{-\text{BW}}^{+\text{BW}} H^*(-\Delta' + \omega_0)\tilde{A}^*(-\Delta')e^{+i(\Delta'-\omega_0)t}\text{d}\Delta'. \end{aligned} \tag{2.69}$$

One last measure, make the final variable change $\Delta' = -\Delta$,

$$\begin{aligned} E_{\text{out}}(t) = &\int_{-\text{BW}}^{+\text{BW}} H(\Delta+\omega_0)\tilde{A}(\Delta)e^{+i(\Delta+\omega_0)t}\text{d}\Delta \\ &- \int_{+\text{BW}}^{-\text{BW}} H^*(\Delta+\omega_0)\tilde{A}^*(\Delta)e^{-i(\Delta+\omega_0)t}\text{d}\Delta \end{aligned} \tag{2.70}$$

Combining the integrals, by flipping the sign and bounds on the second,

$$E_{\text{out}}(t) = \int_{-\text{BW}}^{+\text{BW}} H(\Delta+\omega_0)\tilde{A}(\Delta)e^{+i(\Delta+\omega_0)t} + H^*(\Delta+\omega_0)\tilde{A}^*(\Delta)e^{-i(\Delta+\omega_0)t}\text{d}\Delta \tag{2.71}$$

Since the second term is just the complex conjugate of the first term, the over all integrand must be a real-valued function. Thus, using carrier elimination, complex fields has been validated as equivalent to simulating real fields on carriers.

THEORY

In this chapter, the electric-field propagation through an arbitrary spectrally absorbing material is modeled. It serves to illustrate how a laser passing through the programmed crystalline spatial-spectral material would behave. The output intensity after interaction is also examined to describe, in a new analysis, the linear recovery algorithm by Chang et al. [4]. It is here that the limitation of linear recovery is mathematically encountered, leading to the need for nonlinear recovery.

Modeling Electric Field Propagation Through an Absorbing Material

Electric field plane wave propagation (1D) through a homogeneous, isotropic, and linear medium is governed by the following wave equation [36]

$$\frac{\partial^2 E(z,t)}{\partial z^2} - \frac{1}{c_0^2}\frac{\partial^2 E(z,t)}{\partial t^2} = \mu_0 \frac{\partial^2 P(z,t)}{\partial t^2}, \tag{3.1}$$

where E is the electric field, P is the macroscopic polarization, μ_0 is the magnetic permeability of free space, and c_0 is the speed of light in a vacuum. It is possible to solve this partial differential equation as is. However, one may also Fourier transform this, going from the time domain to the frequency domain, while leaving the spatial variable as is. In the end, this makes things easier. (3.1) becomes

$$\mathcal{F}_t\left[\frac{\partial^2 E(z,t)}{\partial z^2}\right] - \mathcal{F}_t\left[\frac{1}{c_0^2}\frac{\partial^2 E(z,t)}{\partial t^2}\right] = \mathcal{F}_t\left[\mu_0 \frac{\partial^2 P(z,t)}{\partial t^2}\right], \tag{3.2}$$

where $\mathcal{F}_t$ indicates taking the Fourier transform in the time-domain, but not the spatial domain. Using the property of Fourier transforms that [38]

$$\mathcal{F}_t\left[\frac{\partial^n}{\partial t^n}E(z,t)\right] = (-i2\pi\nu)^n E(z,\nu), \tag{3.3}$$

one finds

$$\mathcal{F}_t\left[\frac{\partial^2}{\partial t^2}E(z,t)\right] = -4\pi^2\nu^2 E(z,\nu). \tag{3.4}$$

The relationship holds for the polarization, as well. Furthermore, for the spatial derivative, the Leibniz rule states [38]

$$\mathcal{F}_t\left[\frac{\partial^2 E(z,t)}{\partial z^2}\right] = \frac{\partial^2 E(z,\nu)}{\partial z^2}. \tag{3.5}$$

After Fourier transforming (3.1) from time to frequency, one finds

$$\frac{\partial^2 E(z,\nu)}{\partial z^2} + \frac{4\pi^2\nu^2}{c_0^2}E(z,\nu) = -4\pi^2\nu^2\mu_0 P(z,\nu). \tag{3.6}$$

Defining the wave number as $k_0 = 2\pi\nu/c_0$ gives

$$\frac{\partial^2 E(z,\nu)}{\partial z^2} + k_0^2 E(z,\nu) = -4\pi^2\nu^2\mu_0 P(z,\nu). \tag{3.7}$$

With the assumption that the material is linear, the polarization may be written as

$$P(z,\nu) = \epsilon_0\chi(\nu)E(z,\nu), \tag{3.8}$$

where χ is the frequency-dependent electric susceptibility of the material and ϵ_0

is the electric permittivity of free space. To be clear, the *average* spatial electric susceptibility of the material is taken ($\chi(\nu) \equiv \langle \chi(z) \rangle (\nu)$). So,

$$\frac{\partial^2 E(z,\nu)}{\partial z^2} + k_0^2 E(z,\nu) = -4\pi^2 \nu^2 \mu_0 \epsilon_0 \chi(\nu) E(z,\nu). \tag{3.9}$$

Upon using the relationship that $c_0 = 1/\sqrt{\mu_0 \epsilon_0}$,

$$\frac{\partial^2 E(z,\nu)}{\partial z^2} + k_0^2 E(z,\nu) = -k_0^2 \chi(\nu) E(z,\nu). \tag{3.10}$$

Therefore,

$$\frac{\partial^2 E(z,\nu)}{\partial z^2} = -k_0^2 (1 + \chi(\nu)) E(z,\nu). \tag{3.11}$$

This is an elementary differential equation. The solution is

$$E(z,\nu) = C_1(\nu) e^{izk_0\sqrt{1+\chi(\nu)}} + C_2(\nu) e^{-izk_0\sqrt{1+\chi(\nu)}}. \tag{3.12}$$

The coefficients of (3.12) can be functions of frequency. They just must not be z-dependent. Moreover, the units of C_1 and C_2 must be that of electric field units, as a result of the exponential being unitless. Therefore, C_1 and C_2 refer to a frequency-only portion of the electric field. As these terms are associated with a $+$ and $-$ exponential terms, they are relabeled to be $C_1(\nu) = E_+(\nu)$ and $C_2(\nu) = E_-(\nu)$.

Absorption and Dispersion

To continue on with this discussion, the full definition of complex susceptibility for absorbing materials needs to be introduced and examined in greater detail.

Absorbing materials have susceptibility defined by

$$\chi(\nu) \equiv \chi'(\nu) + i\chi''(\nu). \tag{3.13}$$

Susceptibility is a dimensionless quantity and corresponds to a complex permittivity given by $\epsilon = \epsilon_0(1 + \chi)$. For the Tm^{3+}: YAG crystal, an extra χ_0 term is included. This is the background YAG susceptibility around the Tm^{3+}: YAG ions. It varies slowly over the bandwidth of interest, and so it can be considered to be frequency independent. Now, the total wave number through the medium is [36, 37]

$$k = k_0\sqrt{1+\chi} = k_0\sqrt{1+\chi_0+\chi'+i\chi''}. \tag{3.14}$$

Furthermore, define two constants β and α such that

$$k = \beta - i\frac{\alpha}{2}. \tag{3.15}$$

This will permit a way to relate β and α to χ' and χ''. The term α is the absorption coefficient that has been discussed in Ch.'s 1 and 2. With these constants, the intensity of the wave falls off as $|\exp(-ikz)|^2 = |\exp(-i\beta z)\exp(-\alpha z/2)|^2 = \exp(-\alpha z)$. Since the term β effects only the rate at which the phase of the wave changes, this quantity can be related to the effective index of refraction in the material by

$$\beta \equiv nk_0. \tag{3.16}$$

Therefore, (3.14) becomes

$$n - i\frac{\alpha}{2k_0} = \sqrt{1 + \chi_0 + \chi' + i\chi''}. \tag{3.17}$$

Weakly Absorbing Medium A weakly absorbing medium is defined, here, by

$$\chi', \chi'' \ll 1 + \chi_0. \tag{3.18}$$

So, by pulling out the $1 + \chi_0$ term,

$$\sqrt{1 + \chi_0 + \chi' + i\chi''} = \sqrt{1 + \chi_0}\sqrt{1 + \frac{\chi' + i\chi''}{1 + \chi_0}}. \tag{3.19}$$

The first term is just the index of refraction for YAG,

$$n_0 = \sqrt{1 + \chi_0}. \tag{3.20}$$

The square-root can be binomial expanded as

$$n_0\sqrt{1 + \frac{\chi' + i\chi''}{1 + \chi_0}} \approx n_0 + \frac{1}{2n_0}(\chi' + i\chi''). \tag{3.21}$$

Now, grouping the real and imaginary parts of (3.21), and insert this expression into (3.17),

$$n - i\frac{\alpha}{2k_0} = n_0 + \frac{\chi'}{2n_0} + i\frac{\chi''}{2n_0}. \tag{3.22}$$

This easily identifies that, under this regime, there exists a clear relationship between χ'' and α,

$$\chi''(\nu) = -\frac{n_0}{k_0}\alpha(\nu). \tag{3.23}$$

To reiterate, $\chi''(\nu)$ is the average spatial value. So, $\alpha(\nu) \equiv \langle\alpha(z)\rangle(\nu)$, denoting the absorption is taken to be a frequency dependent, average spatial value.

Kramers-Kronig Relations Often, one will have knowledge of the absorption profile, but not detailed knowledge of the dispersion. However, the terms χ' and χ'' turn out to be related to one another. The relations are known as the Kramers-Kronig relations, defined as [36]

$$\chi'(\nu) = \frac{2}{\pi}\int_0^\infty \frac{s\chi''(s)}{s^2-\nu^2}\mathrm{d}s, \tag{3.24}$$

$$\chi''(\nu) = \frac{2}{\pi}\int_0^\infty \frac{\nu\chi'(s)}{\nu^2-s^2}\mathrm{d}s. \tag{3.25}$$

These relations are powerful tools that allow for the determination of the real or imaginary part of the susceptibility, so long the other is known for all frequencies, thereby allowing both the dispersion or absorption profile to be known.

These relations come from fundamental physical symmetries in Maxwell's equations. The time-dependent polarization $P(t)$ is related to the applied, time-dependent electric field $E(t)$ by the factor $\epsilon_0\chi(\nu)$. This relationship is known as a linear shift-invariant system, with a transfer function $H(\nu) = \epsilon_0\chi(\nu)$. Because $P(t)$ and $E(t)$ must be real functions, $\chi(\nu)$ must be symmetric so that $\chi(-\nu) = \chi^*(\nu)$. Since the system is causal, that is nothing can happen before $t = 0$, the real portion of $H(\nu)$ is even, the imaginary portion is odd, and they must be related by the above Kramers-Kronig relations.

The functions (3.24) and (3.25) are actually Hilbert pairs of one another. To demonstrate this, (3.24) is massaged into a traditional form of a Hilbert transform of the function $\chi''(\nu)$, as stated in (2.29):

$$\chi'(\nu) = \frac{2}{\pi}\int_0^\infty \frac{s\chi''(s)}{s^2-\nu^2}\mathrm{d}s \tag{3.26}$$

$$= \frac{1}{\pi}\int_0^\infty \left[\frac{1}{s+\nu}+\frac{1}{s-\nu}\right]\chi''(s)\mathrm{d}s \tag{3.27}$$

$$= \frac{1}{\pi}\left[\int_0^\infty \frac{1}{s+\nu}\chi''(s)\mathrm{d}s + \int_0^\infty \frac{1}{s-\nu}\chi''(s)\mathrm{d}s\right]. \tag{3.28}$$

Examining the first integral in more detail, the fact that $\chi'(\nu)$ is odd, so that $\chi'(-\nu) = -\chi'(\nu)$, is now of importance. Since the integral is a linear transformation, they must also exhibit the same property of being odd in ν. Therefore,

$$\int_0^\infty \frac{\chi''(s)\mathrm{d}s}{s+\nu} = -\int_0^\infty \frac{\chi''(s)\mathrm{d}s}{s-\nu} = \int_{-\infty}^0 \frac{\chi''(s)\mathrm{d}s}{s-\nu}, \tag{3.29}$$

where the fact that the integrand itself is also odd was used, and so the minus sign can act to flip the bounds. Combining the integrals,

$$\chi'(\nu) = \frac{1}{\pi}\int_{-\infty}^\infty \frac{\chi''(s)\mathrm{d}s}{s-\nu} = \mathcal{H}[\chi''(\nu)] = -\frac{n_0}{k_0}\mathcal{H}[\alpha(\nu)], \tag{3.30}$$

which proves they are Hilbert pairs. The fact that χ' is the Hilbert transform of the absorption is very important, as it provides an avenue to solve for the dispersion of a system, given the absorption. Thus,

$$k_0\sqrt{1+\chi(\nu)} = k_0 n_0 - \frac{1}{2}\left(i\alpha(\nu) + \mathcal{H}[\alpha(\nu)]\right). \tag{3.31}$$

As a further example of the utility of (3.30), consider a Lorentzian absorption

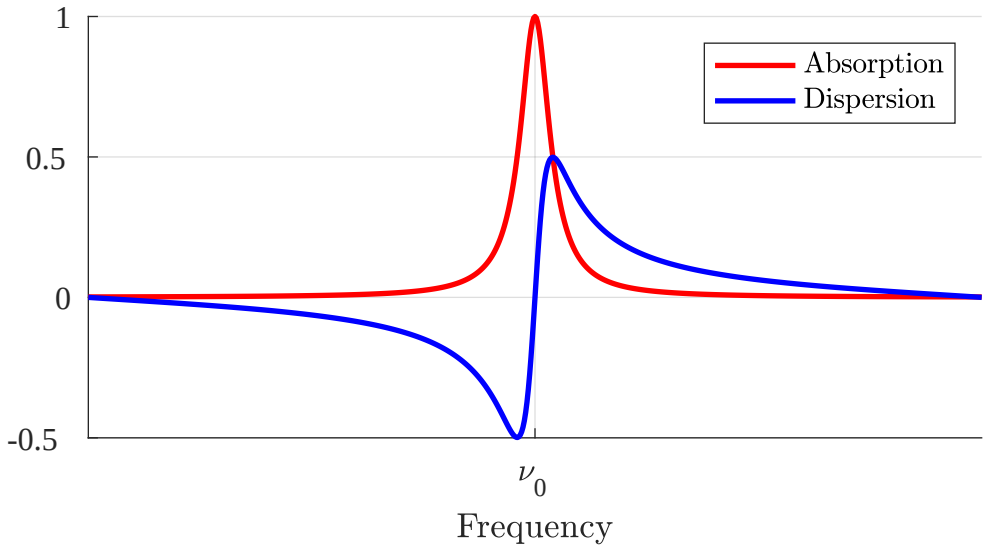

Figure 3.1: Example of using the Hilbert transform on the absorption profile to get the dispersion profile, demonstrating the Kramers-Kronig relationship.

spectrum. Then, the dispersion from this spectrum is plotted in Fig. 3.1. It is exactly what would be expected for complex form of a Lorentzian. This dispersion profile was found only by taking the Hilbert transform on the absorption.

The Transfer Function

Now that the argument of the exponential terms from (3.12) has been examined and fleshed out, the discussion returns to the electric field propagation. Substituting (3.31) into (3.12),

$$\begin{aligned} E(z,\nu) = E_+(\nu)\exp\left(+iz\left[k_0 n_0 - \frac{1}{2}\left(i\alpha(\nu) + \mathcal{H}[\alpha(\nu)]\right)\right]\right) \\ + E_-(\nu)\exp\left(-iz\left[k_0 n_0 - \frac{1}{2}\left(i\alpha(\nu) + \mathcal{H}[\alpha(\nu)]\right)\right]\right). \end{aligned} \tag{3.32}$$

Now, consider two monochromatic waves such that

$$E_+(t) = A_+ e^{i2\pi\nu_0 t} \quad \text{and} \quad E_-(t) = A_- e^{i2\pi\nu_0 t}, \tag{3.33}$$

where A_+ and A_- are amplitudes. Then, the Fourier transform of this wave is

$$E_+(\nu) = A_+\delta(\nu - \nu_0) \quad \text{and} \quad E_-(\nu) = A_-\delta(\nu - \nu_0). \tag{3.34}$$

So,

$$\begin{aligned} E(z,\nu) = A_+\delta(\nu-\nu_0)\exp\left(+iz\left[k_0n_0 - \frac{1}{2}\left(i\alpha(\nu) + \mathcal{H}[\alpha(\nu)]\right)\right]\right) \\ + A_-\delta(\nu-\nu_0)\exp\left(-iz\left[k_0n_0 - \frac{1}{2}\left(i\alpha(\nu) + \mathcal{H}[\alpha(\nu)]\right)\right]\right). \end{aligned} \tag{3.35}$$

If this expression is inverse Fourier transformed back from the frequency domain to the time domain, then

$$E(z,t) = A_+e^{i(2\pi\nu_0 t + k_0n_0z)}e^{+\frac{z}{2}(\alpha(\nu_0) - i\mathcal{H}[\alpha(\nu_0)])} + A_-e^{i(2\pi\nu_0 t - k_0n_0z)}e^{-\frac{z}{2}(\alpha(\nu_0) - i\mathcal{H}[\alpha(\nu_0)])}. \tag{3.36}$$

The exponentials involving the absorption are now only functions of z. Now, if ν_0 is a value that is far off resonance in the material, then

$$e^{+\frac{z}{2}(\alpha(\nu_0) - i\mathcal{H}[\alpha(\nu_0)])} \approx e^{-\frac{z}{2}(\alpha(\nu_0) - i\mathcal{H}[\alpha(\nu_0)])} \approx 1. \tag{3.37}$$

This leads to

$$E(z,t) = A_+e^{i(2\pi\nu_0 t + k_0n_0z)} + A_-e^{i(2\pi\nu_0 t - k_0n_0z)}. \tag{3.38}$$

If a point of constant phase (say φ) is considered for the first term, then

$$2\pi\nu_0 t + k_0n_0z = \varphi. \tag{3.39}$$

This can be rearranged to solve for z, as

$$z = \frac{1}{k_0 n_0}(\varphi - 2\pi\nu_0 t). \tag{3.40}$$

The group velocity for the first term is, therefore,

$$v_{g1} = \frac{\mathrm{d}z}{\mathrm{d}t} = -\frac{2\pi\nu_0}{k_0 n_0}. \tag{3.41}$$

Similarly, the group velocity for the second term is found to be

$$v_{g2} = +\frac{2\pi\nu_0}{k_0 n_0}. \tag{3.42}$$

Since the group velocity on the first term is negative, it refers to a backwards propagation. Meanwhile, the second term refers to forward propagation. As the goal is to model electric field propagation into the material (to be later sent to a detector only existing on one side of the material), the backward propagating term is neglected–the laser is only being sent in one direction. So, the E_+ term is going to be removed, while retaining the E_- term.

By taking $z = L$, where L is full length of the material, the output through the whole material is found. Then, the $\exp(-ik_0 n_0 L)$ term is just an overall constant phase shift. The electric field into the material may be redefined such that

$$E_{\mathrm{in}}(\nu) = \exp(+ik_0 n_0 L) E'_{\mathrm{in}}(\nu), \tag{3.43}$$

so that this term may be ignored. Therefore,

$$E_{\mathrm{out}}(\nu) = E_{\mathrm{in}}(\nu) \exp\left(-\frac{L}{2}\left(\alpha(\nu) - i\mathcal{H}[\alpha(\nu)]\right)\right), \tag{3.44}$$

where $E_{\text{out}}(\nu)$ is the electric field exiting the material. Hence, the transfer function, which describes the behavior of the system independent from any input, is

$$H(\nu) \equiv \frac{E_{\text{out}}(\nu)}{E_{\text{in}}(\nu)} = \exp\left(-\frac{L}{2}\left(\alpha(\nu) - i\mathcal{H}[\alpha(\nu)]\right)\right). \tag{3.45}$$

This leaves an expression that consists only of parameters intrinsic to the material. Furthermore, it eliminates the need to consider the spatially dependent electric field, as this analysis describes that behavior for a specific length of crystal. It should be noted that (3.45) includes the polarization for the input field and the full response of the medium.

Effect of an Arbitrary Absorption Profile on an Electric Field

In this section, how an arbitrary absorption profile effects an electric field is explored. To accomplish this, analysis of Eqn. (3.44) is carried out. Ultimately, a model of what a detector will see, which is power–proportional to $|E(t)|^2$, is sought. So, the result after returning to the time domain will be taken as the absolute value squared.

To start this model, there does need to be some more explanation of how the absorption spectrum is defined. The inhomogeneous spectrum will have a peak value $\alpha_0 L$, defined by the material itself. The model to be constructed is what happens when an arbitrary spectrum is burned into the inhomogeneous spectrum. Define an arbitrary spectrum as a series of Lorentzian-shaped spectral holes ℓ_m, each with width equal to the homogeneous linewidth of the material. Then, the arbitrary spectrum is

$$\mathcal{A}(\nu) = \sum_{m=1}^{N} \ell_m(\nu - \nu_m), \tag{3.46}$$

where each Lorentzian is centered around a frequency ν_m and is normalized to the inhomogeneous spectrum peak $\alpha_0 L$. So, for any given m,

$$\ell_m(\nu - \nu_m) = \frac{\beta_m}{1 + \left(\frac{\nu - \nu_m}{\Gamma_H/2}\right)^2}, \tag{3.47}$$

where β_m is real number between 0 and 1, giving the percent of $\alpha_0 L$ the mth Lorentzian is normalized to. Define the spacing between the frequencies to be

$$|\nu_{m+1} - \nu_m| \geq \Gamma_H. \tag{3.48}$$

Therefore, the inhomogeneous spectrum becomes

$$\alpha(\nu)L = \alpha_0 L(1 - \mathcal{A}(\nu)). \tag{3.49}$$

Inserting (3.49) in (3.44),

$$E_{\text{out}}(\nu) = E_{\text{in}}(\nu) \exp\left(-\frac{1}{2}\left(\alpha_0 L(1 - \mathcal{A}(\nu)) - i\mathcal{H}[\alpha_0 L(1 - \mathcal{A}(\nu))]\right)\right). \tag{3.50}$$

The term $\mathcal{H}[\alpha_0 L]$ is the Hilbert transform of a constant, and so it's evaluated to be zero. Therefore,

$$E_{\text{out}}(\nu) = E_{\text{in}}(\nu) e^{-\alpha_0 L/2} e^{\frac{\alpha_0 L}{2}(\mathcal{A}(\nu) - i\mathcal{H}[\mathcal{A}(\nu)])}. \tag{3.51}$$

Now, a mathematical trick is played by adding and subtracting one from the second exponential term.

$$E_{\text{out}}(\nu) = E_{\text{in}}(\nu) e^{-\alpha_0 L/2}\left[e^{\frac{\alpha_0 L}{2}(\mathcal{A}(\nu) - i\mathcal{H}[\mathcal{A}(\nu)])} - 1 + 1\right]. \tag{3.52}$$

Then,

$$E_{\text{out}}(\nu) = \underbrace{E_{\text{in}}(\nu)e^{-\alpha_0 L/2}}_{E_B(\nu)} + \underbrace{E_{\text{in}}(\nu)e^{-\alpha_0 L/2}\left[e^{\frac{\alpha_0 L}{2}(\mathcal{A}(\nu)-i\mathcal{H}[\mathcal{A}(\nu)])}-1\right]}_{E_H(\nu)}. \tag{3.53}$$

Now, the reason for adding and subtracting one is clear. It allows the parts of the field that are due to the background to be separated from the field that is resultant from the spectral holes. Label the first term as $E_B(\nu)$ and the second $E_H(\nu)$. The output of this in the time domain is found by inverse transforming back.

$$E_{\text{out}}(t) = \mathcal{F}^{-1}\left[E_B(\nu)\right] + \mathcal{F}^{-1}\left[E_H(\nu)\right]. \tag{3.54}$$

Label the first term as $E_B(t) = \mathcal{F}^{-1}\left[E_B(\nu)\right]$ and the second $E_H(t) = \mathcal{F}^{-1}\left[E_H(\nu)\right]$. So,

$$E_{\text{out}}(t) = E_B(t) + E_H(t). \tag{3.55}$$

The field intensity is what is needed. So,

$$|E_{\text{out}}(t)|^2 = |E_B(t)|^2 + |E_H(t)|^2 + E_B^*(t)E_H(t) + E_B(t)E_H^*(t). \tag{3.56}$$

Now, in the end, this output will be measured by a balance detector, which removes the background term. Therefore, after balance detection, the resultant intensity is

$$|E_{\text{out}}(t)|^2 = |E_H(t)|^2 + E_B^*(t)E_H(t) + E_B(t)E_H^*(t). \tag{3.57}$$

The expression in (3.57) can be thought of as what the time domain intensity appears

as, after balance detection. The expression is, therefore, relabeled

$$P_{\text{det}}(t) = |E_H(t)|^2 + E_B^*(t)E_H(t) + E_B(t)E_H^*(t). \tag{3.58}$$

This is the expression for which recovery needs to occur. The intensity from E_H is what needs to be isolated. So, the cross terms are what mess the signal up, from this perspective.

Take one of the cross terms for examination. Recovery takes place in the Fourier domain. So, Fourier transforming it back [38]

$$\mathcal{F}[E_B^*(t)E_H(t)] = \frac{1}{\sqrt{2\pi}}\mathcal{F}[E_B^*(t)] \otimes \mathcal{F}[E_H(t)] = \frac{1}{\sqrt{2\pi}}\int_{-\infty}^{\infty} E_B^*(f)E_H(f+\nu)\mathrm{d}f. \tag{3.59}$$

Substituting in,

$$\mathcal{F}[E_B^*(t)E_H(t)] = \frac{e^{-\alpha_0 L}}{\sqrt{2\pi}}\int_{-\infty}^{\infty} \underbrace{E_{\text{in}}^*(f)}_{E_B^*(f)} \underbrace{E_{\text{in}}(f+\nu)\left[e^{\frac{\alpha_0 L}{2}(\mathcal{A}(f+\nu)-i\mathcal{H}[\mathcal{A}(f+\nu)])}-1\right]}_{E_H(f+\nu)}\mathrm{d}f. \tag{3.60}$$

The other cross term is

$$\mathcal{F}[E_B(t)E_H^*(t)] = \frac{e^{-\alpha_0 L}}{\sqrt{2\pi}}\int_{-\infty}^{\infty} E_{\text{in}}^*(f)E_{\text{in}}(f+\nu)\left[e^{\frac{\alpha_0 L}{2}(\mathcal{A}(f)+i\mathcal{H}[\mathcal{A}(f)])}-1\right]\mathrm{d}f. \tag{3.61}$$

For the Fourier transform of the term $|E_H(t)|^2$, the integral that needs to be considered

is

$$|E_H(t)|^2 = \frac{e^{-\alpha_0 L}}{\sqrt{2\pi}} \int_{-\infty}^{\infty} E_{\text{in}}^*(f) E_{\text{in}}(f+\nu) \left[e^{\frac{\alpha_0 L}{2}(\mathcal{A}(f)+i\mathcal{H}[\mathcal{A}(f)])} - 1 \right] \times \left[e^{\frac{\alpha_0 L}{2}(\mathcal{A}(f+\nu)-i\mathcal{H}[\mathcal{A}(f+\nu)])} - 1 \right] \mathrm{d}f. \tag{3.62}$$

The product of the exponentials is

$$\begin{aligned} &\left[e^{\frac{\alpha_0 L}{2}(\mathcal{A}(f)+i\mathcal{H}[\mathcal{A}(f)])} - 1 \right] \left[e^{\frac{\alpha_0 L}{2}(\mathcal{A}(f+\nu)-i\mathcal{H}[\mathcal{A}(f+\nu)])} - 1 \right] \\ &\qquad = 1 - e^{\frac{\alpha_0 L}{2}(\mathcal{A}(f)+i\mathcal{H}[\mathcal{A}(f)])} - e^{\frac{\alpha_0 L}{2}(\mathcal{A}(f+\nu)-i\mathcal{H}[\mathcal{A}(f+\nu)])} \\ &\qquad + e^{\frac{\alpha_0 L}{2}(\mathcal{A}(f)+i\mathcal{H}[\mathcal{A}(f)])} e^{\frac{\alpha_0 L}{2}(\mathcal{A}(f+\nu)-i\mathcal{H}[\mathcal{A}(f+\nu)])}. \end{aligned} \tag{3.63}$$

Now, notice that the second and third terms in (3.63) equal the negative of the exponentials in $\mathcal{F}[E_B^*(t)E_H(t)]$ and $\mathcal{F}[E_B(t)E_H^*(t)]$. Hence, except having a minus sign out front in the total intensity, they cancel these terms. So, in the total intensity an extra -2 term is picked up, the cross terms cancel, and everything may be brought under a single integral. Therefore, the transform of the detected power is exactly

$$\mathcal{F}[P_{\text{det}}(t)] = \frac{e^{-\alpha_0 L}}{\sqrt{2\pi}} \int_{-\infty}^{\infty} E_{\text{in}}^*(f) E_{\text{in}}(f+\nu) \left[e^{\frac{\alpha_0 L}{2}(\mathcal{A}(f)+i\mathcal{H}[\mathcal{A}(f)]+\mathcal{A}(f+\nu)-i\mathcal{H}[\mathcal{A}(f+\nu)])} - 1 \right] \mathrm{d}f. \tag{3.64}$$

I would like to stress that this is a generic expression for the Fourier transform of the detected power for any input field. For a chirp input field of

$$E_{\text{in}}(t) = e^{i(2\pi\nu_0 t + \pi\kappa t^2)}, \tag{3.65}$$

its Fourier transform is functionally

$$E_{\text{in}}(\nu) = e^{-i\pi(\nu-\nu_0)^2/\kappa}, \tag{3.66}$$

up to some scaling terms. Then, the product of fields is

$$E^*_{\text{in}}(f)E_{\text{in}}(f+\nu) = e^{-i\pi(\nu^2-2\nu_0\nu)/\kappa}e^{-i2\pi\nu f/\kappa}. \tag{3.67}$$

So,

$$\mathcal{F}[P_{\text{det}}(t)] = \frac{e^{-\alpha_0 L}}{\sqrt{2\pi}}e^{\frac{-i\pi(\nu^2-2\nu_0\nu)}{\kappa}}\int_{-\infty}^{\infty} e^{\frac{-i2\pi\nu f}{\kappa}}\left[e^{\frac{\alpha_0 L}{2}(\mathcal{A}(f)+i\mathcal{H}[\mathcal{A}(f)]+\mathcal{A}(f+\nu)-i\mathcal{H}[\mathcal{A}(f+\nu)])}-1\right]\mathrm{d}f. \tag{3.68}$$

First-Order Absorption

There are two absorption regimes to consider. The first is for low, first-order absorption. That is, a small $\alpha(\nu)L$. In this regime, the exponential term from (3.50) is approximated to be

$$e^{\frac{\alpha_0 L}{2}(\mathcal{A}(\nu)-i\mathcal{H}[\mathcal{A}(\nu)])} \approx 1 + \frac{\alpha_0 L}{2}\left(\mathcal{A}(\nu) - i\mathcal{H}[\mathcal{A}(\nu-\nu_H)]\right). \tag{3.69}$$

With linearization, each Lorentzian can be taken individually. So, instead of using a collection of Lorentzians, a single Lorentzian hole becomes the focus, $\mathcal{A}(\nu) = \ell(\nu)$. Then, the Lorentzian plus its Hilbert pair can be written

$$\ell(\nu-\nu_H) - i\mathcal{H}[\ell(\nu-\nu_H)] \propto \frac{1}{\Gamma + i(\nu-\nu_H)}, \tag{3.70}$$

where Γ is the spectral hole width. To prove this is true, observe

$$\frac{1}{\Gamma + i(\nu - \nu_H)} = \frac{\Gamma - i(\nu - \nu_H)}{\Gamma^2 + (\nu - \nu_H)^2} = \frac{\Gamma}{1 + \left(\frac{\nu - \nu_H}{\Gamma}\right)^2} - \frac{i(\nu - \nu_H)}{1 + \left(\frac{\nu - \nu_H}{\Gamma}\right)^2}. \tag{3.71}$$

The first term may be considered absorption, while the second term is dispersion. It was already proved they are related through Kramers-Kronig. Now, the exponential term in (3.68) becomes

$$e^{\frac{\alpha_0 L}{2}(\ell(f-\nu_H)+i\mathcal{H}[\ell(f-\nu_H)]+\ell(f+\nu-\nu_H)-i\mathcal{H}[\ell(f+\nu-\nu_H)])} - 1 \propto \frac{\alpha_0 L/2}{\Gamma - i(f - \nu_H)} + \frac{\alpha_0 L/2}{\Gamma + i(f + \nu - \nu_H)}. \tag{3.72}$$

Now, for convienence, set $f' = f - \nu_H$. Then, the integral from (3.68) is evaluated to be

$$e^{-i2\pi\nu\frac{\nu_H}{\kappa}} \int_{-\infty}^{\infty} e^{-i2\pi\nu f'/\kappa} \left(\frac{1}{\Gamma - if'} + \frac{1}{\Gamma + i(f' + \nu)}\right) \mathrm{d}f' \propto 2\pi e^{-i2\pi\nu\frac{\nu_H}{\kappa}} \begin{cases} e^{-2\pi\Gamma\frac{\nu}{\kappa}}, & \nu > 0 \\ e^{2\pi\Gamma\frac{\nu}{\kappa}} e^{i2\pi\frac{\nu^2}{\kappa}}, & \nu < 0. \end{cases} \tag{3.73}$$

Positive Frequencies For $\nu > 0$,

$$\mathcal{F}[P_{\mathrm{det}}(t)] = \sqrt{\frac{\pi}{2}} \alpha_0 L e^{-\alpha_0 L} e^{-i\pi(\nu^2 - 2\nu_0\nu)/\kappa} e^{-2\pi\Gamma\frac{\nu}{\kappa}} e^{-i2\pi\nu\frac{\nu_H}{\kappa}}. \tag{3.74}$$

Now, from Chang et al. the linear recovery algorithm can now come into play. The multiplicative factor is defined as

$$\text{Linear Recovery} \equiv \exp\left[i\frac{\pi}{\kappa}\left(\mathrm{sgn}(\nu)\nu^2 - 2\nu_0\nu\right)\right]. \tag{3.75}$$

Multiplying (3.75) into (3.74),

$$\mathcal{F}[P_{\text{det}}(t)]_{\text{rec}} = \sqrt{\frac{\pi}{2}}\alpha_0 L e^{-\alpha_0 L} e^{-i\pi(\nu^2-2\nu_0\nu)/\kappa} e^{i\pi(\nu^2-2\nu_0\nu)/\kappa} e^{-2\pi\Gamma\frac{\nu}{\kappa}} e^{-i2\pi\nu\frac{\nu_H}{\kappa}}, \tag{3.76}$$

which simplifies to

$$\mathcal{F}[P_{\text{det}}(t)]_{\text{rec}} = \sqrt{\frac{\pi}{2}}\alpha_0 L e^{-\alpha_0 L} e^{-2\pi\Gamma\frac{\nu}{\kappa}} e^{-i2\pi\nu\frac{\nu_H}{\kappa}}. \tag{3.77}$$

Therefore, for positive frequencies, the recovered power spectrum in time is

$$P_{\text{rec},\nu>0}(t) = \sqrt{\frac{\pi}{2}}\alpha_0 L e^{-\alpha_0 L} \int_0^\infty e^{-2\pi\Gamma\frac{\nu}{\kappa}} e^{i2\pi\nu(t-\nu_H/\kappa)} \mathrm{d}\nu. \tag{3.78}$$

Negative Frequencies When $\nu < 0$,

$$\mathcal{F}[P_{\text{det}}(t)] = \sqrt{\frac{\pi}{2}}\alpha_0 L e^{-\alpha_0 L} e^{-i\pi(\nu^2-2\nu_0\nu)/\kappa} e^{2\pi\Gamma\frac{\nu}{\kappa}} e^{i2\pi\frac{\nu^2}{\kappa}} e^{-i2\pi\nu\frac{\nu_H}{\kappa}}. \tag{3.79}$$

Factoring in the linear recovery

$$\mathcal{F}[P_{\text{det}}(t)]_{\text{rec}} = \sqrt{\frac{\pi}{2}}\alpha_0 L e^{-\alpha_0 L} e^{-i\pi(\nu^2-2\nu_0\nu)/\kappa} e^{-i\pi(\nu^2+2\nu_0\nu)/\kappa} e^{2\pi\Gamma\frac{\nu}{\kappa}} e^{i2\pi\frac{\nu^2}{\kappa}} e^{-i2\pi\nu\frac{\nu_H}{\kappa}}, \tag{3.80}$$

and simplifying

$$\mathcal{F}[P_{\text{det}}(t)]_{\text{rec}} = \sqrt{\frac{\pi}{2}}\alpha_0 L e^{-\alpha_0 L} e^{2\pi\Gamma\frac{\nu}{\kappa}} e^{-i2\pi\nu\frac{\nu_H}{\kappa}}. \tag{3.81}$$

Converting back to the time domain,

$$P_{\text{rec},\nu<0}(t) = \sqrt{\frac{\pi}{2}}\alpha_0 L e^{-\alpha_0 L} \int_{-\infty}^0 e^{2\pi\Gamma\frac{\nu}{\kappa}} e^{i2\pi\nu(t-\nu_H/\kappa)} \mathrm{d}\nu. \tag{3.82}$$

Linear Recovery The integrals in (3.78) and (3.82) can be combined for a single expression of recovery

$$P_{\text{rec}}(t) = \sqrt{\frac{\pi}{2}}\alpha_0 L e^{-\alpha_0 L} \int_{-\infty}^{\infty} e^{-2\pi\Gamma\frac{|\nu|}{\kappa}} e^{i2\pi\nu(t-\nu_H/\kappa)} \mathrm{d}\nu. \tag{3.83}$$

The integral is the Fourier transform of a decaying exponential, which is known to be a Lorentzian. One definitional change is made here. Define $t_H = \nu_H/\kappa$. Then, the recovered power is

$$P_{\text{rec}}(t) = \sqrt{\frac{\pi}{2}}\alpha_0 L e^{-\alpha_0 L} \ell(t - t_H). \tag{3.84}$$

Collect the constants such that

$$C = \sqrt{\frac{\pi}{2}} e^{-\alpha_0 L}. \tag{3.85}$$

Then

$$P_{\text{rec}}(t) = C\alpha_0 L \ell(t - t_H). \tag{3.86}$$

Therefore, at low absorption, this recovery algorithm restores the spectrum identically, up to some scaling factors out front. For a collection of Lorentzians, you simply need to sum this result of (3.84) for the number of Lorentzians you have.

Higher-Order Absorption

For higher absorbing materials, (3.69) needs to be taken out to higher order. Up to second order,

$$e^{\frac{\alpha_0 L}{2}(\mathcal{A}(\nu)-i\mathcal{H}[\mathcal{A}(\nu)])} \approx 1 + \frac{\alpha_0 L}{2}\left(\mathcal{A}(\nu) - i\mathcal{H}[\mathcal{A}(\nu)]\right) + \frac{(\alpha_0 L)^2}{8}\left(\mathcal{A}(\nu) - i\mathcal{H}[\mathcal{A}(\nu)]\right)^2. \tag{3.87}$$

For a single Lorentzian hole, (3.72) now becomes

$$\begin{aligned} e^{\frac{\alpha_0 L}{2}(\ell(f-\nu_H)+i\mathcal{H}[\ell(f-\nu_H)]+\ell(f+\nu-\nu_H)-i\mathcal{H}[\ell(f+\nu-\nu_H)])} - 1 \propto \frac{\alpha_0 L/2}{\Gamma - i(f-\nu_H)} \cdots \\ \cdots + \frac{\alpha_0 L/2}{\Gamma + i(f+\nu-\nu_H)} + \frac{1}{2}\left(\frac{\alpha_0 L/2}{\Gamma - i(f-\nu_H)}\right)^2 + \frac{1}{2}\left(\frac{\alpha_0 L/2}{\Gamma + i(f+\nu-\nu_H)}\right)^2. \end{aligned} \tag{3.88}$$

So, (3.73) becomes

$$\begin{aligned} e^{-i2\pi\nu t_H}\int_{-\infty}^{\infty} e^{-i2\pi\nu f'/\kappa}\left(\frac{\alpha_0 L/2}{\Gamma - if'} + \frac{\alpha_0 L/2}{\Gamma + i(f'+\nu)} + \frac{1}{2}\left(\frac{\alpha_0 L/2}{\Gamma - if'}\right)^2\right. \\ \left. + \frac{1}{2}\left(\frac{\alpha_0 L/2}{\Gamma + i(f'+\nu)}\right)^2\right) \mathrm{d}f' \propto \frac{\pi}{2}\alpha_0 L e^{-i2\pi\nu t_H} \\ \times \begin{cases} e^{-2\pi\Gamma\frac{\nu}{\kappa}}\left[2 + \frac{\pi\nu}{\kappa}\alpha_0 L\left(1 + e^{i2\pi\frac{\nu^2}{\kappa}}\right)\right], & \nu > 0 \\ 2e^{2\pi\Gamma\frac{\nu}{\kappa}} e^{i2\pi\frac{\nu^2}{\kappa}}, & \nu < 0. \end{cases} \end{aligned} \tag{3.89}$$

The result now contains additional terms. Comparing this with (3.73), the first term for positive frequencies will combine with the negative-frequency term to return first-order absorption. The second term for positive frequencies will return other terms. This gives,

$$P_{\mathrm{rec}}(t) \propto \ell(t - t_H) + \text{other terms}. \tag{3.90}$$

From these other terms, even at just a second-order approximation, the original recovery method fails to accurately return the desired spectrum. This is the cause of the distortions. This also demonstrates why the recovery method from Chang et al. is referred to as "linear recovery," as it fails for orders of 2 and higher in $\Delta\alpha(\nu)L$. Therefore a solution that accounts for higher-order terms is sought.

Finding a Higher Order Recovery

To motivate how a higher-order recovery algorithm can be found, this discussion needs to take a step back. One can imagine a fast chirp scanning across a single spectral hole, such that $\kappa \gg \Gamma^2$, in some sense would be like a brief pulse incident on the Lorentzian spectral hole. This can be modeled as

$$E_{\text{in}}(t) = \delta(t - t_H)e^{i2\pi\nu_H t}. \tag{3.91}$$

Then, the Fourier transform of this is

$$E_{\text{in}}(\nu) = e^{-i2\pi(\nu-\nu_H)t_H}. \tag{3.92}$$

Under the formulation of a single Lorentzian hole, and assuming low absorption, (3.55) is used to find the output. So, the interaction between the spectral hole and this "impulse-like" response would be

$$E_H(t) = e^{-\alpha_0 L/2}\int_{-\infty}^{\infty}\frac{e^{-i2\pi(\nu-\nu_H)t_H}}{\Gamma + i(\nu-\nu_H)}e^{i2\pi\nu t}\mathrm{d}\nu. \tag{3.93}$$

By change of variable,

$$E_H(t) = e^{-\alpha_0 L/2} e^{i2\pi\nu_H t} \int_{-\infty}^{\infty} \frac{e^{-i2\pi\nu' t_H}}{\Gamma + i\nu'} e^{i2\pi\nu' t} \mathrm{d}\nu' = e^{-\alpha_0 L/2} e^{i2\pi\nu_H t} e^{-\Gamma(t-t_H)} u(t-t_H), \tag{3.94}$$

where u is the Heaviside function. Now, the background field–which is a chirp, without any interaction from the hole would be

$$E_B(t) = e^{-\alpha_0 L/2} e^{i(2\pi\nu_H t + \pi\kappa t^2)}. \tag{3.95}$$

So, by (3.58),

$$P_{\mathrm{det}} = e^{-\alpha_0 L} e^{-2\Gamma(t-t_H)} u(t-t_H) + e^{-\alpha_0 L} e^{-\Gamma(t-t_H)} e^{-i\pi\kappa t^2} u(t-t_H) + \mathrm{c.c.} \tag{3.96}$$

Ignore the constants, as this is only meant to be an approximate formalism. Then

$$P_{\mathrm{det}} \propto \underbrace{e^{-\Gamma(t-t_H)} \cos(\pi\kappa t^2) u(t-t_H)}_{\text{Ringout}} + \underbrace{e^{-2\Gamma(t-t_H)} u(t-t_H)}_{\text{FID}}. \tag{3.97}$$

The second term represents the intensity of the free induction decay from the spectral hole. The first term can be considered a beating between the spectral hole FID and the background chirp, causing the chirped ringing. The linear recovery removes the ringing behavior, leaving behind the spectral hole and the FID term,

$$P_{\mathrm{rec}} \propto \underbrace{e^{-\Gamma(t-t_H)} u(t-t_H)}_{\text{Spectral hole}} + \underbrace{e^{-2\Gamma(t-t_H)} u(t-t_H)}_{\text{Want to remove}}. \tag{3.98}$$

This can be thought of as also causing the nonlinear tail. So, the goal is to try to

find a way to remove the FID term. To start, take the Hilbert transform of (3.97),

$$\mathcal{H}[P_{\text{det}}(t)] \simeq e^{-\Gamma(t-t_H)} \sin(\pi\kappa t^2) u(t-t_H) + e^{-2\Gamma(t-t_H)} u(t-t_H). \tag{3.99}$$

It's worth noting that this is not an exact expression. The exponential has not been taken into account. This is just to get a feel for how the spectral hole term can be isolated.

By squaring (3.97) and (3.99), taking $t > t_H$ for brevity, and adding them, one finds

$$P_{\text{det}}(t)^2 + \mathcal{H}[P_{\text{det}}(t)]^2 \simeq e^{-2\Gamma(t-t_H)} + e^{-3\Gamma(t-t_H)}(\sin(\pi\kappa t^2) + \cos(\pi\kappa t^2)) + e^{-4\Gamma(t-t_H)}. \tag{3.100}$$

From the sinusoidal term, there is still ringing present here. If this term is recovered with the linear recovery method, one ends up with a nonlinear term that is consistent with a higher order exponential decay. This is labeled as

$$P_{\text{FID}}(t) \equiv [P_{\text{det}}(t)^2 + \mathcal{H}[P_{\text{det}}(t)]^2]_{\text{rec}} \tag{3.101}$$

$$\propto \underbrace{e^{-2\Gamma(t-t_H)}}_{\text{Want to remove}} + \underbrace{e^{-3\Gamma(t-t_H)} + e^{-4\Gamma(t-t_H)}}_{\text{Higher-order terms}}. \tag{3.102}$$

The quantity P_{FID} yields an expression that includes the term that needs to be removed from (3.98), as well as higher-order terms. If this term is then subtracted from the linearly recovered term, then this would work to isolate the spectral term, now with even higher-order terms that don't contribute and can be ignored. This provides the pathway for nonlinear correction.

The definition of nonlinear recovery is presented as:

$$P_{\mathrm{NL}} \equiv P_{\mathrm{rec}} - \mathcal{L} \cdot P_{\mathrm{FID}}, \tag{3.103}$$

where a scaling factor $\mathcal{L}$ is added to account for the unknown coefficients involved in the P_{FID} term. As P_{FID} is second-order in power, the units of $\mathcal{L}$ are inverse power. This forms the basis for the nonlinear recovery algorithm, in which the $\exp(-\Gamma(t-t_H))$ term is sought to be isolated, as the second-order exponential term can be corrected for by this method. Using the current example, for $t > t_H$,

$$P_{\mathrm{NL}}(t) \simeq \underbrace{e^{-\Gamma(t-t_H)}}_{\text{Spectral hole}} + \underbrace{e^{-2\Gamma(t-t_H)} - \mathcal{L}(e^{-2\Gamma(t-t_H)}}_{\text{Nonlinear removal}} + \underbrace{\mathcal{O}[e^{-3\Gamma(t-t_H)}}_{\text{Higher-order terms}}]) \tag{3.104}$$

From this, the value of the $\mathcal{L}$-factor is extremely important, since it accounts for proper scaling of P_{FID}. Labeled as "nonlinear removal," it adjusts the scaling of the second-order term in P_{FID}, so that it would match the second-order term in P_{rec}. It is sensitive to the system being used, as will be demonstrated in the coming chapters. When adjusted properly, this algorithm will remove the nonlinearity caused by second-order term.

ANALYSIS

With the model set up, the results from the previous chapter can now be analyzed. Simulated spectral hole burning effects are analyzed, followed by the effects of reading them out. The nonlinear recovery algorithm is tested, and its performance is characterized. This includes the method for determining the $\mathcal{L}$ scaling factor.

Hole Burning Effects on Absorption

The effect on the absorption spectrum for burning spectral holes that are either increasingly deep or increasingly wide, and burning holes with varying $\alpha_0 L$ are analyzed, first. For burning deep holes, a point is reached when the medium can no longer burn any deeper. This effect is seen in Fig. 4.1, which shows how the absorption changes for varying hole depths β. For this, the burned hole width, Γ, was set to be 1 MHz, peak absorbance to be $\alpha_0 L = 2$, and varied the hole depth from 0.1 to 1 in steps of 0.1. Physically, this can be modeled by

$$\text{Absorption} = 1 - e^{-\alpha_0 L(1-\ell(\nu))}, \tag{4.1}$$

where

$$\ell(\nu) = \frac{\beta}{1 + \left(\frac{\nu-\nu_H}{\Gamma/2}\right)^2} \tag{4.2}$$

for a given hole location ν_H. The absorption is normalized to $\exp(-\alpha_0 L)$. That is, $0 \leq \beta \leq 1$. In the figure, the hole eventually reaches zero, meaning total saturation. It is unphysical for β to be greater than one.

While it's unphysical to burn more than the absorption peak $\exp(-\alpha_0 L)$, the

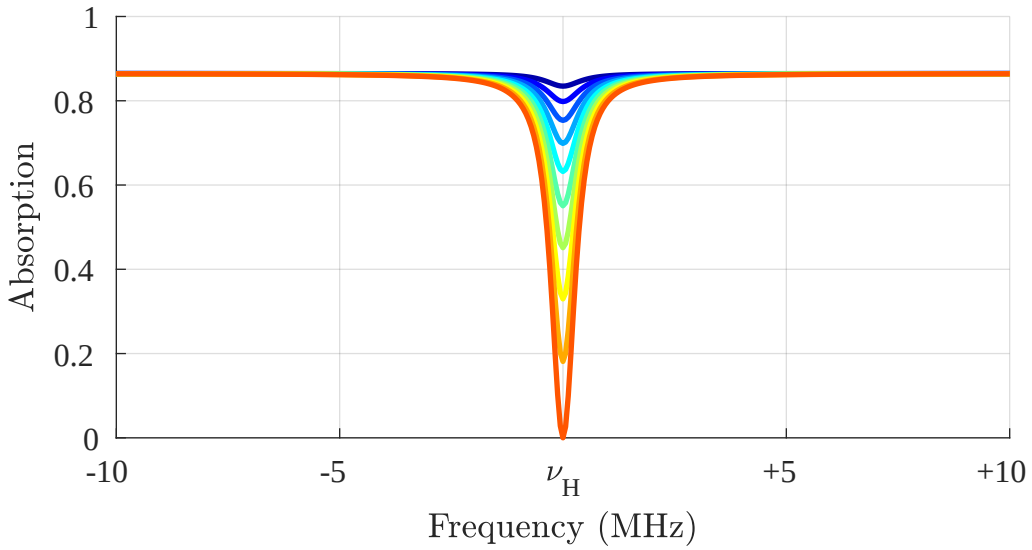

Figure 4.1: The effect on absorption of burned spectral holes with different hole depth values, with β changing from 0.1 to 1 in steps of 0.1, $\Gamma = 1$ MHz, and $\alpha_0 L = 2$.

absorption peak, itself, can become a parameter. If the maximum absorption is varied starting from $\alpha_0 L = 1$ to 5, the hole burns deeper into the material's spectrum. This is observed in Fig. 4.2. In this example, the hole depth was fixed at 0.6, and hole width kept at 1 MHz.

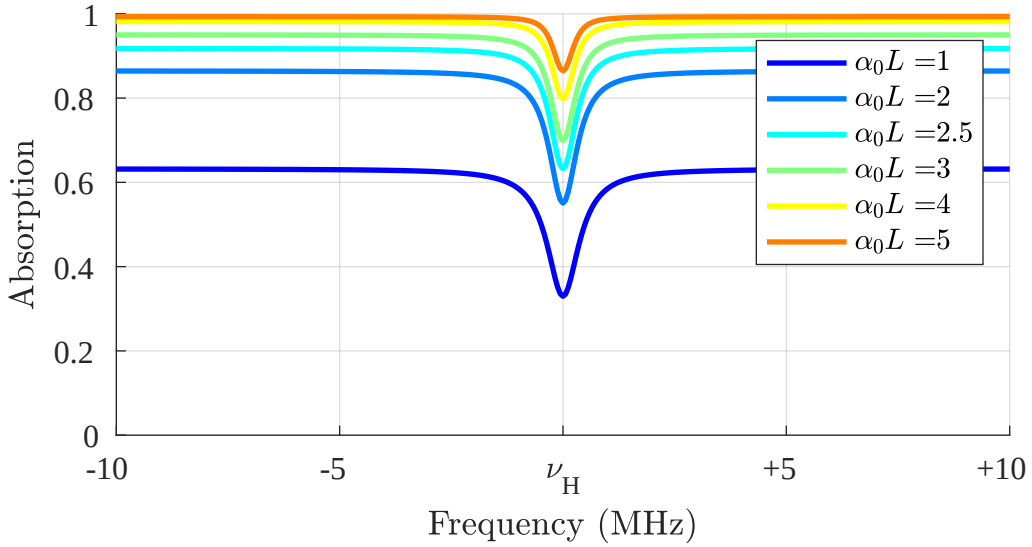

Figure 4.2: Saturation of the burned hole as result of increasing the absorption coefficient. The hole width and depth were fixed at 1 MHz and 0.6, respectively.

The last parameter to vary is the hole width. Up until now, it has been held fixed at 1 MHz. There is not much effected by the change in hole width, except the hole gets wider as is expected. The results are seen in Fig. 4.3. The hole depth was fixed to 0.6, $\alpha_0 L = 2$, and the hole width was varied from 0.1-3.0 MHz.

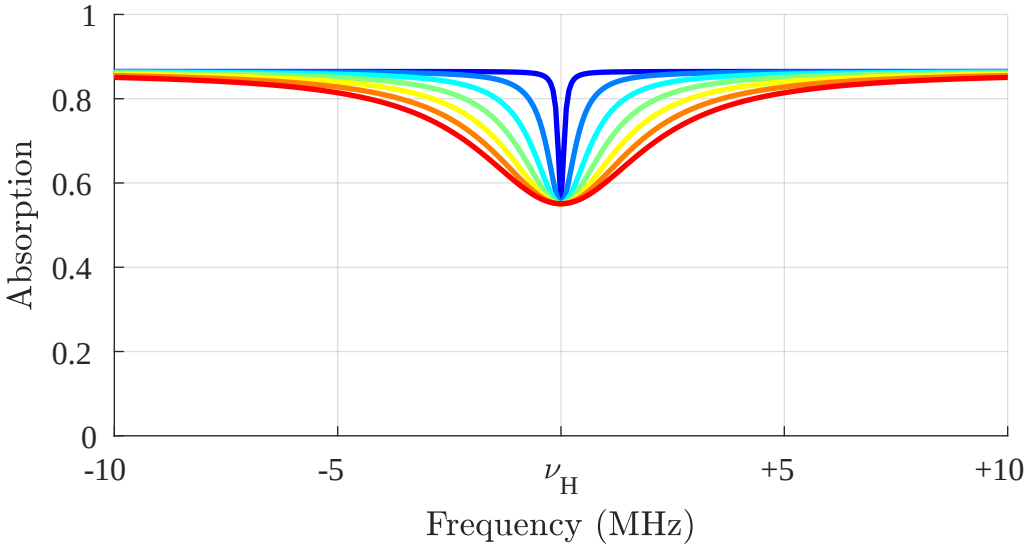

Figure 4.3: The effect on absorption of spectral holes with varying hole widths. The varying widths are $\Gamma = 0.1, 0.5, 1.0, 1.5, 2.0, 2.5, 3.0$ MHz, with $\beta = 0.6$ and $\alpha_0 L = 2$.

Linear Recovery

Readout of Single Spectral Hole

Now, the focus is brought to modeling a nonlinear system such that the new nonlinear algorithm is necessary to correct for the nonlinearity. Such a model has already been shown in the figures from Ch. 1. Attention is returned to those examples, where they can be discussed in detail.

In the example from Ch. 1, the hole depth was set to $\beta = 0.3$, $\alpha_0 L = 4$, and $\Gamma = 1$ MHz. Here, those same parameters are kept for this analysis, unless otherwise stated. However, other parameters from the original example in Ch. 1 will change, so that they are more closely in line with what was used for the actual experiment. This

would ensure a more accurate simulation to what was captured in the lab. The chirp rate becomes $\kappa = 12$ MHz/μs. The chirp duration is also defined to be $t_{\max} = 800$ μs. This is about 5 times less than what was used in the introductory examples. It only effects the total bandwidth one would see, which, for a simulation, may be arbitrary to begin with. The only other main difference is that artificial noise is now factored in. This is done by adding in an array of random values into the program's detected power (the ringout), at value that would be similar to what is seen in lab conditions–approximately -35 to -40 dB. The simulated detector bandwidth is 84 MHz. Finally, a logarithmic scaling is kept, unless it is relevant to show results on a linear scaling.

Now, recall from Ch. 1 that some of the peak signal strength is lowered, as a result from the nonlinearity. A way is needed that will allow a true comparison of the recovered signals to the original hole. One way that this could be accomplished is to simply find the difference in peak height by dividing the max of the spectral hole by the max of each of the recovered signals. However, a different method is used. Namely the area beneath curves are integrated, and then take their ratio to be the multiplicative normalization factor. Mathematically,

$$\text{Norm. Factor} = \frac{\int_{-\text{BW}}^{+\text{BW}} \alpha_H(\nu)\mathrm{d}\nu}{\int_{-\text{BW}}^{+\text{BW}} \alpha_R(\nu)\mathrm{d}\nu}, \tag{4.3}$$

where α_H is the spectral hole, and α_R is the recovered spectral hole. BW would be the bandwidth of interest, and it was chosen to be far enough away so that there would be no appreciable area underneath the curve of α_H. Then, the areas underneath this bandwidth region will be the same, after this process is completed. With this normalization factor, the spectral hole is plotted in Fig. 4.4.

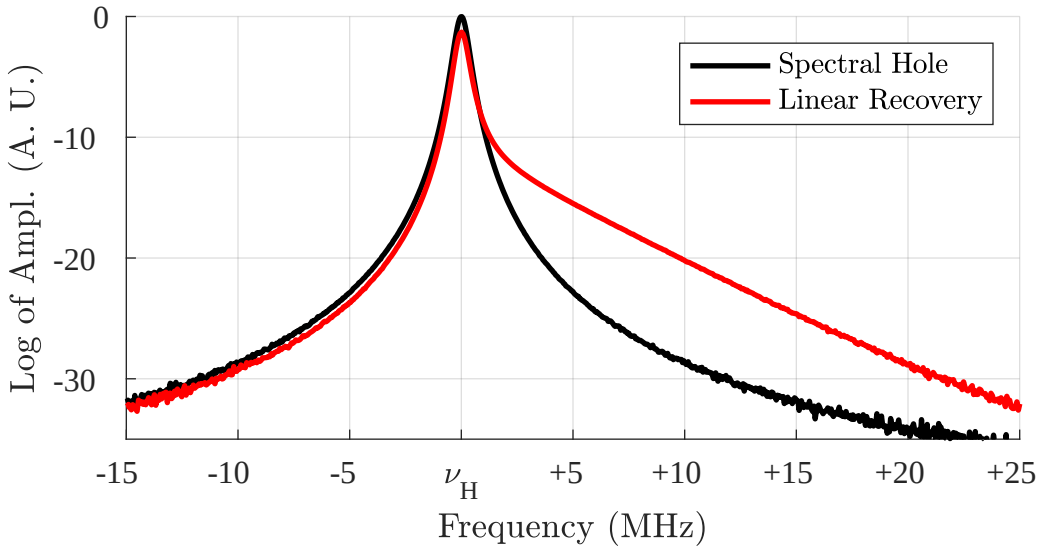

Figure 4.4: Linear spectral recovery of a 1 MHz wide signal, with $\beta = 0.3$, $\alpha_0 L = 4$, and $\kappa = 12$ MHz/μs.

Readout of Multiple Holes

Another important issue the nonlinearity can cause is to obscure a small signal next a large one. When a small signal is within the tail of the larger one, it can become masked in the tail or assigned a higher signal strength than it really has. To see this effect, a signal that is 100 kHz wide, with a hole depth that is 1% of $\alpha_0 L$, is added, and it is placed 5 MHz away from the original spectral hole, as seen in Fig. 4.5. The nonlinear tail adversely effects the signal, as it is masked making it more difficult to observe and accurately measure.

Nonlinear Recovery

Now, how the nonlinear recovery restores the spectrum is examined. Before applying it to the previous example, just what exactly the $P_{\text{det}}^2 + \mathcal{H}[P_{\text{det}}]^2$ and P_{FID} terms are doing to this hole needs to be scrutinized. These terms are plotted along with the linearly recovered hole in Fig. 4.6. The characteristic free-induction decay curves are seen in the $P_{\text{det}}^2 + \mathcal{H}[P_{\text{det}}]^2$ and P_{FID}. Now, the P_{FID} is what gets subtracted from the linearly recovered signal, up to the scaling factor $\mathcal{L}$. The P_{FID} needs to

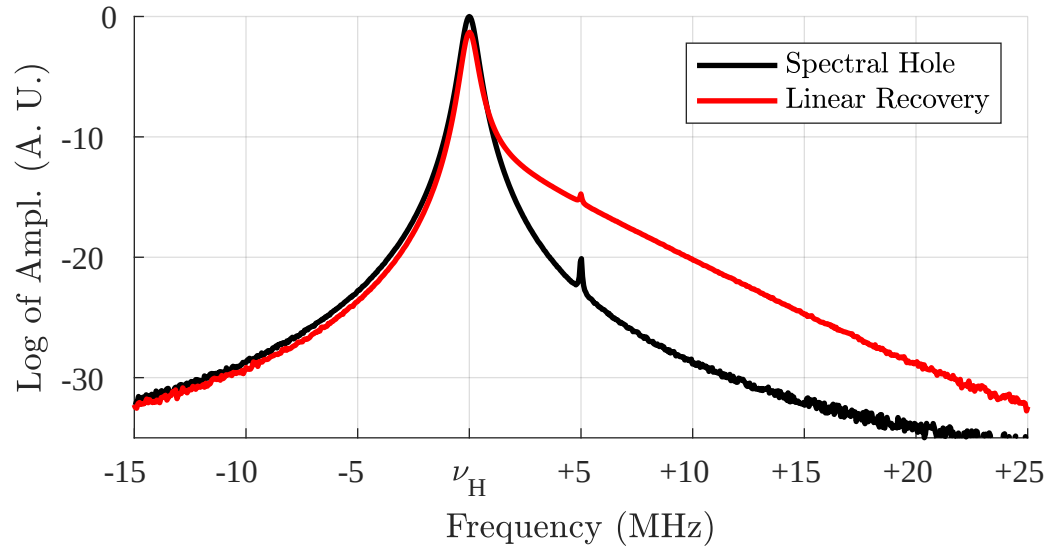

Figure 4.5: Linear spectral recovery of a 1 MHz main signal, with a 100 kHz signal located in the nonlinear tail at 5 MHz. The side signal is 1% as strong as the main signal.

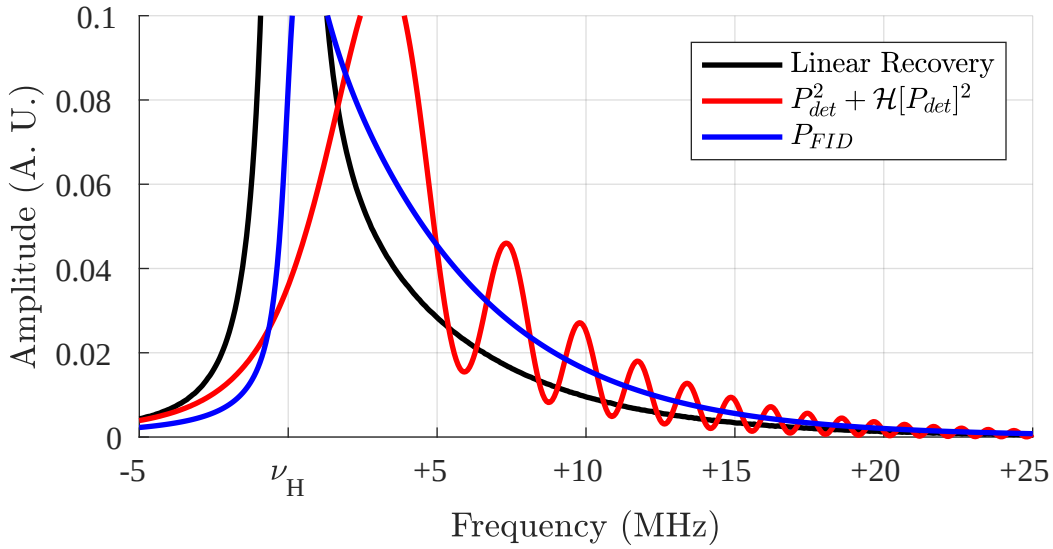

Figure 4.6: $P_{\rm det}^2 + \mathcal{H}[P_{\rm det}]^2$ and $P_{\rm FID}$ for a 1 MHz spectral hole, with $\beta = 0.3$, $\alpha_0 L = 4$, and $\kappa = 12$ MHz/μs.

essentially hug up against the tail of the linear recovery, without actually touching it. This is where proper scaling is required. For example, for a scaling factor $\mathcal{L} = 0.45$, then, the nonlinear recovery appears as it is in Fig. 4.6. With this $\mathcal{L}$-value, the

nonlinear recovery doesn't fully recover the signal shape. The question, then, arises as to how one can obtain the proper scaling coefficient.

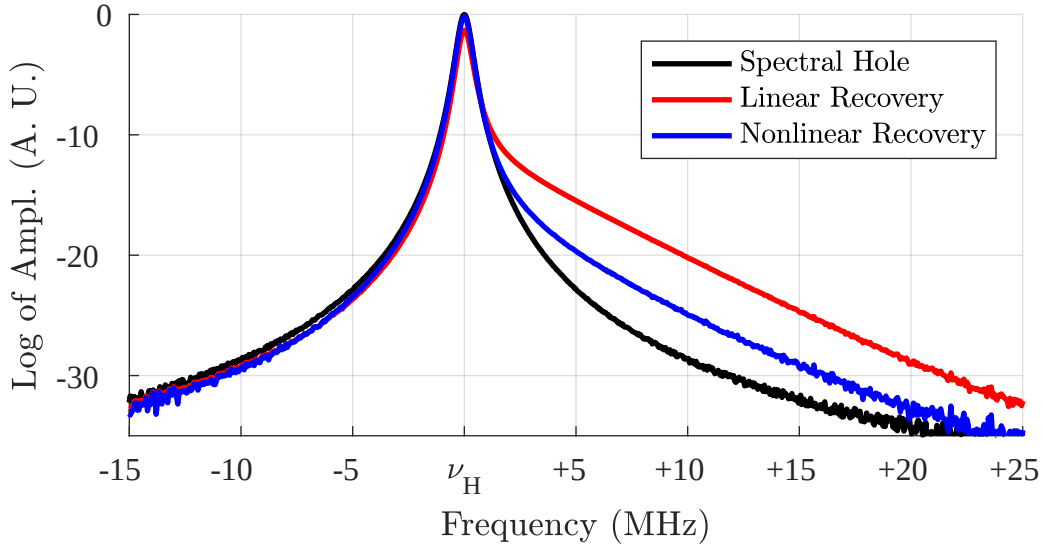

Figure 4.7: Nonlinear and linear spectral recovery of a 1 MHz wide signal, with $\beta = 0.3$, $\alpha_0 L = 4$, $\kappa = 12$ MHz/μs, and $\mathcal{L} = 0.45$.

To obtain the proper scaling factor, for a given Lorentzian hole, the power of statistics is employed, but, first, notice that the left-hand side (LHS) of the nonlinearly recovered spectral hole in Fig. 4.7 follows the actual spectral hole fairly well. Because of this, the LHS of the nonlinearly recovered hole can be considered to be an accurate representation of the actual LHS of the signal. This can, therefore, be compared to the right-hand side (RHS) of the same hole. The comparison between these are found in Fig. 4.8. The reason why the nonlinearly recovered LHS needs to be compared to the RHS, as oppose to the simulated spectral hole, is that the spectral hole is a simulation. In real life, the actual hole shape is unknown.

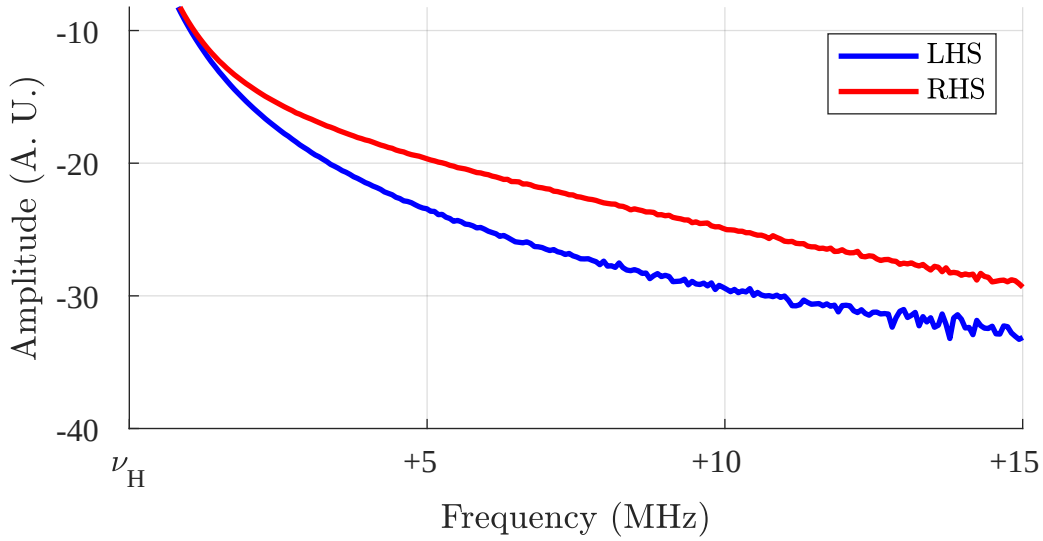

Figure 4.8: Comparison of the LHS and RHS of the same nonlinearly recovered spectral hole, with $\beta = 0.3$, $\alpha_0 L = 4$, $\kappa = 12$ MHz/μs, and $F = 0.45$.

Nonlinear Scaling $\mathcal{L}$-Factor

The scaling factor by which P_{FID} must be changed is going to be dependent on several factors. In the lab, it was found to depend on the absorption $\alpha_0 L$ and the scanning chirp laser power P_{chirp}. These details are covered in Ch. 6. In this subsection, how it changes with $\alpha_0 L$ is covered. To determine what factor is best, in both the simulation and real data, the root-mean-square error (RMSE) is used, which is a measure of the differences between the values of a sample predicted by a model and the values actually observed. RMSE represents the sample standard deviation, which is a measure of how disperse the data are from the sample mean. The RMSE is given by [39]

$$s = \sqrt{\frac{1}{N-1}\sum_{i=1}^{N}(x_i - \overline{x})^2}, \tag{4.4}$$

where N is the number of data points, x_i is the ith data point, and $\overline{x}$ is the accepted mean for that point. If the LHS of a nonlinearly recovered signal is considered to be

the accepted or predicted value, the RMSE can be used to compare it with its RHS.

The plan is to now vary $\mathcal{L}$-values in (3.103). Then, the RMSE is used to find the $\mathcal{L}$-value that corresponds to the the minimum RMSE. This will be the best scaling factor value for the given parameters. Running through a simulation of 1,000 different $\mathcal{L}$-values ranging from 0 to 2, the optimal value is found to be $\mathcal{L} = 0.5495$. The RMSE vs. $\mathcal{L}$-values are plotted in Fig. 4.9.

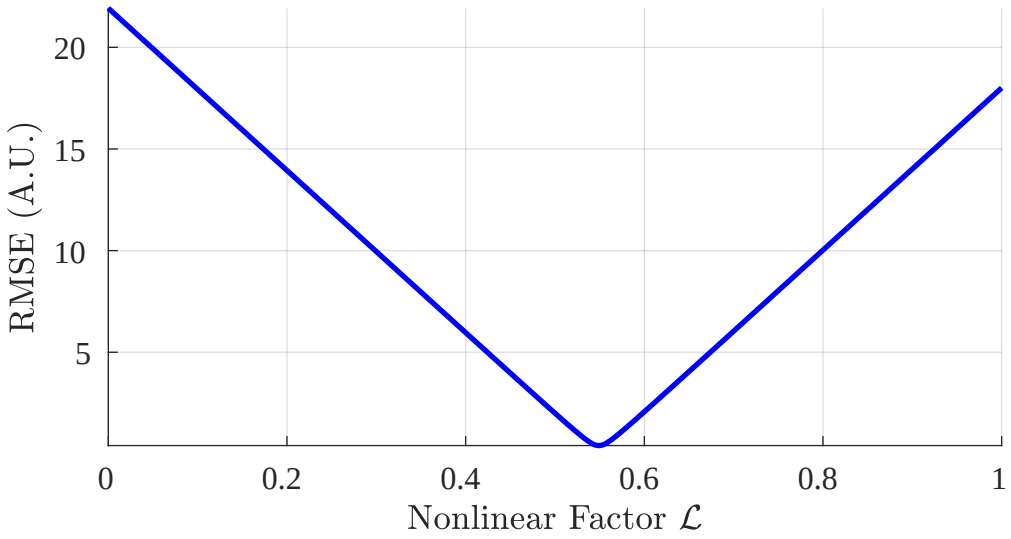

Figure 4.9: Variation of the RMSE for different $\mathcal{L}$-values, corresponding to the example from Fig. 4.7. The minimum corresponds to the best value of $\mathcal{L}$, with $\beta = 0.3$, $\alpha_0 L = 4$, $\kappa = 12$ MHz/μs.

When this value of $\mathcal{L}$ is used, the nonlinear recovery now accurately restores the spectrum, as seen in Fig. 4.10. Additionally, the relative amplitude difference, which was first demonstrated in Fig. 1.3, is shown in Fig. 4.11. The linear recovery curve behaves as it did in Ch. 1, but now the nonlinear recovery curve shows that, indeed, there exists little difference between the spectral hole and the nonlinearly recovered hole.

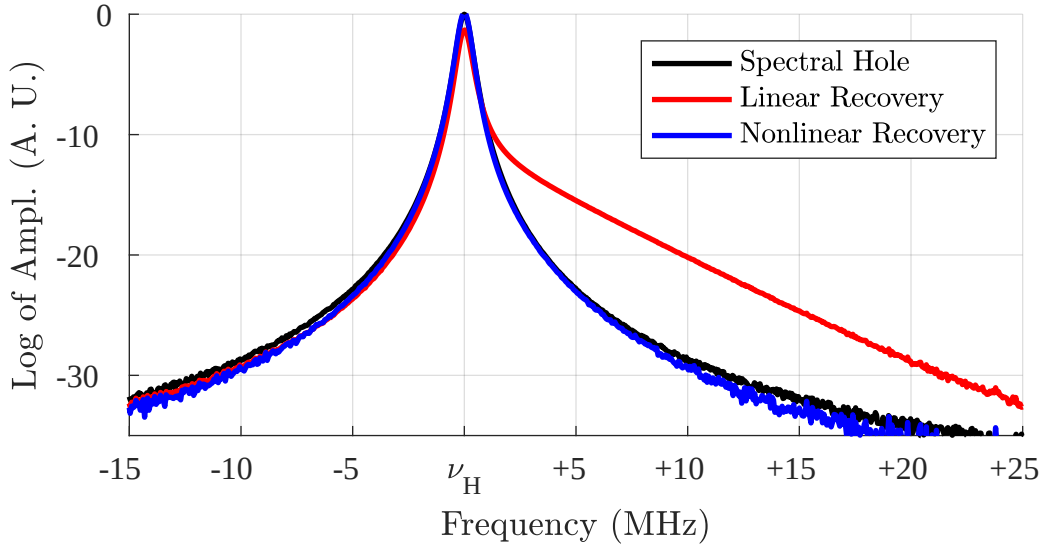

Figure 4.10: Nonlinear and linear spectral recovery of a 1 MHz wide signal, with $\beta = 0.3$, $\alpha_0 L = 4$, $\kappa = 12$ MHz/μs, and $\mathcal{L} = 0.5495$.

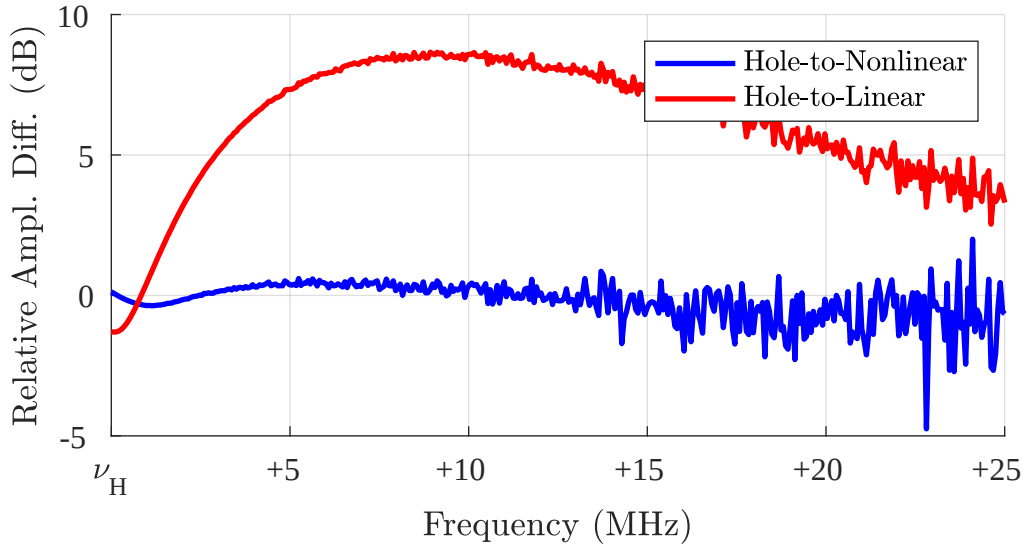

Figure 4.11: Relative amplitude differences for the linear recovery-to-spectral hole and the nonlinear recovery-to-spectral hole for $\mathcal{L} = 0.5495$.

Change in $\mathcal{L}$ Due to Absorption $\alpha_0 L$

The main characterization of the $\mathcal{L}$-factor is done in Ch. 6. There is one characterization that cannot be made there. Namely, how the change in peak absorption changes the $\mathcal{L}$-value. In the lab, only two different crystal lengths were used, which would only provide two data points. Therefore, the change in $\mathcal{L}$ against the change in $\alpha_0 L$ is observed in Fig. 4.12. It was found to fit an exponential best, given as

$$\mathcal{L}(\alpha_0 L) = a \exp(b \cdot \alpha_0 L) + c, \tag{4.5}$$

with $a = 0.2427$, $b = 0.2868$, $c = -0.2266$. Interestingly, $a \approx b \approx -c \approx 1/4$. So, a generalization could be made here that

$$\mathcal{L}(\alpha_0 L) \approx \frac{1}{4}\left(e^{\alpha_0 L/4} - 1\right). \tag{4.6}$$

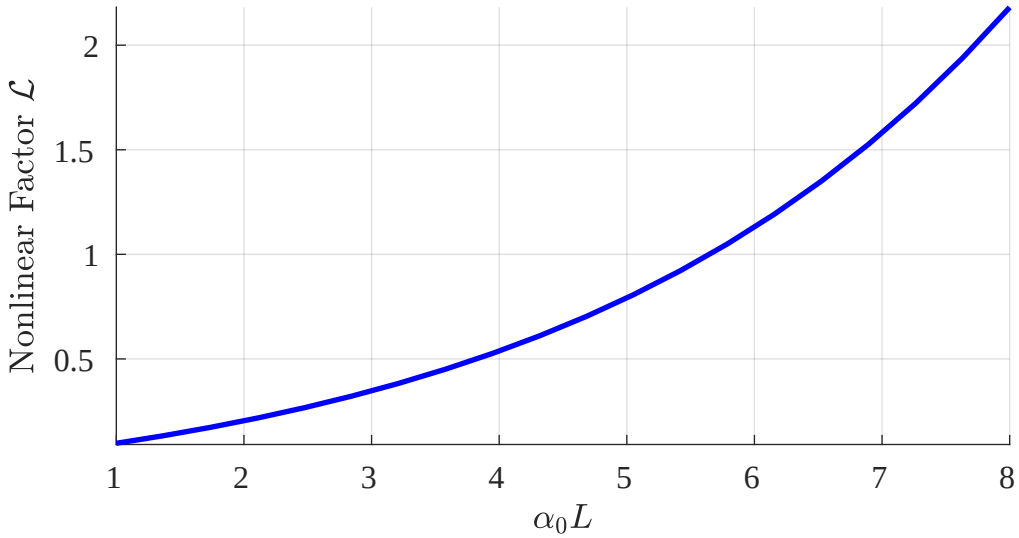

Figure 4.12: The effect on the nonlinear factor as a result of a changing absorption, with $\beta = 0.3$, $\Gamma = 1$ MHz, and $\kappa = 12$ MHz/μs.

Multiple Holes

Finally, the nonlinear recovery algorithm is applied to the burned spectrum from the example in Fig. 4.5. It is observed to accurately recover the entire spectrum, with proper signal strength. This is shown in Fig. 4.13.

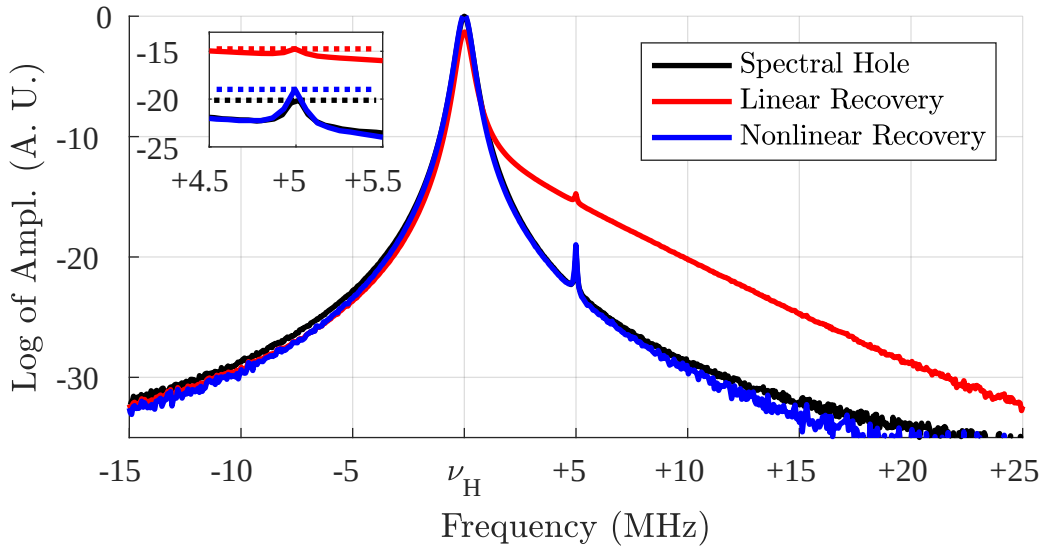

Figure 4.13: Nonlinear and linear spectral recovery of a 1 MHz main signal, with a 100 kHz signal located in the nonlinear tail at 5 MHz. The side signal is 1% of the main hole depth $\beta = 0.3$, with $\alpha_0 L = 4$, $\kappa = 12$ MHz/μs, and $\mathcal{L} = 0.5495$. (Inset) The peak heights of each figure are indicated. The spectral hole peak is -20.1, linear recovery is -14.7, and nonlinear recovery is -19.0.

Since the signal strength of small side signals are now expected to be restored to their proper peak height, it is useful to see what kind of sensitivity can be expected from signals that may be in the nonlinear tail. For a side signal 5 MHz from the main hole, with $\beta = 0.3$, with $\alpha_0 L = 4$, $\kappa = 12$ MHz/μs, and $\mathcal{L} = 0.5495$, the peak amplitude difference of the side signal between the linear and nonlinear recovery was found to be as larger than 6 dB, when the side signal is very small. Fig. 4.14 plots the peak heights of this side signal for varying side hole depths, ranging from just under -30 to just under -14 dB down from the main signal. For reference, the amplitude

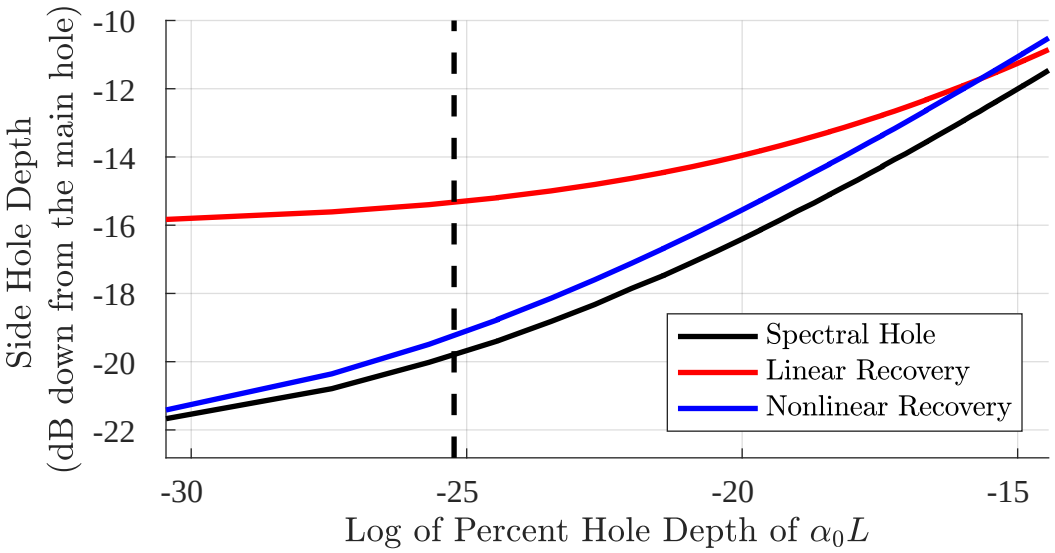

Figure 4.14: Difference in peak amplitudes for linear and nonlinear recoveries of a small signal at 5 MHz away from the central spectral hole, with $\alpha_0 L = 4$, $\kappa = 12$ MHz/μs, and $\mathcal{L} = 0.5495$. The dashed line indicates the size of the side hole from Fig. 4.13.

value at this frequency location, in the absence of any side hole, should be around -22.5 dB.

LABORATORY METHODS

System Layout and Schematic

In this section, the system layout and schematic that was used to record data is presented. This system was developed at Montana State University's Spectrum Lab over the past 10 years. To be completely clear, I did not build nor create any of laboratory systems described in this section. Over the course of my time at Spectrum Lab, I was trained to operate the system presented here, and take data that is presented both in this chapter and in Ch. 6.

The General Overview

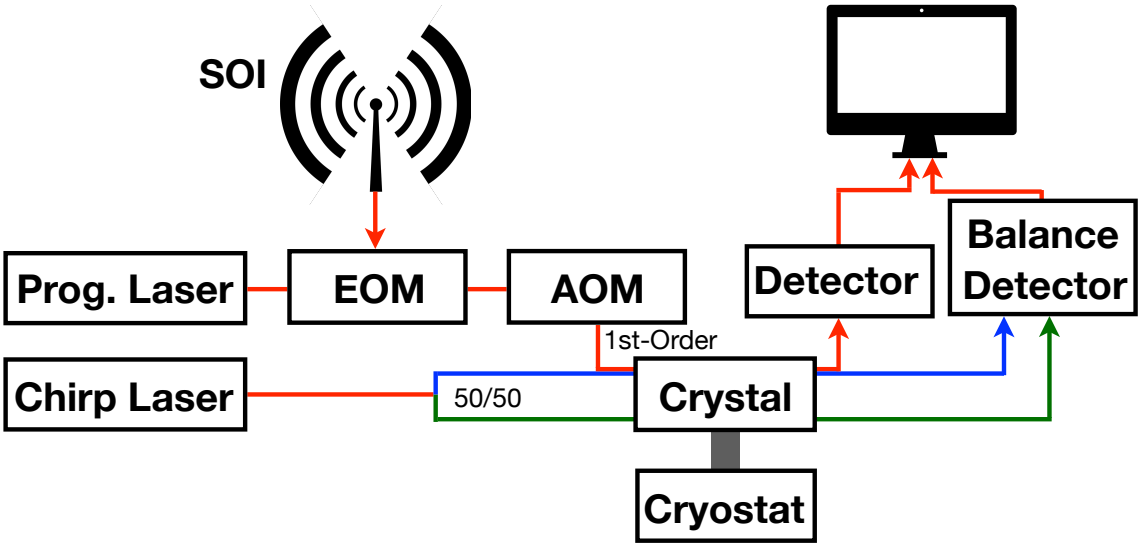

Figure 5.1: A general overview of the system.

The primary function of the experiment is to act as a high-resolution spectrum analyzer for an arbitrary spectrum or signal of interest (SOI). For that reason, this overview starts with the signal and follows its path through to the end detector. The general view is drawn in Fig. 5.1. Similar setups have been used in the past [19]. It

all begins with an antenna that couples the SOI into the system and to an electro-optic modulator (EOM), where it acts as an applied voltage driving the EOM. Next, a high-powered laser beam is sent through the EOM. This causes the output to be phase modulated so that the resultant beam has an attenuated carrier frequency with sidebands caused by the SOI. Thus, the SOI is effectively up-converted onto a carrier wave. From there, the beam is pulsed using an AOM, where the first-order is used. The next major component in the system is the crystal, cooled to around 3 K with a close cycle cryo-cooler from Montana Instruments (i.e. cryo-station). This beam is then sent to a 40 kHz detector. Since this beam burns the holes into the crystal's spectrum, it is called the programming beam, in the sense that it "programs" the spectrum in.

To actually see the spectrum on a detector, a low-powered, chirped laser beam that sweeps across the spectrum of the crystal linearly in time is used. This is the beam that was analyzed in Ch. 3. Sending it through the material, it must cross paths with the programming beam. This allows one to map out the absorption spectrum of the crystal. Since the holes exist in the spectral domain of the material, it will now see those holes in time as it chirps across in frequency. After exiting the crystal, this beam is sent to a detector for analysis. This is said to be "reading" the spectrum, and so it is called the readout beam. A third beam that is identical to the readout beam is, also, sent into the material. This is done by using a 50/50 fiber splitter on the chirp. It does not cross paths with either of the two previous beams and serves as a reference for the readout beam. It will record the unaltered material spectrum, and then be sent to a detector. It has its utility in background subtraction. This is done by subtracting what the readout beam records from what the reference beam records. The spectrum common to both is the unaltered material spectrum. Thus, after the subtraction has occurred, only the absorption spectrum from the SOI remains. This

process is known as balanced detection.

The final step is compiling and processing all the data from the detectors. This part is in post analysis, and is covered in Chapter 6.

The Programming Laser

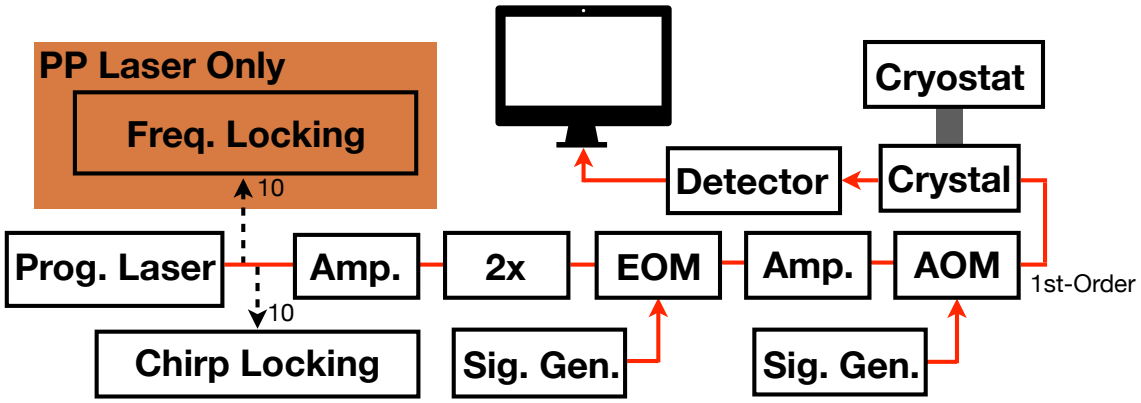

Figure 5.2: Detailed path of the programming laser.

The system begins with two narrow linewidth lasers at around 1.5 μm. One is for the programming beam and the other is for the chirp, which feeds to the readout and reference beams. These lasers are tunable to different frequencies. The programming laser is tuned so that its frequency corresponds to the frequency of maximum absorption in the crystal. For Tm^{3+}: YAG, the maximum absorption wavelength is $\lambda = 793.374$ nm (in air), which corresponds to a frequency of $\nu = 377.8702$ THz. This laser will undergo frequency doubling in the optical circuit, so it is tuned to be half that value $\nu_{\text{prog}} = 188.9351$ THz. Two different programming lasers were used throughout the course of this research. The first was a Pure Photonics (PP) laser, and the second was a NKT Photonics (NKTP) laser. The PP laser was not as stable (with respect to itself), and required frequency stabilization. The NKTP laser did not need this. Frequency stabilization was done first, if it was necessary. Afterwards, the path was the same.

A detailed diagram of the programming path is seen in Fig. 5.2. After setting the frequency, the programming beam starts its journey by first locking to itself via fiber heterodyne, if necessary. This showed improved performance of the laser stability, when the error signal was viewed on an oscilloscope, although this was not measured. Then, it is sent through to a fiber amplifier, before getting frequency doubled. This is done using second-harmonic generation (SHG) in a periodically poled KTP crystal [40]. Then the beam goes through to the EOM, where it becomes modulated with the SOI. Going into a little of the mathematics can be insightful for analysis later. Assume that the modulated programming beam is of the form

$$E(t) = A(t)e^{i4\pi\nu_{\text{prog}}t}, \tag{5.1}$$

where

$$A(t) = e^{i\phi(t)} \tag{5.2}$$

is the modulation due to the SOI. In this expression, $\phi(t)$ is the input signal, but could be any arbitrary spectrum. An RF signal generator was used in this setup. If the RF signal is modeled as a summation of cosines

$$\phi(t) = \sum_{m=0}^{N} \beta_m \cos(2\pi\nu_m t), \tag{5.3}$$

where β_m is the m^{th} amplitude, corresponding to a frequency of ν_m, then (5.2) may be expanded into a basis of Bessel functions using the Jacobi-Anger identity [41, 42].

Examining, first, the $m = 0$ case, the identity states that

$$e^{i\beta_0 \cos(2\pi\nu_0 t)} = \sum_{n=-\infty}^{\infty} J_n(\beta_0) i^n e^{in2\pi\nu_0 t}, \tag{5.4}$$

where J_n is the n^{th} order Bessel function of the first-kind. For the special case of a single tone ($N = 0$), the signal can be written as

$$E(t) = \sum_{n=-\infty}^{\infty} J_n(\beta) i^n e^{i2\pi(2\nu_{\text{prog}} + n\nu)t}. \tag{5.5}$$

(5.5) is insightful, as this type of behavior is covered in this thesis. It is important to note that for a given power and frequency, the output orders will be separated by integer multiples of the frequency of the tone ν. Also, with each additional order, the output orders will shrink in accordance with the Bessel functions. Thus, if the frequency is held constant and the amplitude power of the signal is varied, it should be possible to map out the Bessel functions of each n. This is a metric by which the dynamic range of the system is determined. This measurement is performed, with the results presented in the proceeding chapter.

After the modulation, the signal is sent to a tapered semiconductor optical amplifier (SOA). This can amplify the beam as much as 10-20 dB.

Once through the amplifier, the beam is sent through to an acousto-optic modulator (AOM). The modulator grants the ability to pulse the otherwise always-on beam. A RF pulse to the AOM is supplied, which operates the piezo-electric transducer inside the AOM. The transducer creates sound waves in the AOM, which creates a diffraction grating. Then, the first-order diffracted beam is picked out from the AOM. The first-order is selected, because the zeroth order will always be 'on' in the sense that it is always permitted to pass through the AOM as DC signal.

Although, the intensity in the zeroth order is attenuated to some degree, as the intensity is spread out among the diffraction orders. The first-order will only pass through when the Bragg condition is met, given as

$$\sin\theta_B = \frac{\lambda}{2\Lambda}, \tag{5.6}$$

where θ_B is the Bragg angle, λ is the wavelength of the beam, and Λ is the wavelength of the acoustic wave inside the AOM [36]. Thus, this permits control over when the beam can pass through the AOM. If there is no applied RF voltage, then there is no diffraction and no part of the beam is permitted to pass. If a pulsed RF is applied to the AOM, then the beam that passes through will take on the same temporal pattern as the pulse. Additionally, the optical power passing through the first-order diffraction out of the AOM is maximized by tilting or rotating the AOM, with respect to the incoming beam. Afterwards, it gets sent through to the crystal, where part of it gets absorbed. The part of the beam that does not get absorbed is then sent to a detector.

Chirp Laser

Now, the chirp laser path is described. Its frequency is tuned so that it is about 15.6 GHz away from the programming beam, or $\nu_{\text{chirp}} = 188.9474$ THz. The reason for this will become apparent. The first thing done with this laser is to offset lock it to the programming laser frequency. Use Fig. 5.3 for reference. Then, it gets modulated with a frequency chirp, using an electro-optic modulator. The chirp is generated by an RF board. On the RF board, a direct digital synthesizer (DDS) is used to create a frequency chirp. Then, through filtering, amplification, and frequency multiplication the chirp center frequency, ν_s, and chirp rate, κ_{DDS}, are multiplied six times. To be clear, κ_{DDS} and ν_s are set by the DDS board. This output, then, drives the chirp

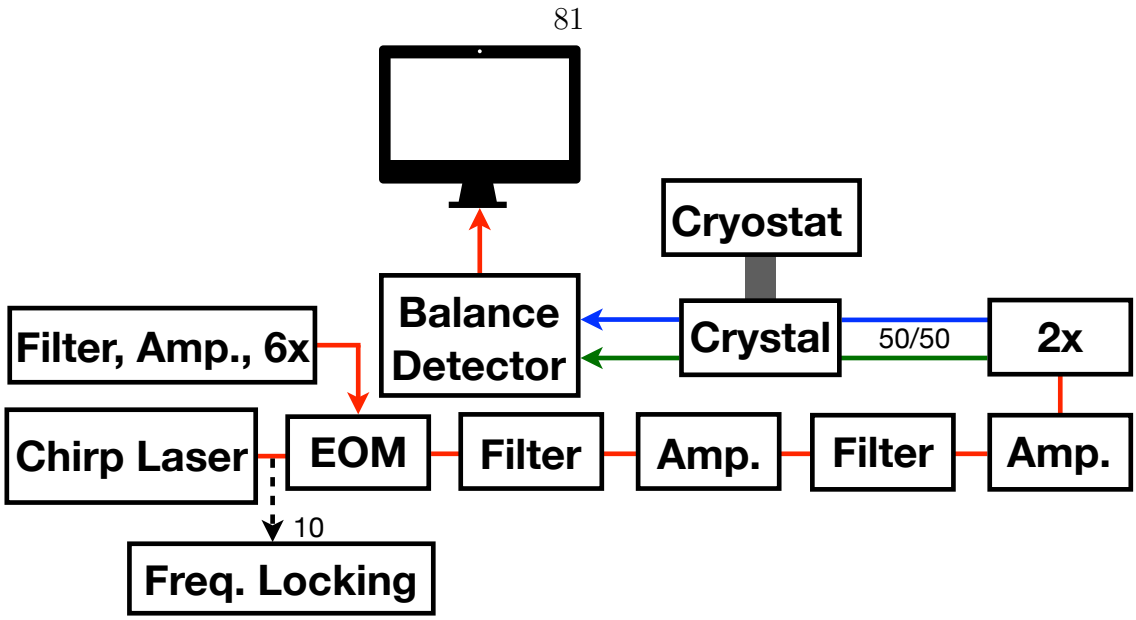

Figure 5.3: Detailed path of the chirp laser.

EOM.

Essentially, this EOM works like any other EOM by combining the carrier signal with the modulation signal. However, the modulation signal is unique. The phase function $\phi(t)$ is designed so that it is of the form

$$\phi(t) = \frac{V}{V_\pi}\pi \cos\left(6(2\pi\nu_s + \pi\kappa_{\text{DDS}}t^2)\right), \tag{5.7}$$

where V_π is the half-wave voltage. For convenience, set

$$\beta = \frac{V}{V_\pi}\pi, \tag{5.8}$$

so that

$$\phi(t) = \beta \cos\left(6(2\pi\nu_s t + \pi\kappa_{\text{DDS}}t^2)\right). \tag{5.9}$$

Now, thanks again to the Jacobi-Anger expansion, (5.9) may be expanded into a basis

of Bessel functions, given as

$$A(t) = \sum_{n=-\infty}^{\infty} J_n(\beta) i^n e^{in[6(2\pi\nu_s + \pi\kappa_{\mathrm{DDS}} t^2)]}. \tag{5.10}$$

The chirp bandwidth may be ignored in the summation for this analysis, since the chirp rate is considered slow compared to ν_s. Given that the input optical field to the EOM is

$$E(t) = e^{i2\pi\nu_{\mathrm{chirp}} t}, \tag{5.11}$$

the output is

$$E(t) = \sum_{n=-\infty}^{\infty} J_n(\beta) i^n e^{i2\pi(\nu_{\mathrm{chirp}} + 6n\nu_s)t}. \tag{5.12}$$

With this expression for the output of the chirp modulator, it can be thought of in terms of harmonic orders from the summation. By controlling the voltage V, and therefore the value of β, the voltage is tuned so that the second-order in (5.12) is maximized and all other orders are minimized. The second order is chosen for its bandwidth. As you look at higher and higher orders in the output, their bandwidth gets larger and larger. This comes at the cost of power, as the $\max(J_2) < \max(J_1)$. The second-order offers a mix of both. One last thing to note, here, is there is an optical frequency doubler after the filtering of the 2nd order. So, in the end,

$$E(t) = -J_2(\beta) e^{i2\pi(2\nu_{\mathrm{chirp}} - 24\nu_s)t}. \tag{5.13}$$

Now, it can be explained why the chirp frequency is set to be 15.6 GHz away from the programming laser frequency. The programming laser frequency is wholly

determined by the crystal and its absorption spectrum, as already discussed. Since the chirp is chosen to be focused on the second sideband, that sideband will be swept through starting at $24\nu_s - \mathrm{BW}/2$ up to $24\nu_s + \mathrm{BW}/2$. BW is the bandwidth of the second sideband, equal to $24\kappa_{\mathrm{DDS}}\tau_C$, where τ_C is the chirp duration. This sweep needs to encompass the spectrum from the programming beam to allow for the readout of the absorption spectrum. Therefore, it must be centered on or around ν_{prog}. Mathematically, this means that chirp carrier minus the chirp center frequency must be equal to the programming laser frequency. In other words,

$$2\nu_{\mathrm{chirp}} - 24\nu_s = 2\nu_{\mathrm{prog}}. \tag{5.14}$$

The chirp center frequency is determined by the inputs on the chirp. For this purpose, it is a known value set to be $\nu_s = 1,300$ MHz. From this, the chirp carrier frequency is solved for

$$\nu_{\mathrm{chirp}} = \nu_{\mathrm{prog}} + 12\nu_s = 188.9474 \text{ THz}. \tag{5.15}$$

As claimed, this value is 15.6 GHz away from the programming laser frequency, and it can be seen that $12\nu_s = 15.6$ GHz. Also, note that the chirp rate discussed elsewhere throughout this thesis is related to the one presented here by $\kappa = 24\kappa_{\mathrm{DDS}}$.

Next, the signal is optically filtered with two fiber grating Bragg bandpass filters. In fact, it goes through the first bandpass filter, then is amplified, and then goes through the second bandpass filter. The bandpass filters are used to filter out all the other orders. After the filters, the signal is further amplified by passing through an erbium-doped fiber amplifier (EDFA). To make the readout and the reference beams, the beam is split 50/50, before the crystal, with a fiber splitter. From there it is goes on to the crystal, followed by the balance detector.

Frequency Stabilization

Clearly, it is vital for the lasers to be stable with respect to one another and even to themselves. As the above analysis shows, their frequencies need to be precisely tuned. Laser drift is a phenomenon that is encountered in the lab, and it happens when a laser's carrier frequency unintentionally changes over time. This can occur in both long term (on the order of months) and short term (microseconds to seconds) time periods. It can be verified to occur by tapping the signal with an external wave meter, for example. Here, it is described how to overcome this problem for short term time periods, as well as lock the frequencies in place with respect to each other.

Over the course of this thesis work, two different laser setups were used. The first involved using two Pure Photonics lasers. These lasers tended to be less stable, although this was not quantified. Their laser locking method is described in Setup One. Later, one of the Pure Photonics lasers, associated with the programming beam, was changed out for a stable NKT Photonics laser. This is a similar setup to Setup One, but it no longer needs to lock to itself. This is described in Setup Two.

Setup One The first thing that is done is to lock the programming laser to a fringe of a fiber interferometer. Some of the light is split off with a fiber optic splitter, for reference refer to the schematic in Fig. 5.4. This path is then split 50/50 with half going through an AOM and half passing through to a 70 meter delay line. The AOM is driven at a frequency of 80 MHz. Then, the two beams are recombined and heterodyne detected. If there is no frequency fluctuations of the laser the heterodyne detected signal is an 80 MHz beat tone. However, if there are fluctuations in the laser frequency, then the beat tone will fluctuate accordingly. The beat tone is, then, compared to the 80 MHz driving the AOM using the mixer producing an error signal. The mixer is a digital phase and frequency detector, the output of which is

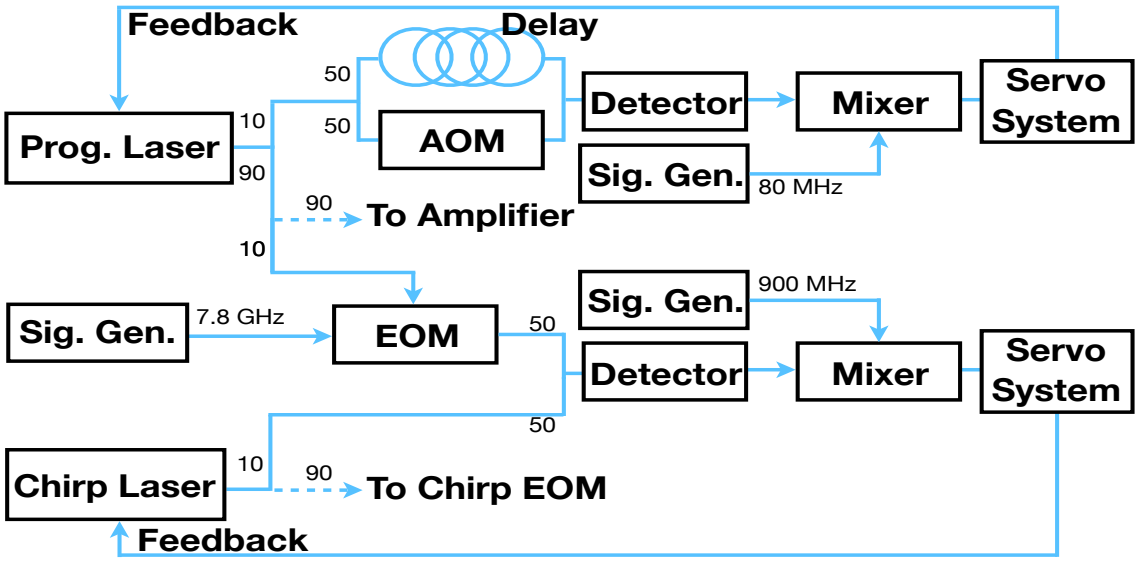

Figure 5.4: Diagram of laser locking for setup one, using a heterodyne on the programming path.

then fed into a servo board to be amplified and filtered. This drives feedback into the amplitude modulation (AM) port on the laser, which changes the laser current to tune the frequency. It corrects the frequency difference until there is zero phase difference between the beat tone and the 80 MHz tone on the servo board. This is how the programming laser frequency is stabilized to itself. There is about 100 kHz frequency bandwidth, using this system. That is, the phase fluctuations need to be less than 100 kHz to stabilize them out. If you were to observe this on a spectrum analyzer, you would see characteristic servo shape around the beat tone. This tells you the laser is locked. These are seen in Fig. 5.5.

The chirp laser is locked in a similar manner, but, instead of locking to itself, it gets locked to the programming laser. Therefore, it starts by picking off another small portion of the programming laser. This is sent through to an EOM that is being driven at $6\nu_s = 7.8$ GHz. This will place the sidebands on it in intervals of 7.8 GHz. ν_{chirp} needs to be centered on or near $\nu_{\text{prog}} + 12\nu_s$. The programming laser then comes together with the chirp laser, after the programming laser has passed

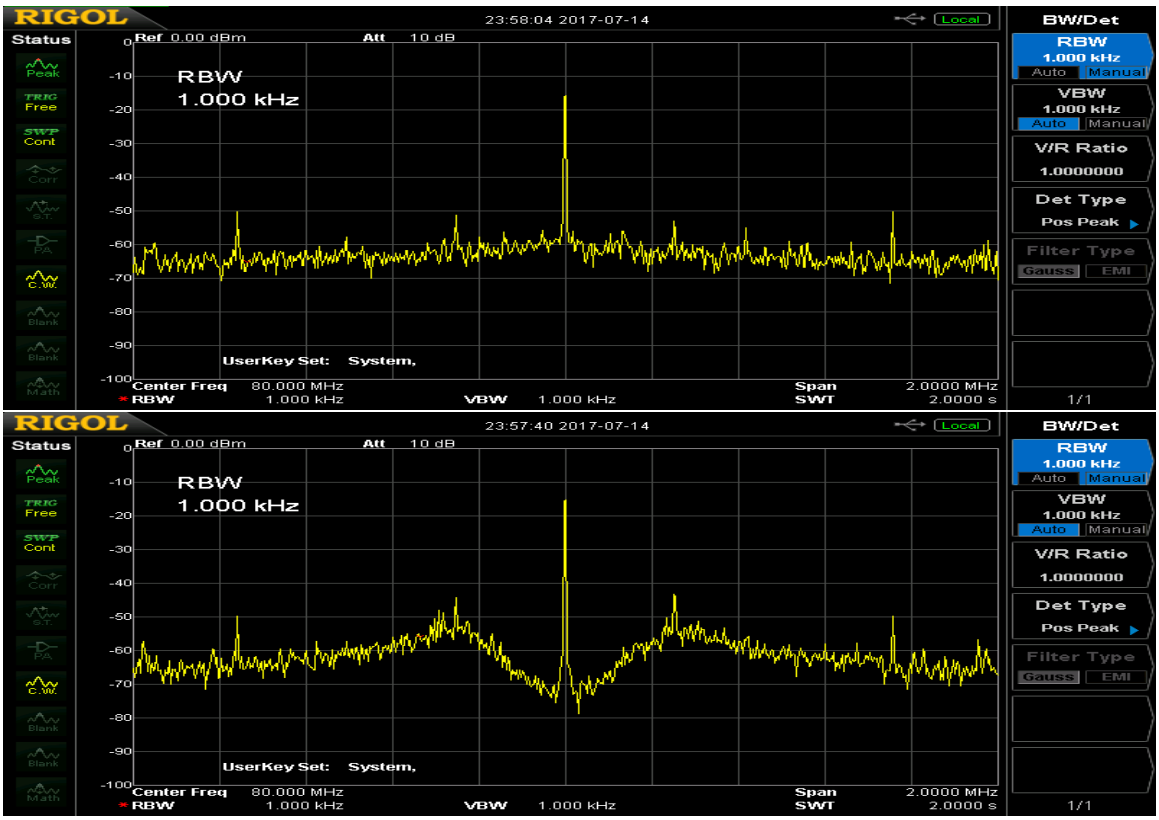

Figure 5.5: Top: Example of the programming laser not locked. Bottom: Example of the programming laser locked.

through this EOM. It is then essentially sent through a similar system as before, where the programming and chirp beams combine for heterodyne detection. Then, they mix with a 900 MHz signal. The beat tone between the two beams is found and checked on a servo board. The servo board then adjusts the chirp laser until the phase difference goes to zero, thus, locking the chirp laser to stay exactly where it needs to be, in relation to the programming laser.

Setup Two The NKT Photonics laser is a fiber laser, and is quite stable [43]. Therefore, any need to lock to the fiber interferometer is bypassed. The chirp laser is still locked exactly the same way as before, though, as seen in Fig. 5.6.

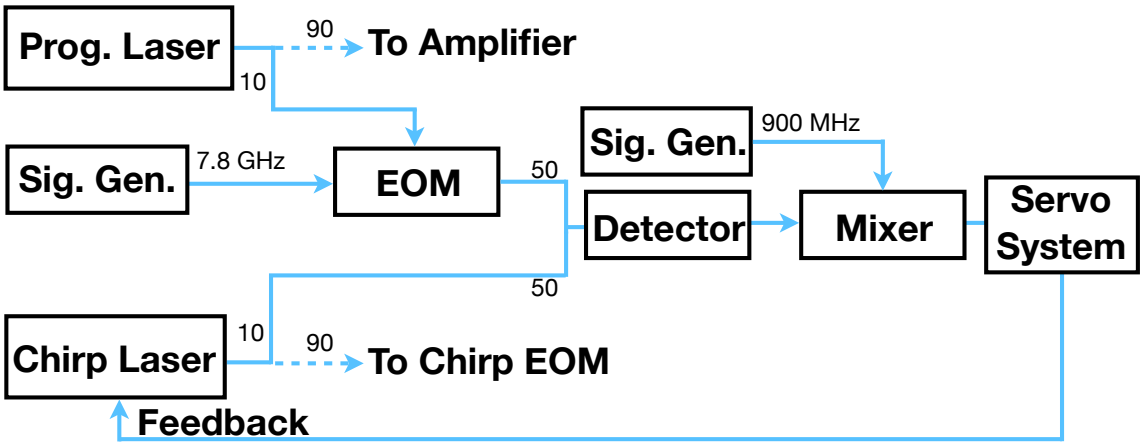

Figure 5.6: Diagram of laser locking for setup two, forgoing the locking method for the programming.

Inhomogeneous Absorption Spectra Measurements

To measure the inhomogeneous absorption spectrum in the lab, measurements of the optical nutation edge described in (2.16) were taken. This is done using the programming laser. An example of this measurement is given in Fig. 5.7. The maximum absorption point and 100% transmission powers are marked. Note that the data was captured in voltage, but that $|E|^2 \propto V$.

At the given scale, it is unclear how to determine where the input power begins. A zoomed-in portion of the turn-on is given at the bottom of the figure. With this zoomed-in portion, it is now clear where the signal turns on. Therefore, for the given maximum absorption and 100% transmission values determined, (2.13) can be used to calculate the absorption coefficient for that frequency. Tuning the frequency of the laser, then, the absorption spectrum of the crystals that were used can be mapped out. This is done by finding each 100% transmission and maximum absorption points for each tuned frequency, and then using (2.13).

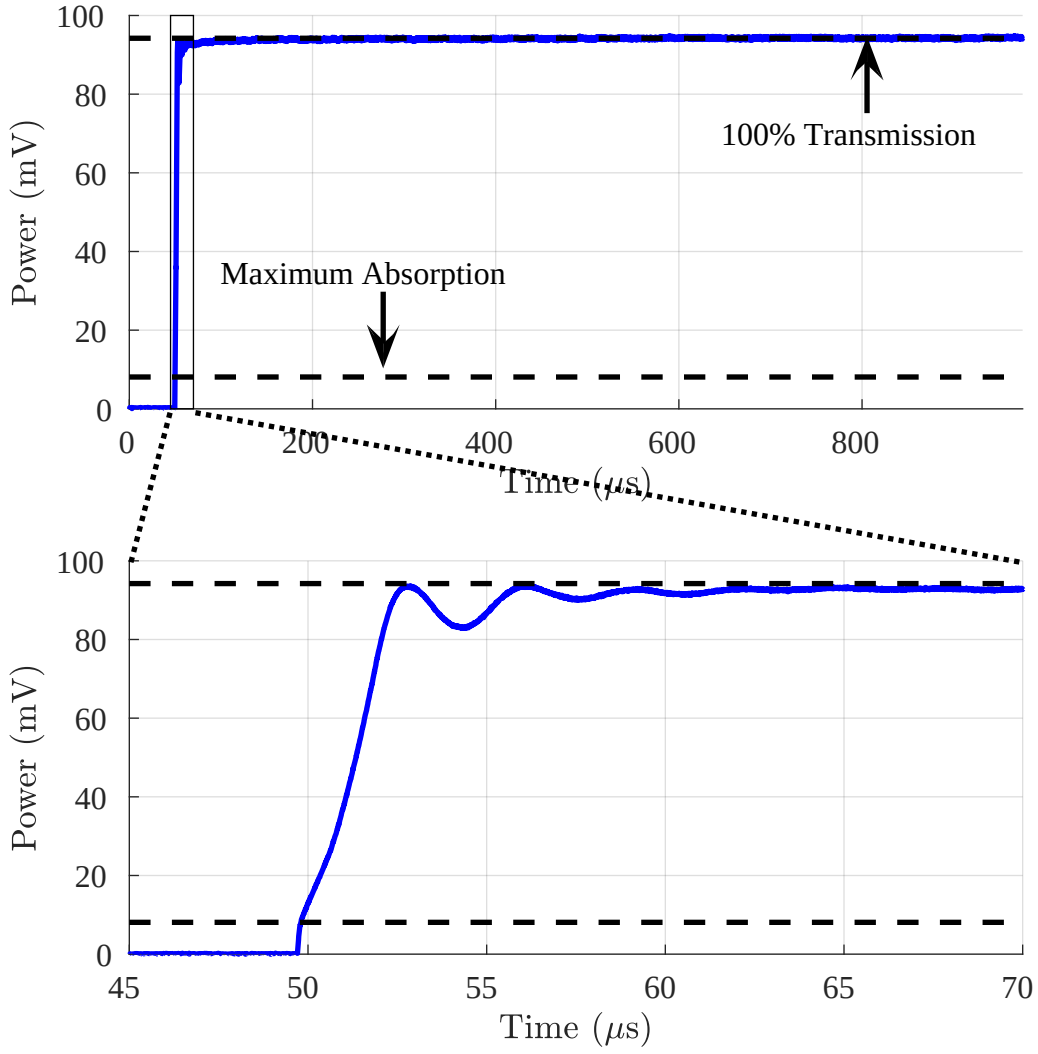

Figure 5.7: Top: Example of Rabi nutation for 15 mm long Tm^{3+}: YAG crystal at wavelength $\lambda = 793.3790$ nm. Bottom: Zoom in to show the turn-on edge.

Measured Absorption Spectrum

The absorption spectrum for two 0.1% Tm^{3+}: YAG crystals were mapped out, a small one with length $L = 10$ mm and thick one with length $L = 15$ mm. In total, three separate data measurements of the absorption spectrum were taken throughout the course of this research work. Two sets were done with the PP laser (the top left (TL) and top right (TR)) and one set for the NKT laser (bottom left (BL)). The

results of this are plotted in Fig. 5.8. In the TR, only the absorption measurements on the 10 mm crystal were taken. The data are fit to Lorentzian profiles.

This data demonstrates two things. First, the two sets with the PP laser were performed over two months apart, showing how the laser drifted over a two month time period can be seen. The difference is only 0.0008 nm, but this translates to a 381 MHz difference. This would be noticeable during spectral hole data collection had the laser not been re-characterized, again. Secondly, in the data from the NKT laser in the BL plot, its peak absorption frequency is, also, not 793.374 nm (relative to its internal caliibration), much like the top two. One last thing to notice is the difference in measurements from these three plots. The measurements in the BR are very uniform. This is a testament to how stable the NKT laser is. Meanwhile, the PP laser measurements tended to fluctuate more.

By adjusting the absorption measurements in all three cases, so that their peaks line up with 793.374 nm, all data are observed to have consistent heights and widths. They all measure the same peak absorption at the same point, seen in the BR of 5.8. These fits gave estimates on the required parameters needed for characterization of the crystals. Using the total combined data in Fig. 5.8, the findings are summarized in Table 5.1.

Table 5.1: Characterization of the two Tm^{3+}: YAG crystals used.

Crystal Length	$\alpha_0 L$ Data Fit	$\alpha_0 L$ Data Max	Material Bandwidth Γ_I
10 mm	1.8598	1.9274	16.9838 GHz
15 mm	2.4919	2.5390	16.8509 GHz

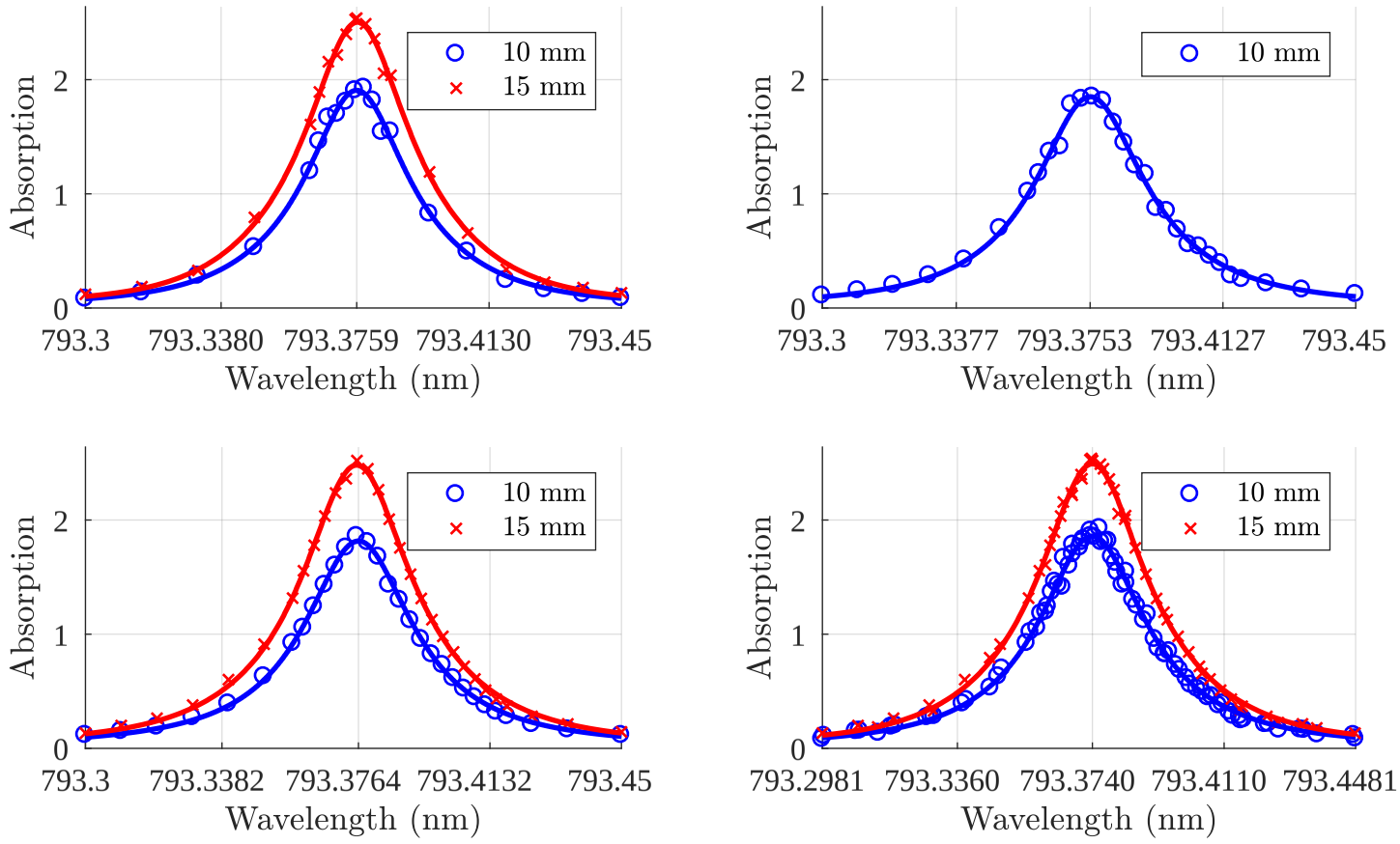

Figure 5.8: Absorption profile for 10 mm and 15 mm long Tm^{3+}: YAG crystals. The TL and TR plots were measured with the same PP laser, two months apart–demonstrating the laser drift. The BL plot was done with a NKTP laser. The BR plot is all three data sets, adjusted to 793.374 nm.

Gaussian vs. Lorentzian vs. Voigt Profile

One last matter to discuss, in this section, is displaying the difference between the Gaussian, Lorentzian, and Voigt profiles, as promised in Ch. 2. The combined data for the 15 mm long crystal is fit to a Gaussian profile, Lorentzian profile, and a Voigt profile in Fig. 5.9. The Gaussian fit is defined as

$$G(\lambda;\sigma) = a_1 \exp(-((\lambda - \lambda_0)/\sigma)^2) + c_1, \tag{5.16}$$

Lorentzian fit as

$$L(\lambda;\gamma) = \frac{a_2}{(\lambda - \lambda_0)^2 + (\gamma/2)^2)} + c_2. \tag{5.17}$$

The Voigt fit is traditional given as a convolution, as presented in Ch. 2. However, under certain conditions it may be modeled as a summation of both the Lorentzian and Gaussian shapes. This is known as a pseudo-Voigt profile [44], given by

$$V(\lambda;\sigma,\gamma) = (1-\eta)G(\lambda;\sigma) + \eta L(\lambda;\gamma), \tag{5.18}$$

where $0 \leq \eta \leq 1$. Thus, in this sense, V is defined as being part Gaussian and part Lorentzian. The fit parameters are in Table 5.2. In the Voigt fit, η was found to equal to one, meaning that no part of a Gaussian fits this profile. Hence, the Lorentzian is the best fit for this data. The GOF findings are summarized in Table 5.3.

Beam Waists

The beam waists of each of the three beams going into the crystal were also measured: the programming beam, the readout beam, and the reference beam. This

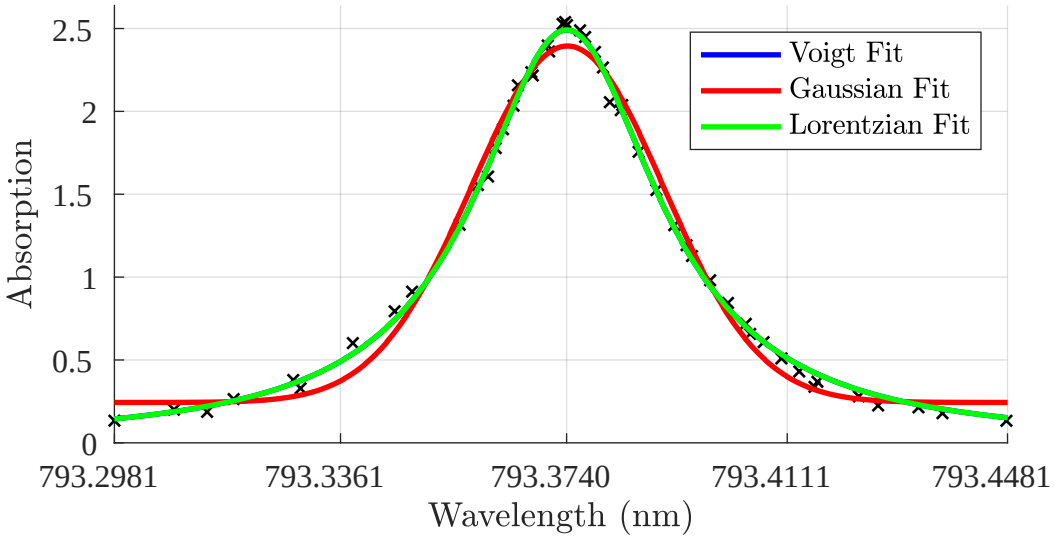

Figure 5.9: Absorption profile for 15 mm long Tm^{3+}: YAG crystal, with data fit to Voigt, Lorentzian, and a Gaussian profile. The Voigt is more accurate.

Table 5.2: Fit parameters for the data in Fig. 5.9.

	a_1	a_2	c_1	c_2	λ_0 (nm)	σ (nm)	γ (nm)	η
Voigt	0.8457	0.0009	N/A	N/A	793.3740	210.7369	0.0377	1
Gaussian	2.1509	N/A	0.2436	N/A	793.3742	0.0228	N/A	N/A
Lorentzian	N/A	0.0009	N/A	0.0000	793.3740	N/A	0.0400	N/A

Table 5.3: Goodness-of-fit for the data in Fig. 5.9, comparing a Voigt fit to a Gaussian fit and Lorentzian fit.

Profile	SSE	r^2	Adj. r^2	RMS Error
Voigt	0.0786	0.9979	0.9978	0.0413
Gaussian	0.3787	0.9900	0.9894	0.0898
Lorentzian	0.0786	0.9979	0.9978	0.0409

was done using two different methods. The first was by using a knife edge, and the other was by using an image detector and computer program.

Mathematically, assume the beams can be described as first-order Gaussian beams. For more information on the mathematics behind Gaussian beams, see [36], for example. The goal is to determine the waist radius for the three beams w_0. The beam radius as a function of distance z is given by

$$w(z) = w_0 \left[1 + \frac{z^2}{z_0^2}\right]^{1/2}, \tag{5.19}$$

where z_0 is the Rayleigh range. The waist w was measured at different distances z. This seems to leave one unknown, z_0. However, the Rayleigh range for a Gaussian beam is, in fact, related to the beam waist by

$$w_0 = \sqrt{\frac{\lambda z_0}{\pi}}, \tag{5.20}$$

where λ is the wavelength of the beam being used. Hence, (5.20) can be rearranged to be

$$z_0 = \frac{\pi w_0^2}{\lambda}, \tag{5.21}$$

so that

$$w(z) = w_0 \left[1 + \frac{\lambda^2 z^2}{\pi^2 w_0^4}\right]^{1/2}. \tag{5.22}$$

Now, instead of solving this equation for w_0, which is completely valid to do, values for w and z were measured, as stated. Then, those values are fitted to (5.22) in Matlab.

Knife Edge Method

There exists more than one method to determine the beam waist using a knife edge. One such method begins by starting with the definition of the Gaussian beam

$$E(r,z) = E_0 \exp(-r^2/w(z)^2). \tag{5.23}$$

This means the intensity of this beam is

$$I(r,z) = I_0 \exp(-2r^2/w(z)^2) = I_0 \exp(-2x^2/w(z)^2) \exp(-2y^2/w(z)^2). \tag{5.24}$$

Now, the goal is to occlude the beam using the knife edge from $-\infty \to w/2$ in the x direction at a given z location. This will occlude the fraction of the beam given by

$$\text{Fraction Occluded} = \frac{\int_{-\infty}^{w/2} \exp(-2x^2/w(z)^2)\mathrm{d}x \int_{-\infty}^{\infty} \exp(-2y^2/w(z)^2)\mathrm{d}y}{\int_{-\infty}^{\infty} \exp(-2x^2/w(z)^2)\mathrm{d}x \int_{-\infty}^{\infty} \exp(-2y^2/w(z)^2)\mathrm{d}y}. \tag{5.25}$$

The integrals over y cancel, and leaves only the ones in x. The bottom integral is a Gaussian integral, with a well known solution $w\sqrt{\pi/2}$, so that

$$\text{Fraction Occluded} = \frac{1}{w}\sqrt{\frac{2}{\pi}} \int_{-\infty}^{w/2} \exp(-2x^2/w(z)^2)\mathrm{d}x. \tag{5.26}$$

By making the substitution of $x' = \sqrt{2}x/w$, one finds that

$$\text{Fraction Occluded} = \frac{1}{\sqrt{\pi}} \int_{-\infty}^{\sqrt{2}/2} \exp(-x'^2)\mathrm{d}x'. \tag{5.27}$$

Now, break the integral up, so that

$$\int_{-\infty}^{\sqrt{2}/2} \exp(-x'^2)\mathrm{d}x' = \int_{-\infty}^{0} \exp(-x'^2)\mathrm{d}x' + \int_{0}^{\sqrt{2}/2} \exp(-x'^2)\mathrm{d}x'. \tag{5.28}$$

The first integral is another Gaussian integral with solution $\sqrt{\pi}/2$. The second term is recognized as the error function, defined as

$$\mathrm{erf}(x) = \frac{2}{\sqrt{\pi}} \int_{0}^{x} \exp(-t^2)\mathrm{d}t. \tag{5.29}$$

Thus,

$$\text{Fraction Occluded} = \frac{1}{2}\left[1 + \mathrm{erf}\left(\sqrt{2}/2\right)\right] = 0.841345. \tag{5.30}$$

This means that by occluding 84% of the total power, and transmitting 16%, then the knife edge is a distance $w/2$ away from the center of the beam. Therefore, by measuring from 16% to 84% the knife is displaced by w.

In practice, one measures a distance z from the focal distance of the launcher. The focal distance should be the point where the beam is the tightest, and this is the value that should be centered on the crystal. The beam launcher has a 250 mm focal length. If the waists are found to be at a minimum of some distance away from 250 mm, where $z = 0$ point is set, then either the z measurements are slightly off and the beam launcher needs to be adjusted accordingly, the focal length is not exactly 250 mm, or the fiber collimators are not perfect (i.e. the beams are not collimated before the lens).

At each point z, the total transmitted power from the beam is recorded using a power meter. Then, what should be the 84% and 16% transmission marks are calculated. From there, a calibrated translation stage with the knife edge attached to

it is used. Carefully, the stage is adjusted until it hits these points x_1 and x_2 in the x-direction. The difference between them is the beam waist at the Rayleigh range z_0,

$$w(z_0) = |x_1 - x_2|. \tag{5.31}$$

Beam Profiler Method

The beam profiler method is easier. Using an Ophir Beamstar beam profiler and software, the beam radius is computed, with a software package, in both the x and y directions. Then, the results are simply recorded. The downside is that these measurements are not entirely accurate, which may be surprising as one would think a computer-recorded data would be more accurate than hand-recorded data. This is a result of the software used.

Summary of Data Collected

A complete summary of the data points collected is found in Table 5.4. This data was entered into Matlab and fit to (5.22). However, it was used in a slightly different form, however. To allow for a displacement along z (i.e. the zero-point was off), the data are fit to

$$w(z) = w_0 \left[1 + \frac{\lambda^2 (z - z')^2}{\pi^2 w_0^4}\right]^{1/2}. \tag{5.32}$$

The fits are found in Fig. 5.10.

Table 5.4: Measurements of the beam waists using a knife edge and computer software.

	Knife (z in cm, w in μm)					**Computer** (z in cm, w in μm)					
Prog.	z	4.0	14.9	22.6	37.7	z		9.9	15.8	24	31
	w	160	248	313.3	586	w	H	169.5	236	314	430.5
						w	V	145.5	227	307.5	418
Read.	z	8.3	13.5	22.1	39.7	z		9.9	16	22.5	32.1
	w	180.5	175	296.7	572.5	w	H	141	194	265	417.5
						w	V	138	197	295	393
Ref.	z	8.3	13.5	22.1	39.7	z		11.1	15.2	22	31.6
	w	200	181.3	272	526	w	H	167.5	199.5	273.5	403
						w	V	174.5	212.5	273	408.5

By combing all sets of data points onto one figure, a single estimate on the beam waist and offset can be obtained. The single figure with all three sets of measurements is found in the bottom right of Fig. 5.10. With it, Matlab gave that the beam waist was $w_0 = 156$ μm and offset by $z' = 7$ cm.

Beam Overlap

An important component of this system is the beam overlap in the crystal. The programming and readout beams need to be as overlapped as possible to achieve best sensitivity and record the spectral holes as accurately as possible. A method for estimating the overlap was developed using geometric methods. To find the overlap, the following quantities need to be measured:

- the length of the crystal = L,
- the distance from the launcher to the crystal (approx. the focal length),

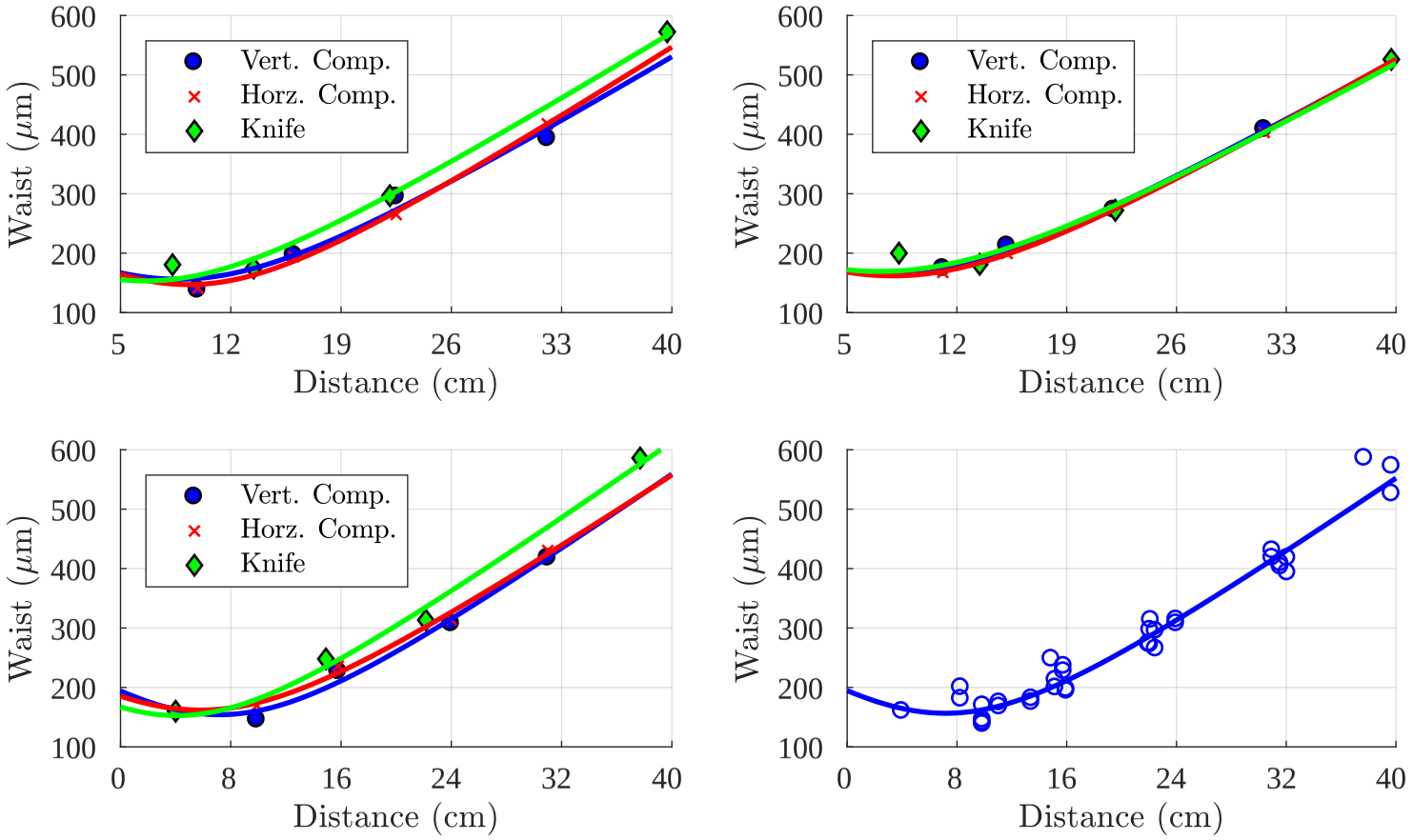

Figure 5.10: Beam waist measurements for the readout beam (top left), reference beam (top right), programming beam (bottom left), and all three sets combined (bottom right).

- the distance between the programming and readout beams as they exit the launcher,
- the radius of the beams.

Assuming these quantities are measureable, the approach to measuring the overlap of the beams is as follows. First, the angle between the beams inside the crystal is needed. This done using simple trigonometric methods. If the distance between the launcher to the crystal is x and the distance between the two beams at the point of the launcher is y, then the angle between them is

$$\beta = \arctan\left(\frac{y}{x}\right). \tag{5.33}$$

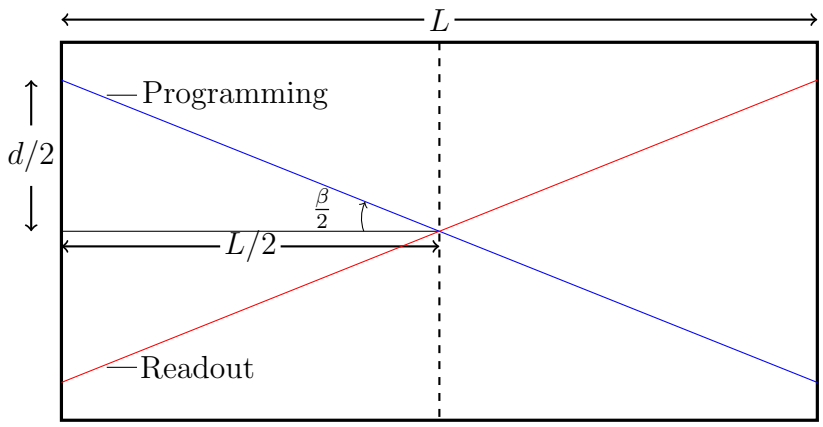

Figure 5.11: Some of the geometry involved.

The next thing to find is the distance between beam centers. Throughout this analysis the beams are modeled as infinite cylinders of equal radii, R. For reference, use Fig. 5.11. Assuming that they intersect in the center of the crystal, a distance $L/2$ from where they enter the crystal, then two right triangles can be created, from a side-view perspective, by drawing a bisecting line from their point of intersection to the where they enter the crystal. The distance between their center radii and this

bisection would thus be

$$d/2 = \frac{L}{2} \tan \frac{\beta}{2}. \tag{5.34}$$

The total distance between their centers at the point of entering the crystal is

$$d = L \tan \frac{\beta}{2}. \tag{5.35}$$

Now, to get the volume of overlap, it is necessary to integrate, but the coordinates need to be set, first. In the perspective of the beams, looking down the long axis of the crystal, one would see two intersecting circles. Center the coordinate system on one of the two circles, and label it A, so that it could be described by the equation

$$x^2 + y^2 = R^2 \tag{5.36}$$

in Cartesian coordinates. The area of this circle is $A_1 = \pi R^2$. The second circle will be separated from the first by the value of d. Hence, it may be described by

$$(x - d)^2 + y^2 = R^2. \tag{5.37}$$

This view of the two beams can be seen in Fig. 5.12, with the black area being their overlap. This can be expanded to find that

$$x^2 + y^2 - 2dx + d^2 = R^2. \tag{5.38}$$

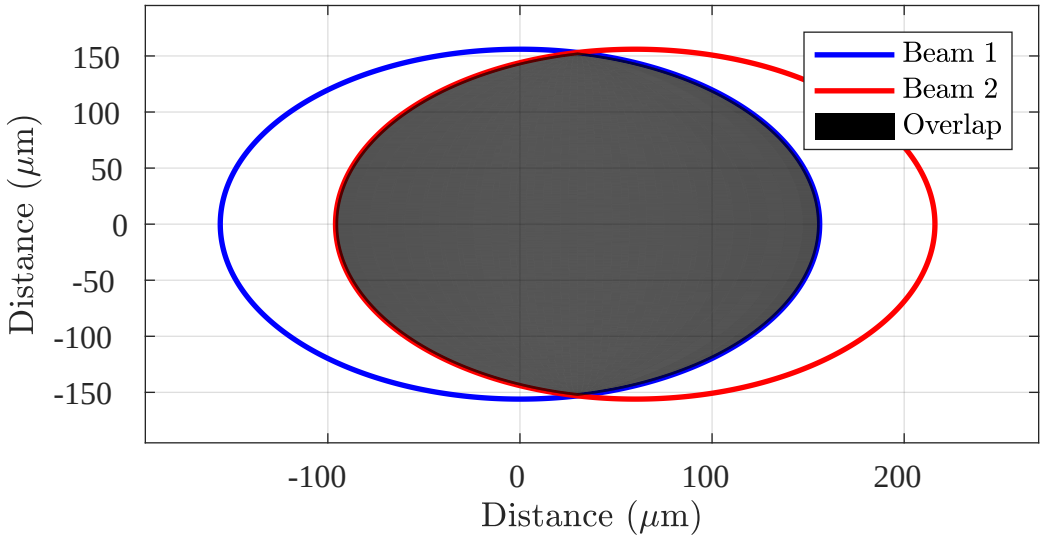

Figure 5.12: Overlap of two beams, with one beam serving as the center of the coordinate system for 10 mm long crystal.

Converting this to polar coordinates, the equation becomes

$$r^2 - 2dr\cos\theta + d^2 = R^2. \tag{5.39}$$

The area not overlapped in circle 1 from circle 2 is therefore

$$A = A_1 - A_2 \tag{5.40}$$

$$= \pi R^2 - \int_0^{2\pi}\int_0^R (r^2 - 2dr\cos\theta + d^2) r\mathrm{d}r\mathrm{d}\theta \tag{5.41}$$

$$= \pi R^2 - \frac{2}{3}\pi R(3d^2 + R^2). \tag{5.42}$$

The total volume not overlapped for this crescent shape is approximated by multiplying this area by the length over which it was analyzed $L/2$. Yet, there is the opposite, bottom side to add to this, which introduces a factor of 2. There will be another factor that would come from the volume integral. The shape that this crescent takes three dimensionally will be somewhere between a wedge and a pyramid.

The difference is a factor of 1/3 for the pyramid or 1/2 for the wedge. So, this gives some bounds of the volume of non-overlap to be

$$\frac{AL}{3} \leq V_{NO} \leq \frac{AL}{2}. \tag{5.43}$$

There may be other factors here that would need to be accounted for, owing to the crescent shape.

One last piece, the volume of one of the beams inside the crystal is needed. The only thing needed for this is the angle at which one beam enters the crystal with respect to the surface normal. This can be found be using the intersection method from before. The angle at which one of the beams enters can be given by

$$\alpha = \pi - \pi/2 - \beta/2 = \frac{\pi - \beta}{2}. \tag{5.44}$$

The volume of the cylinder at this angle is then

$$V = \pi R^2 L \sin\alpha. \tag{5.45}$$

The percent that the beams overlap is, therefore,

$$P = 1 - \frac{V_{NO}}{V}. \tag{5.46}$$

Assuming the high end of overlap, this is

$$P = 1 - \frac{A}{3\pi R^2 \sin\alpha}. \tag{5.47}$$

In the lab, it was measured that $x \approx 250$ mm and $y \approx 3$ mm. This gives an angle $\beta = 0.012$ rad. Using the previous section, assume that radii of the beams are

$R = 156$ μm. The rest of the data is summarized in Table 5.5. The significance of this is that the maximum, approximate overlap that can be attained between the two beams would be about 80%.

Table 5.5: Beam Overlap Measurements.

L	d	A	V_{NO}	α	V	P
10 mm	0.06 mm	0.0650 mm^2	0.162 mm^3	1.56 rad	0.764 mm^3	0.79
15 mm	0.09 mm	0.0606 mm^2	0.227 mm^3	1.56 rad	1.149 mm^3	0.80

Having covered the methods used in the lab, the following chapter presents the results from the experiment. When taking data, the knowledge that was just gained about the $\alpha_0 L$ of the crystals, as well as the corresponding wavelengths, were taken into account to achieve the maximum possible absorption in the experiment

RESULTS

Dynamic Range and the Limits of Linear Recovery

In this chapter, the findings for the nonlinear recovery are presented, starting with the dynamic range (DR) for the linear recovery algorithm. DR is the range of signals this system can resolve, before reaching saturation or the noise floor. This allows for easy identification of two types of data: those that are in the linear regime and those that are in compression. Data that is in compression will be highly nonlinear, and, thus, require the new recovery technique. In this case, saturation occurs for deep holes, with high chirp rate, and height $\alpha_0 L$. Once it is identified where the nonlinear regime occurs, the algorithm can be applied to it. The nonlinear factor will be characterized for each of the two Tm^{3+}: YAG crystals that were used, by observing how the factor behaves when the RF power, optical chirp power, and absorption length $\alpha_0 L$ are changed for single tones.

For single tone characterization, a RF signal generator that sent in a tone at 700 MHz was used as the SOI. In the experiments, the RF power was varied from 16 dBm down to as low as -20 dBm on the thicker crystal and -24 dBm for the smaller crystal. Also, the optical chirp power was varied from 10.5 mW down to 0.5 mW on the thicker crystal. Data were recovered using the linear recovery algorithm, and the peak value was then recorded and stored. The linear recovery algorithm was used, because, even if it is nonlinear, the peak amplitude is very close to where it should be. Also, it scales the peaks with hole depth, giving an accurate behavior, even if the exact scaling is off. The results are plotted in Fig.'s 6.1 and 6.2.

Changing the RF power should have a response corresponding to that of Eqn. (5.5). On the log scale, $10\log_{10}|V| = 10\log_{10}(|J_1(\pi V_{RF}/V_\pi)|^2) +$ constant, where V is the detector voltage ($V \propto I$), J_1 indicates the 1st-order Bessel function of the

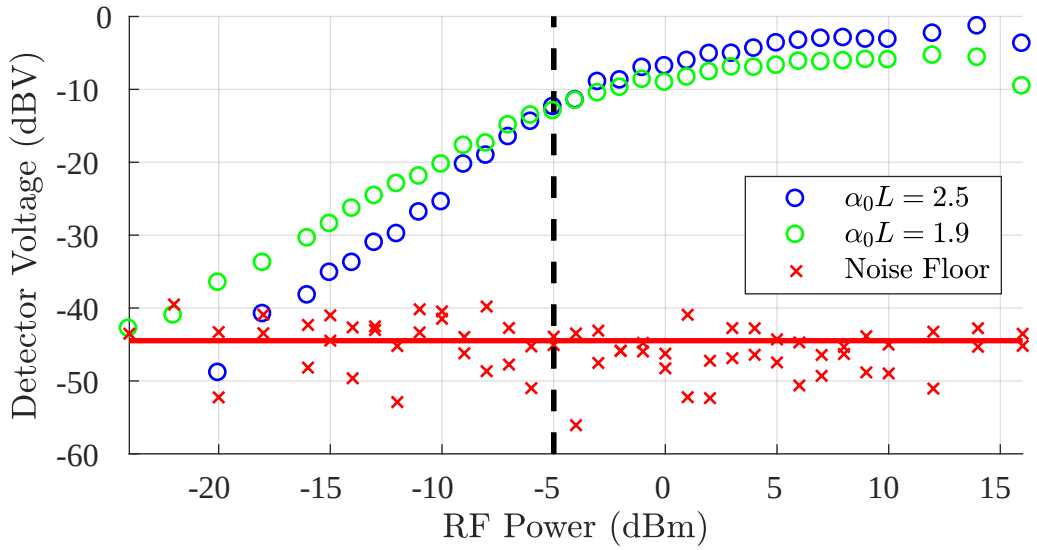

Figure 6.1: DR for Tm^{3+}: YAG with varying RF power. The optical chirp power was $P_{\text{chirp}} = 7.7$ mW for $\alpha_0 L = 2.5$ and $P_{\text{chirp}} = 7.5$ mW for $\alpha_0 L = 1.9$. $P_{\text{RF}} = -5$ dBm is highlighted here, as it marks the onset of compression.

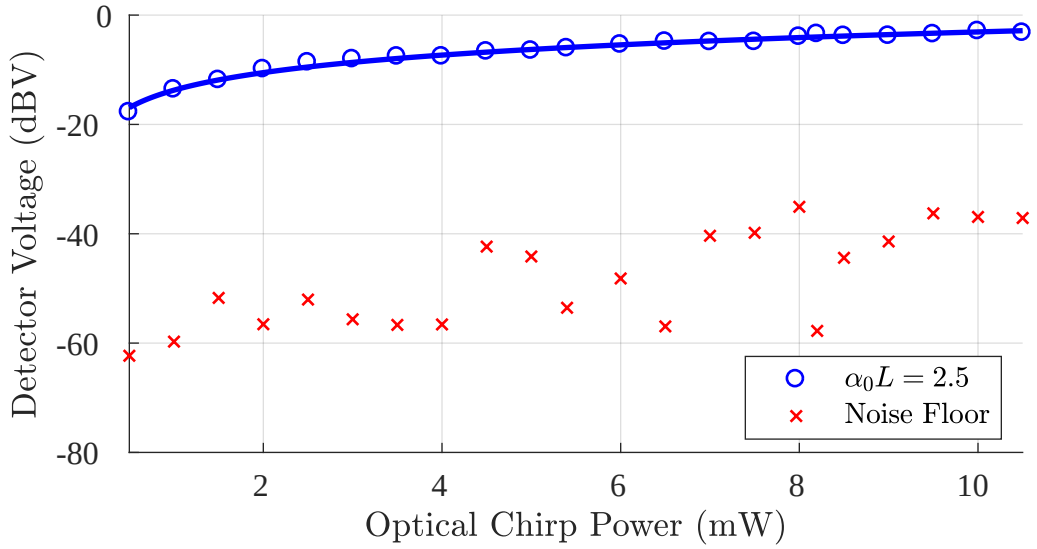

Figure 6.2: DR for Tm^{3+}: YAG with varying optical chirp power. The RF Power was $P = 16$ dBM.

First Kind (J_0 would be for carrier), V_{RF} is the applied RF voltage driving the EOM, and V_π is the half-wave voltage. The constant term is the appropriate scaling value after going through the system. Unlike the chirp laser setup, where the 2nd-order was selected–as described in Ch. 5, the 1st-order is now used. Changing the optical chirp power should have a linear response, so, on the log scale, it simply goes as $10\log_{10}|V| = 10\log_{10}(P_{\mathrm{chirp}}) +$ constant, where P_{chirp} is the optical chirp power, and the constant term is the appropriate scaling value after going through the system. The curves Fig. 6.2 is fit to $a10\log_{10}(bP_{\mathrm{chirp}}) + c$, with $a = 1.065$, $b = -0.2289$, and $c = -6.909$. From Fig. 6.1, it is identified that the system is well into compression when the RF power is at -5 dBm or greater. Compression is when the output voltage levels out and so it changes very little, for an increasing input RF voltage. This flattens out the data at that point. The optical chirp power was maintained between 7-8 mW, for these measurements.

Selecting data at 10 dBm for both the larger crystal and smaller crystal can exemplify what should be seen for nonlinear behavior, plotted in Fig. 6.3. In the lab, 20 traces per data item were taken at any given time. Each trace was summed point-wise with the other traces, and an overall median value was stored for each point. The median was chosen over the mean to account for variability in the data that might throw off what the actual value should be. This is what is seen plotted, except in the top left, where a single raw trace of detected power is plotted, for reference. These recovered data are clearly nonlinear, even on the linear scale, and will require the nonlinear algorithm for best performance.

Conversely, looking at a low RF power of -10 dBm, it can be seen that the linear recovery algorithm is working fine in Fig. 6.4. Despite the lack of needing an additional correction term, the nonlinear algorithm could be applied here, too. It just wouldn't do much, since the system is already in a regime where $\alpha(\nu)L$ is small

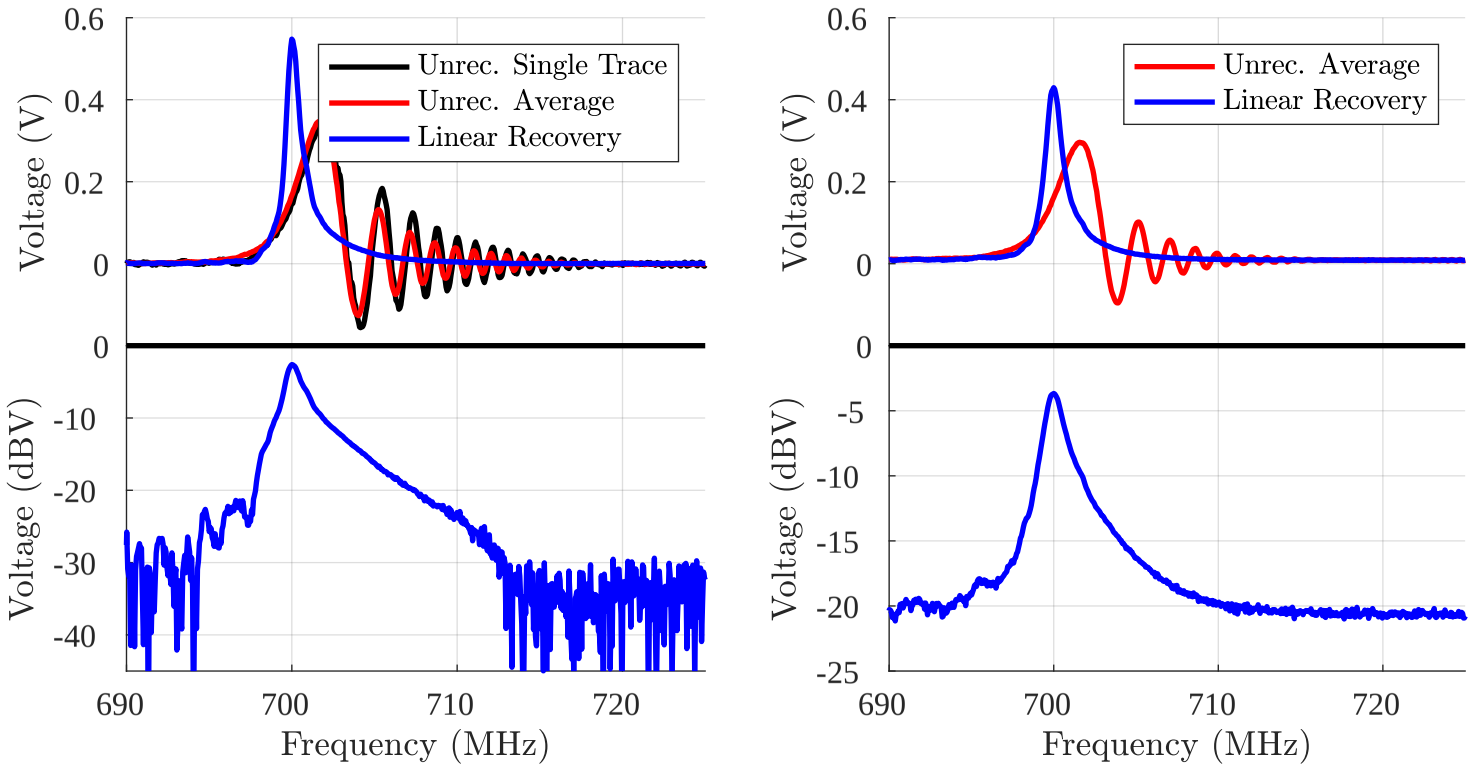

Figure 6.3: (Top Left) Linear recovery for $\alpha_0 L = 2.5$, RF Power $P_{\text{RF}} = 10$ dBM, Chirp Power $P_{\text{chirp}} = 7.7$ mW. A raw detected trace and an averaged detected traced are plotted here, as well. (Bottom Left) Log of Top Left. (Top Right) Linear recovery for $\alpha_0 L = 1.9$, RF Power $P_{\text{RF}} = 10$ dBM, Chirp Power $P_{\text{chirp}} = 7.5$ mW. An averaged detected trace is also plotted. (Bottom Right) Log of Top Right.

compared to $\alpha_0 L$, and a linear approximation is just as good as a second-order one.

Finally, two different chirp powers are examined. One at 7.5 mW and one at 3.5 mW, seen in Fig. 6.5. The main thing to note here, is that as the power gets lower, the signal just sinks into the noise floor. The nonlinearity remains.

Additionally, and with some foresight in mind, there are differences between what is seen in Fig. 6.5 and Fig. 6.3. They should be the same, given that the three parameters are essentially equal. They are not, however. The reason for this is that the data taken for each were performed in different time periods. In between that time, the setup was taken down and had to be rebuilt. As a result, the holes that were burned came out differently. It can be seen that the holes from the later data are about 1/3rd the depth and less than 1/3rd as wide (about 1.1 MHz compared to about 0.3 MHz). This could be due to any number of reasons, none having to do with the materials or parameters listed in this chapter. One possible reason is that the overlap in the crystal could have been reduced, due to poor beam overlap in the material. This will have some effect on the results, but, since this is known, it can be accounted for going forward.

The fact that the data sets are different can be a benefit, since it gives the opportunity to observe real data analysis on two different hole types. The change of hole depth between the two data sets, won't effect any features. However, the change in hole widths does effect the signal. By looking at the ring out, for example, it can be seen that the shallow, thin hole has a ring out that is twice as long (about 40 MHz wide) as the deep, thick hole (about 20 MHz).

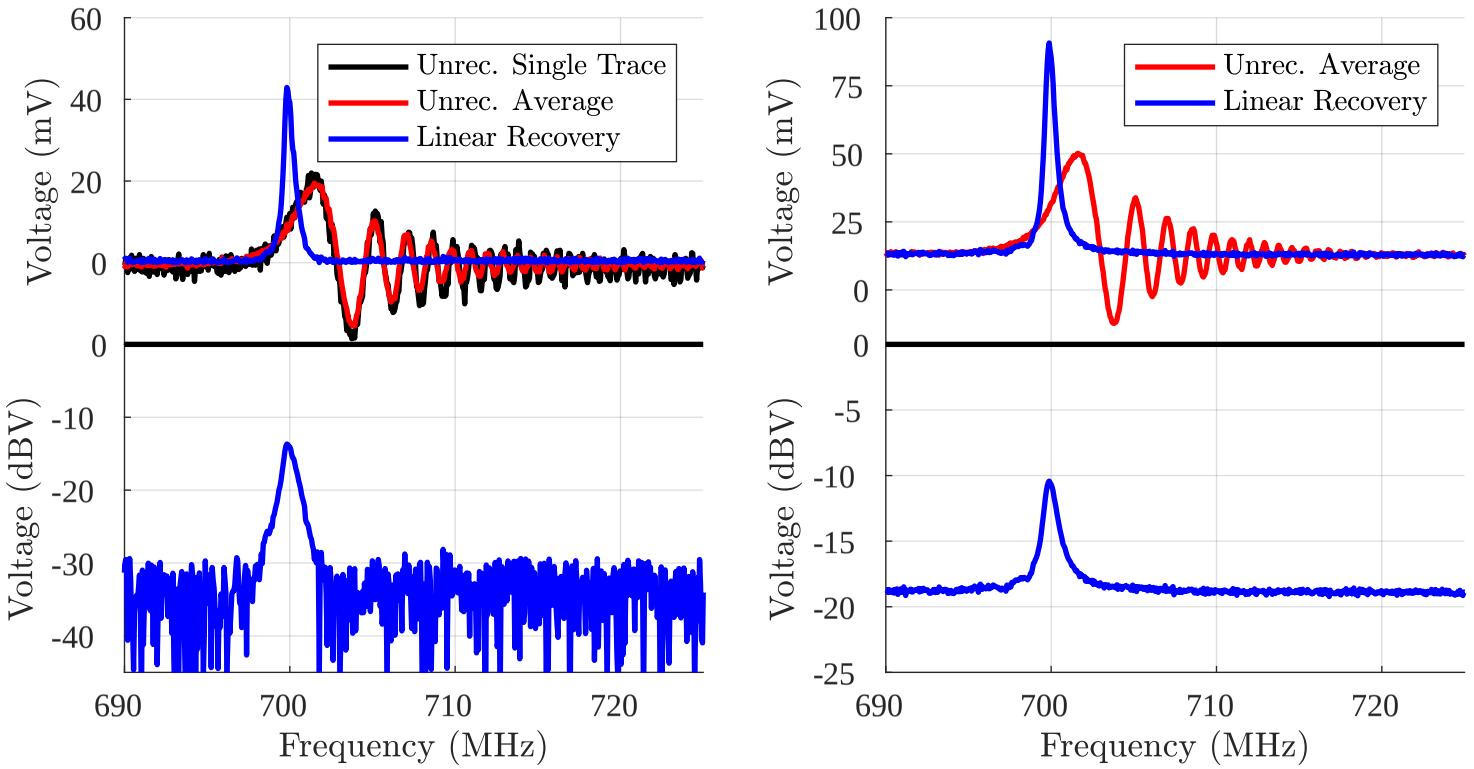

Figure 6.4: (Top Left) Linear recovery for $\alpha_0 L = 2.5$, RF Power $P_{\text{RF}} = -10$ dBM, Chirp Power $P_{\text{chirp}} = 7.7$ mW. A raw detected trace and an averaged detected traced are plotted here, as well. (Bottom Left) Log of Top Left. (Top Right) Linear recovery for $\alpha_0 L = 1.9$, RF Power $P_{\text{RF}} = -10$ dBM, Chirp Power $P_{\text{chirp}} = 7.5$ mW. An averaged detected trace is also plotted. (Bottom Right) Log of Top Right.

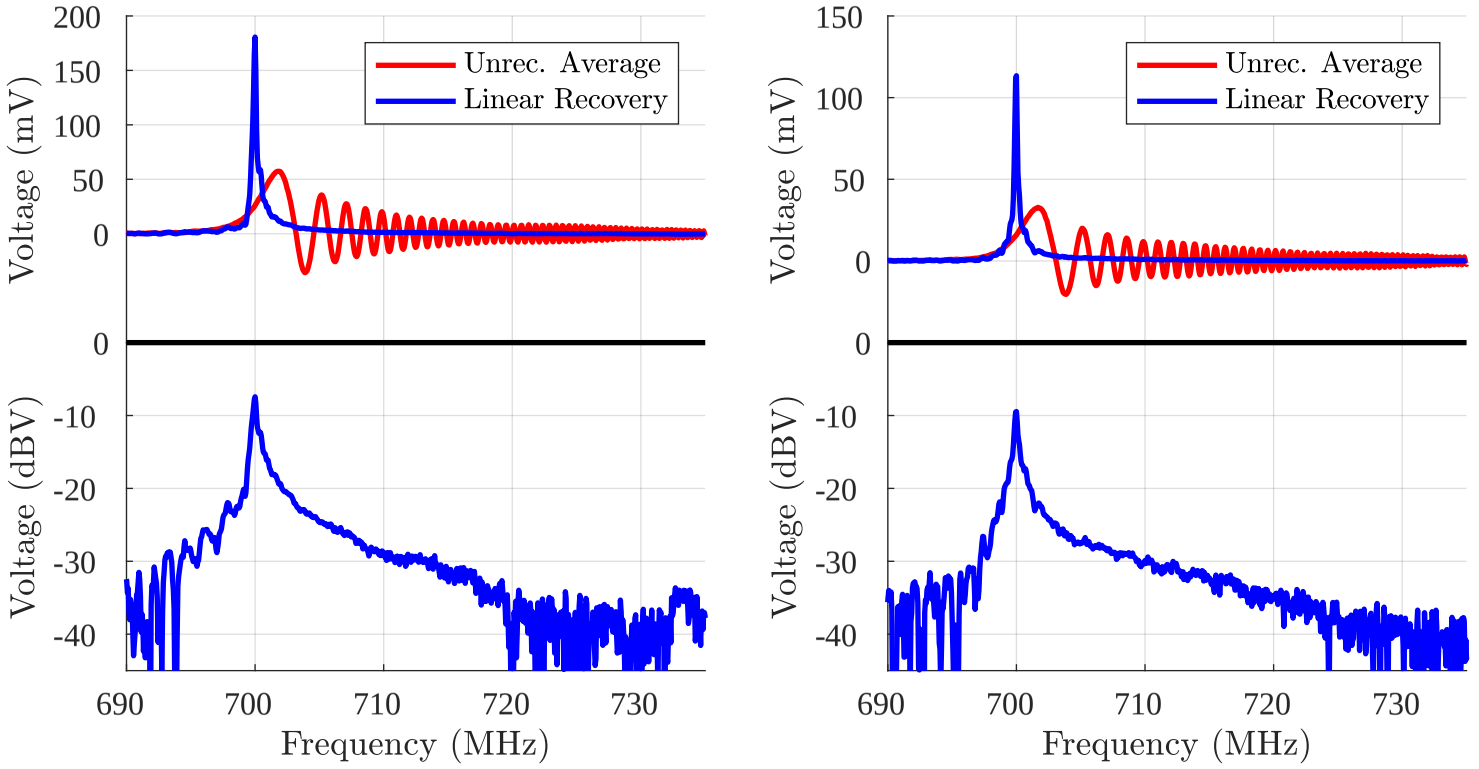

Figure 6.5: (Top Left) Linear recovery for $\alpha_0 L = 2.5$, RF Power $P_{\text{RF}} = 16$ dBM, Chirp Power $P_{\text{chirp}} = 6.5$ mW. (Bottom Left) Log of Top Left. (Top Right) Linear recovery for $\alpha_0 L = 1.9$, RF Power $P_{\text{RF}} = 16$ dBM, Chirp Power $P_{\text{chirp}} = 3.5$ mW. (Bottom Right) Log of Top Right.

Applied Nonlinear Recovery

$\mathcal{L}$-factor Characterization

Now that the regimes that will require the nonlinear recovery have been identified, the new algorithm needs to be applied. However, the values of $\mathcal{L}$ that work best for these two different materials still need to be identified. To this end, various $\mathcal{L}$-values were cycled through, as was done in Ch. 3. The goal is to find which one gives the best RMSE when comparing the LHS of the signal with the RHS. To be clear, the best overall value that could be applied, no matter what the input parameters are, is what is sought.

RF Power Dependence First, how the $\mathcal{L}$-factor changes with RF power, while holding the chirp power and absorption constant, was found. This can be seen in Fig. 6.6. The figure displays data from both crystals. The overall $\mathcal{L}$-factor was determined by taking the mean of the points. For the 15 mm crystal, $\mathcal{L} = 0.965$, and, for the 10 mm crystal, $\mathcal{L} = 0.83$. The fact that these two factors remain relatively constant means that the factor itself is independent from the RF power and, therefore, hole depth. This is important, because the algorithm should be independent of the hole.

Chirp Power Dependence When the chirp power was changed, an asymptotic relationship was found for the factor. That is $\mathcal{L} \propto 1/P_{\text{chirp}}$. This relationship is due to a normalizing component. This is seen in Fig. 6.6. At low powers, below 3.5 mW, the factor quickly increases, while it seems to be settling down to a constant for higher powers. Here, data is displayed from 3.5 mW to 10.5 mW, which follows a linear trend, as well as the data down to as low as 0.5 mW.

The two sets of data, plotted for the chirp power dependence in Fig. 6.6, correspond to two different hole widths . The blue line corresponds to the actual data

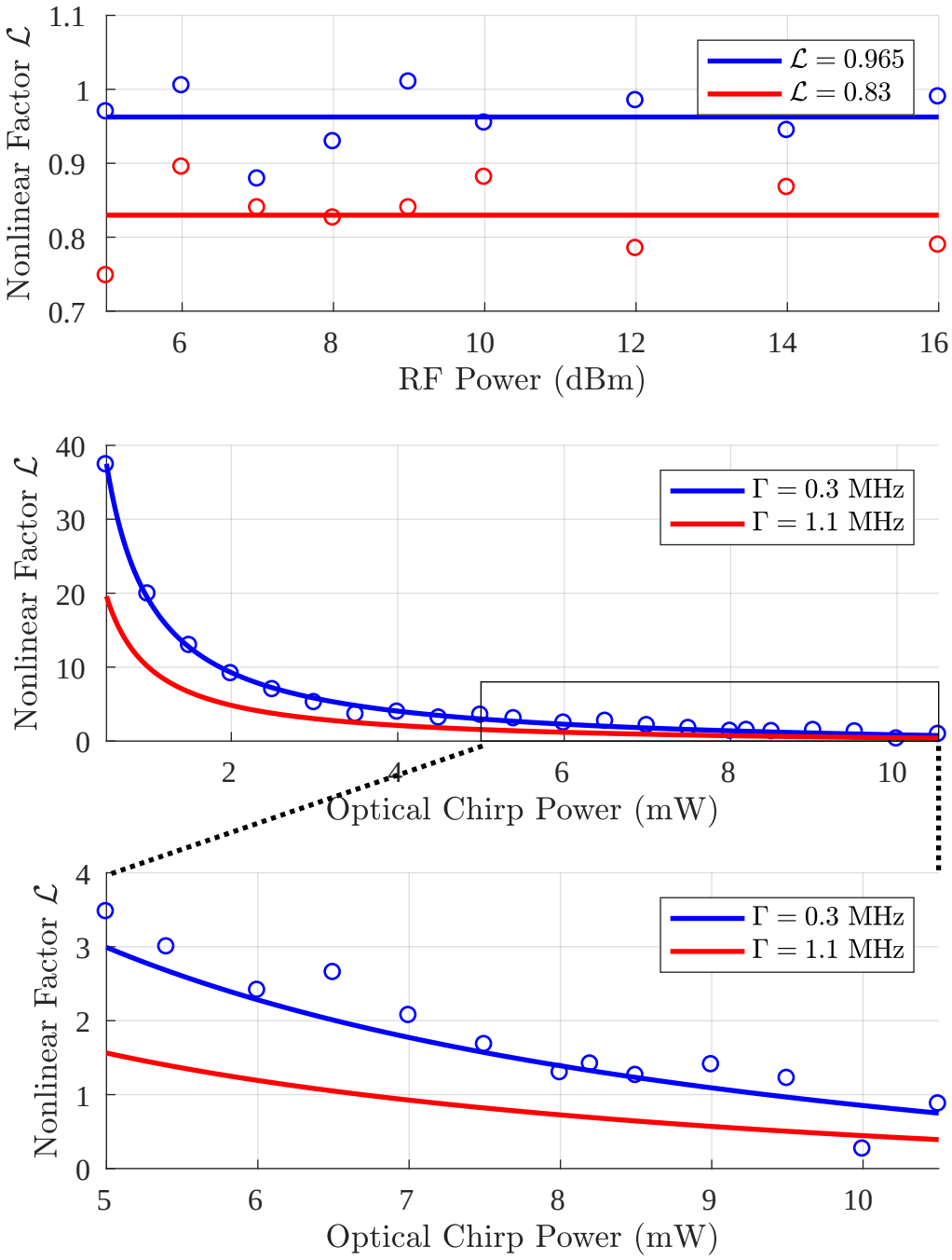

Figure 6.6: (Top) Change in $\mathcal{L}$ as a function of RF power for a single tone at 700 MHz. Blue line is for $\alpha_0 L = 2.5$. Red line is for $\alpha_0 L = 1.9$. (Center & Bottom) Change in $\mathcal{L}$ as a function of chirp power for a single tone at 700 MHz.

taken for a changing optical chirp power with hole width $\Gamma = 0.3$ MHz. This data was taken at a different time than the data presented for the RF power dependence. The red line is guessed to correspond to a hole width of $\Gamma = 1.1$ MHz, which would correspond to the width from Fig. 6.3 and the data from Fig. 6.6. It was determined by taking the ratio of the $\mathcal{L}$-factor for the same RF power, $\alpha_0 L$, and chirp power, but different hole widths. The fact that this is off could be due to an issue with beam overlap in the crystal between data sets, detector issues, or some other lab problem. The main point is that after you characterize these value once, for a given setup, they would remain consistent and independent of hole width.

Nonlinear Suppression

Now, that the $\mathcal{L}$-factor has been determined, the nonlinear recovery can be looked at with it working, as well as the amplitude difference in the tail that was first talked about in Fig. 1.3. Fig. 6.7, displays, visually, how adding in the nonlinear correction term effects the holes at an RF power of 10 dBm. Fig. 6.8 shows the amplitude difference between the linear recovery and nonlinear recovery for these figures, getting about 5 dBV difference for the smaller crystal and over 10 dBV for the larger one.

Nonlinear Recovery on Arbitrary Spectra

For reference, the $\mathcal{L}$-factor from this point on is different than above, as the data was taken at a different time and now corresponds to the $\mathcal{L}$-value from the Center and Bottom of Fig. 6.6. The optical chirp power in all cases was kept to be 7.1 mW, corresponding to $\mathcal{L} = 1.727$.

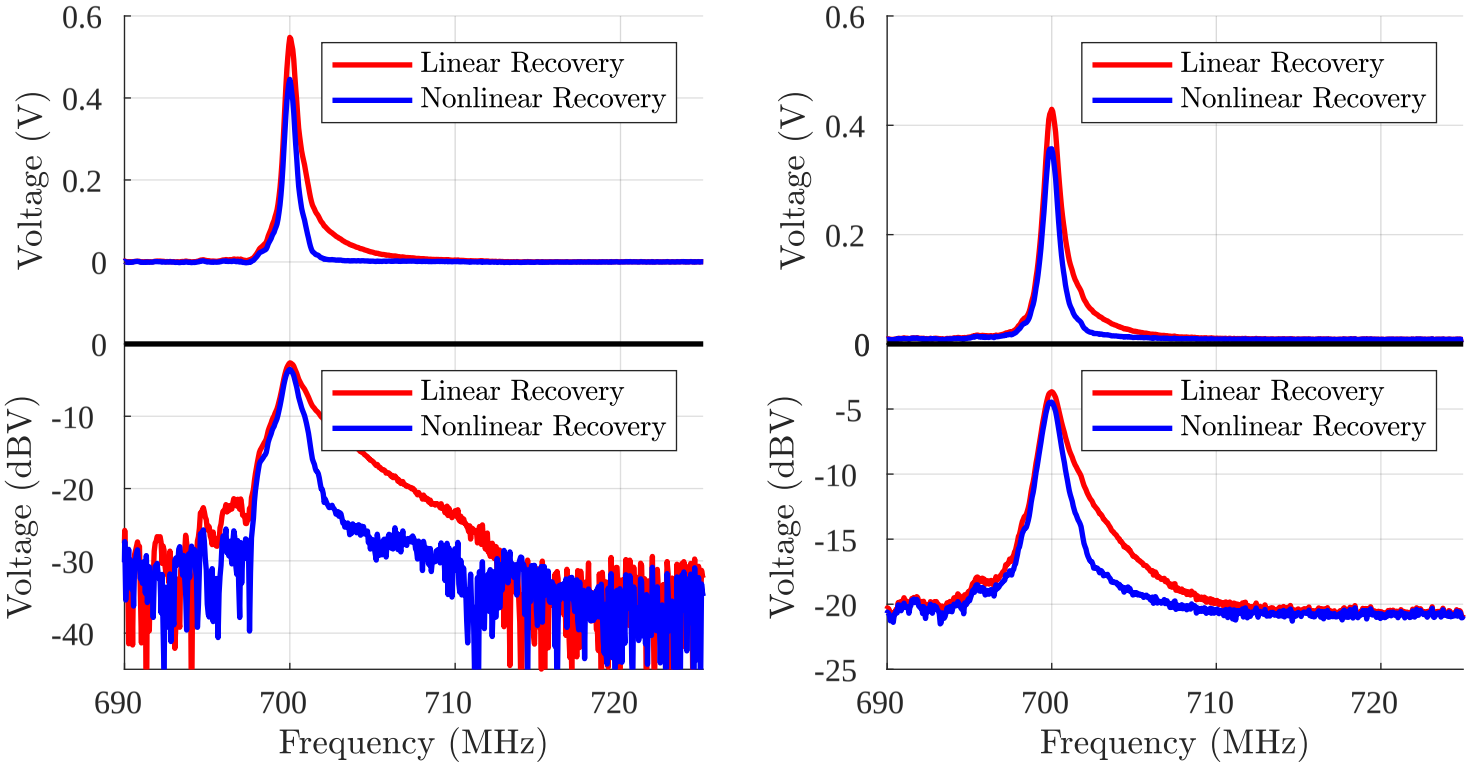

Figure 6.7: (TL) Linear and nonlinear recovery for $\alpha_0 L = 2.5$, RF Power $P_{\text{RF}} = 10$ dBM, Chirp Power $P_{\text{chirp}} = 7.7$ mW, $\mathcal{L} = 0.965$. (BL) Log scaling of TL. (TR) Linear and nonlinear recovery for $\alpha_0 L = 1.9$, RF Power $P_{\text{RF}} = 10$ dBM, Chirp Power $P_{\text{chirp}} = 7.5$ mW, $\mathcal{L} = 0.83$. (BR) Log scaling of TR.

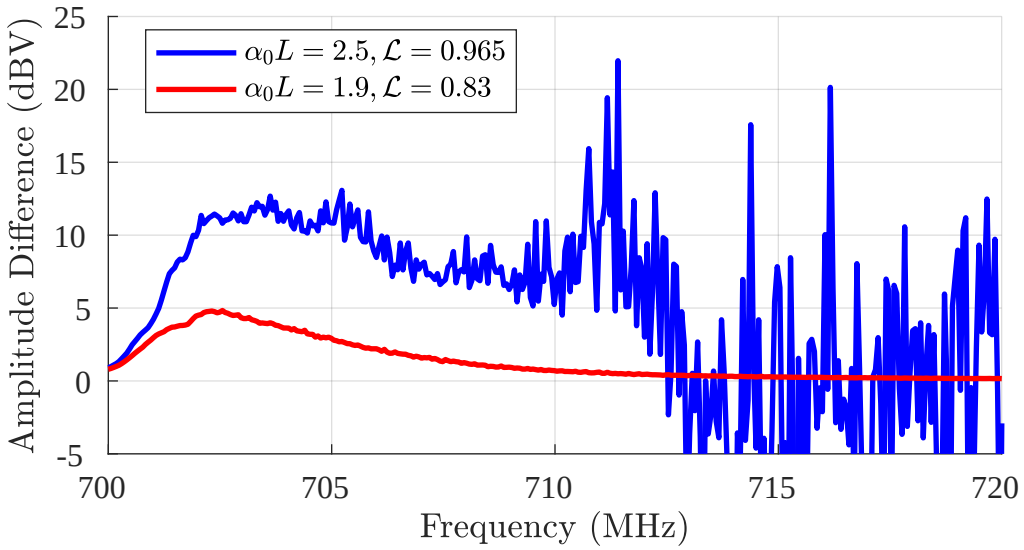

Figure 6.8: Figure shows the amount of tail suppression for the indicated material. The curves correspond to Fig. 6.7.

Multiple Holes

Now, the resolution that can be achieved by using the nonlinear recovery on secondary spectral holes is sought. Two signals from two separate signal generators were summed to do this. The main hole remained at 700 MHz, while a second tone was set anywhere between 701-740 MHz away. Chirp power was maintained around 7.1 mW, and RF power of the main hole was set to 12 dBm. The goal here was to see what kind of peak heights the linear recovery produces against the nonlinear recovery. The behavior should be something that was seen in Fig. 4.14. The peak amplitudes for the linear and nonlinear recoveries are plotted in Fig. 6.9 for each crystal, with the second hole at 705 MHz. Essentially, around 10 dBV difference is gained between linear and nonlinear. Again, this is on weak main holes, and weak sidebands.

As an example of this working in action, a double hole is plotted in Fig. 6.10 that shows this behavior. The dotted line shows where the second hole is. It has a power of -10 dBm. The nonlinear recovery gives more shape to the side hole, aside from lowering its amplitude.

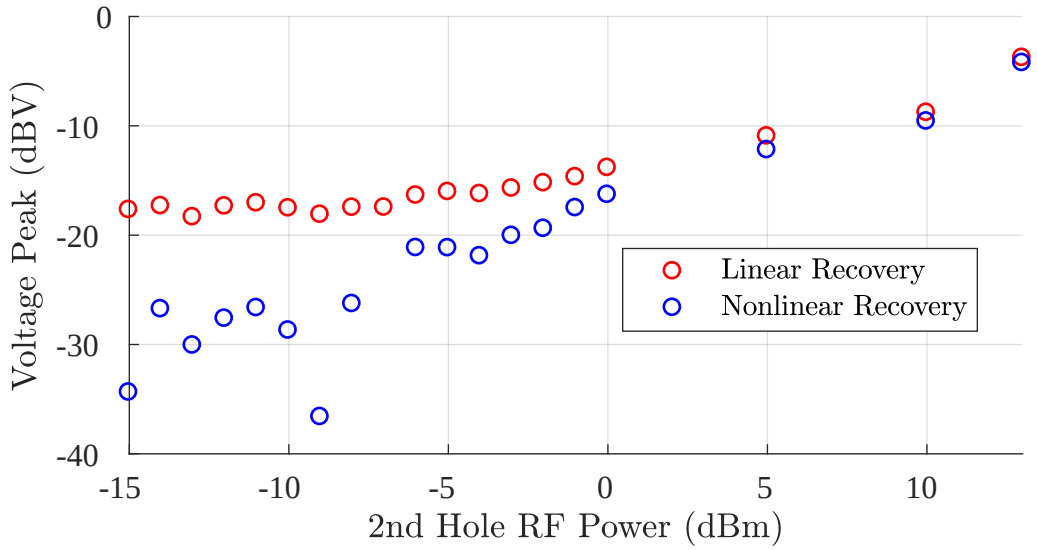

Figure 6.9: Measured peak amplitude for 2nd hole located 5 MHz away from a 12 dBm main hole, for $\alpha_0 L = 2.5$, $\mathcal{L} = 1.727$.

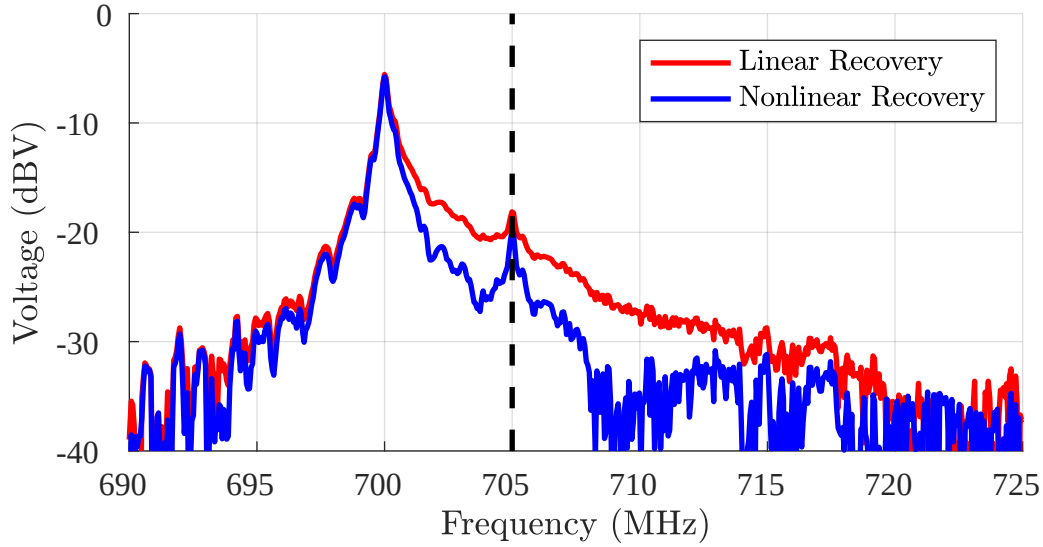

Figure 6.10: Linear and nonlinear recovery of two spectral holes, with $\alpha_0 L = 2.5$, $P_{\text{chirp}} = 7.15$ mW, $P_{\text{RF}} = 12$ dBm, $\mathcal{L} = 1.727$. One main hole at 700 MHz and a side hole at 705 MHz.

Chirp and Mixed Spectra

Chirped spectral patterns were also looked it, and it was observed that they, too, recover with the nonlinear algorithm. Fig. 6.11 displays data for both a single 5 MHz wide chirp as well as two 5 MHz chirps. Additionally, a more arbitrary spectral pattern was examined. A single tone was burned at various frequency locations around with a single 5 MHz wide chirp. The nonlinear recovery can be seen working on the spectra, as the tone moves past a chirp, in Fig. 6.12. The top and bottom left are for a tone set 3 MHz ahead of the chirp, with an RF power of 10 dBm. Thus, the nonlinear recovery can be seen working when the chirp sits in the tail. The top and bottom center are for a tone in the middle of the chirp, at -15 dBm. Finally, the top and bottom right show a tone at -15 dBm, within the nonlinear tail of the chirp.

Implementation of Nonlinear Algorithm

As a first step to implementing this algorithm into a previously working system, the new algorithm was added to an existing program. The option to change the nonlinear factor $\mathcal{L}$ was given as user defined control. A screen capture of this running in real-time is seen in Fig. 6.13. $\mathcal{L}$ is labeled as "Hilbert factor" in the figure.

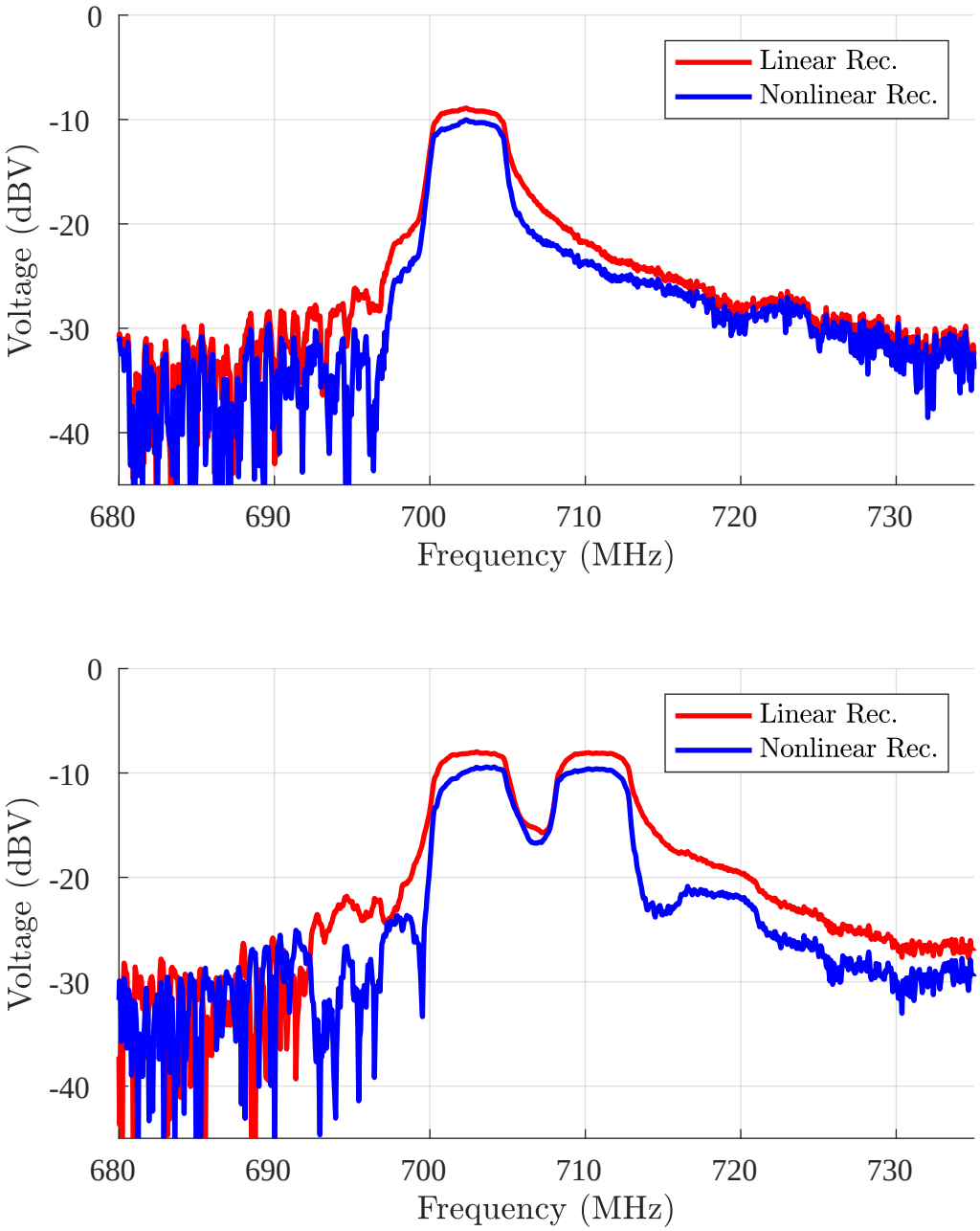

Figure 6.11: $\mathcal{L} = 1.727$, $\alpha_0 L = 2.5$, $P_{\text{chirp}} = 7.1$ mW. (Top) Log scaling of linear and nonlinear recovery of a single chirp spectra, 5 MHz wide with input voltage $V_{pp} = 1.2$ V. (Bottom) Log scaling of linear and nonlinear recovery of two chirp spectra, each 5 MHz wide with input voltage $V_{pp} = 2$ V.

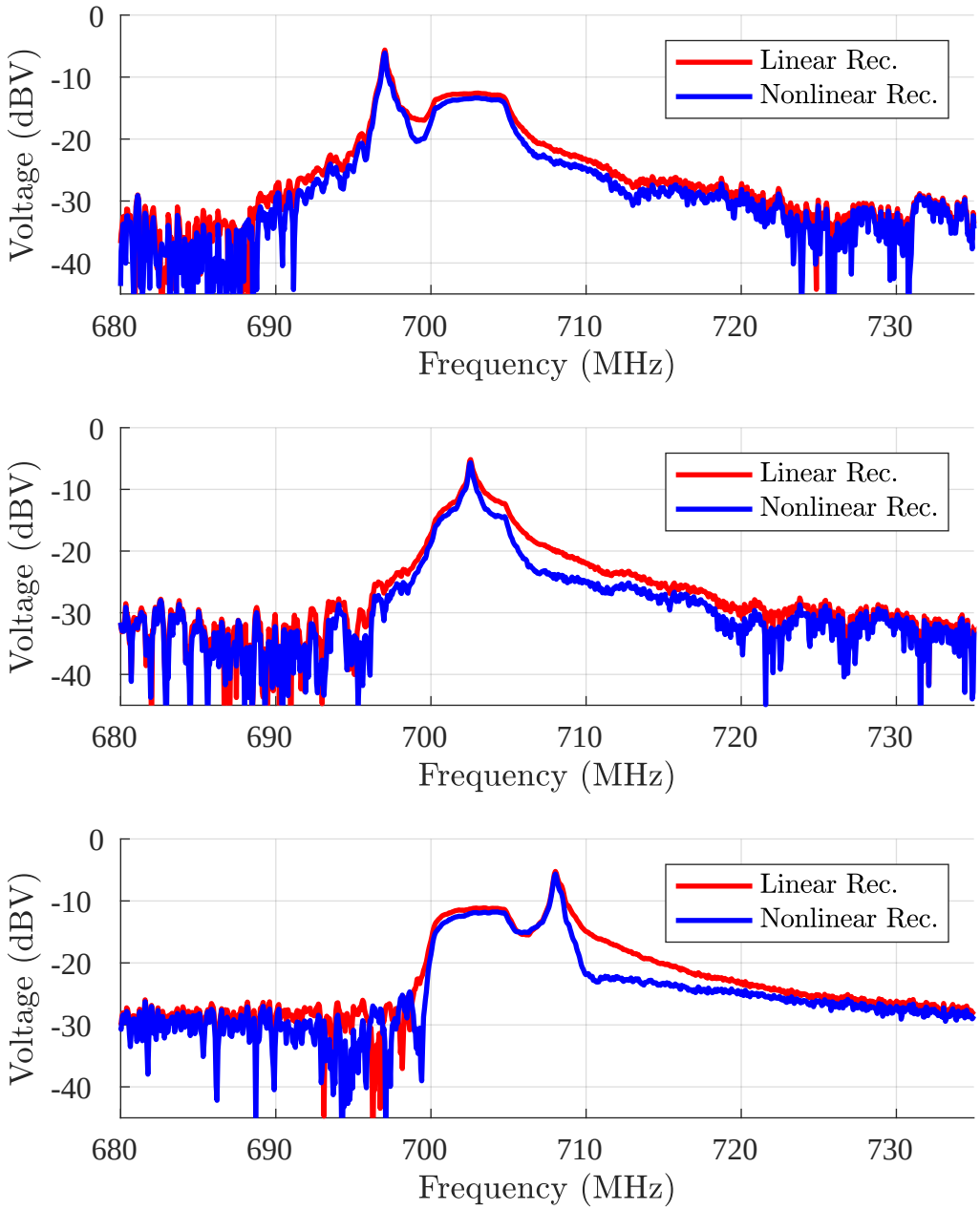

Figure 6.12: 10 dBm tone moving through a 5 MHz wide chirp with $V_{pp} = 1.995$ V. Linear and nonlinear recoveries are applied for $\alpha_0 L = 2.5$, $P_{\text{chirp}} = 7.15$, $\mathcal{L} = 1.727$.

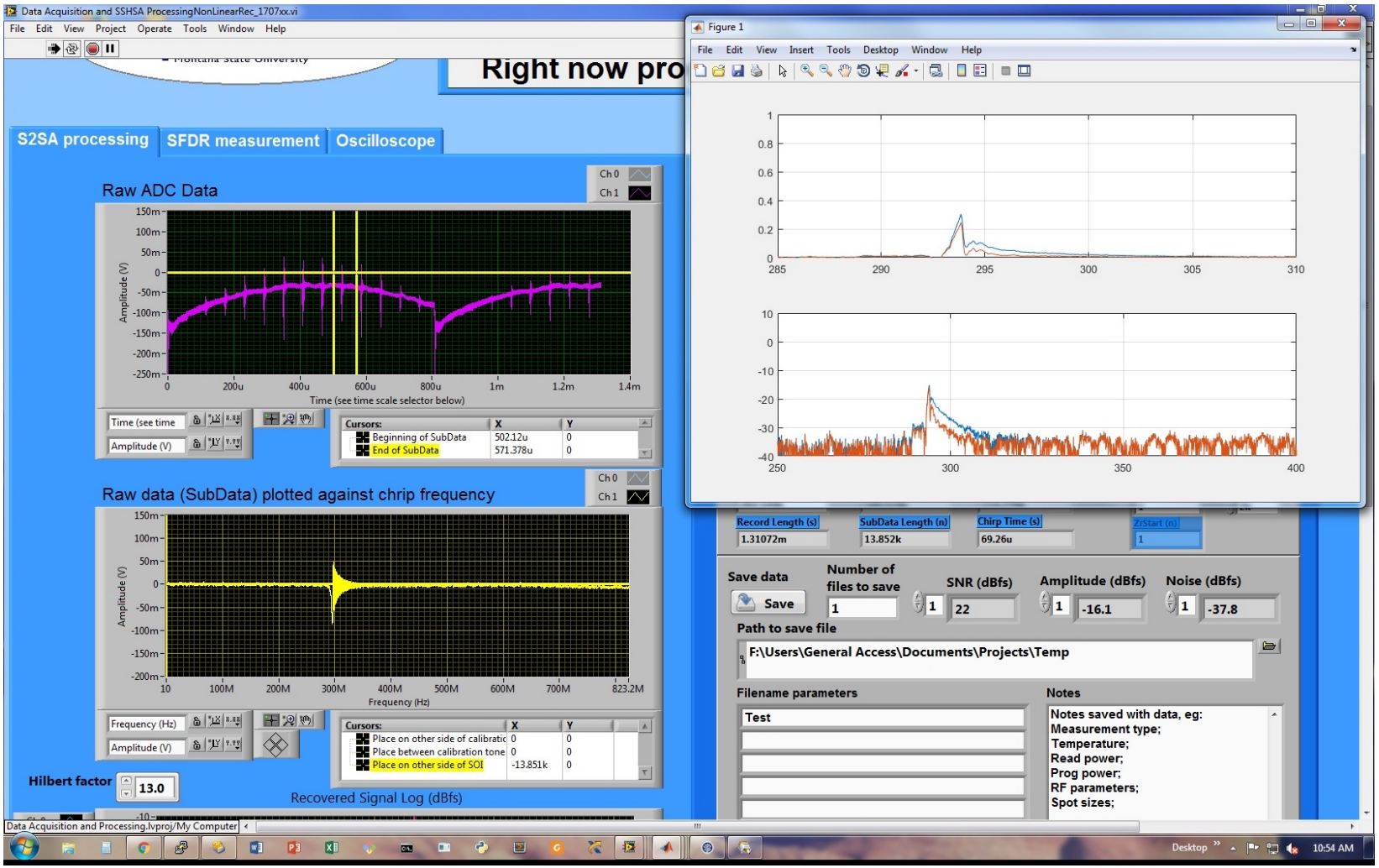

Figure 6.13: Screen capture of the nonlinear algorithm working in real-time. The window on the top-right is where the algorithm is being applied. The "Hilbert factor" seen on the bottom left, allows the user to change the $\mathcal{L}$-factor to whatever they need it to be. The top left and center graphs are the data being read in real-time, without any manipulation.

CONCLUSION

Linear spectral recovery of SOI's, readout with high frequency-chirped laser fields, has been in use for well over 10 years. It pushed the conventional limit of how fast you could scan over a material's bandwidth and still accurately resolve it. Yet, there was a limit on how far it could go. If the chirp rate and absorption length are high, while the holes burned are deep, then a nonlinearity appeared. This limited the dynamic range and total spectrum bandwidth that could be seen in the lifetime of the excited state ions. A higher order correction term was needed to fix this. In this thesis, a new algorithm that takes into account higher orders of the spectral recovery was presented as a means to accurately restore the spectrum. It was described in Ch. 3.

This new algorithm, called nonlinear recovery, enables faster chirp rates, at least as high as $\kappa \approx 12$ MHz/μs. Two Tm^{3+}: YAG crystals, with absorption lengths of $\alpha_0 L = 1.9$ and $\alpha_0 L = 2.5$ were used. These crystals have a material bandwidth of about 17 GHz. Many spectral waveforms we spectrally burned into the material's, and then scanned over. From the high chirp rate, their linearly recovered signals were highly distorted. The nonlinear recovery algorithm enabled their spectrum to be restored. Suppression of the nonlinear tails were observed, with up to 10 dB of spectral density recovered. The new algorithm was also installed on the system in Spectrum Lab at Montana State University, and shown to be running in real-time.

Remarks on $\mathcal{L}$-factor Characterization and Calibration

The new algorithm was found to depend on a scaling factor $\mathcal{L}$. It was required that this factor be characterized for the given optical system, before the new algorithm could be implemented. It was found to be dependent on input optical power and the

absorption length $\alpha_0 L$. There seemed to be separable dependence between the optical power and absorption length. So,

$$\mathcal{L}(P_{\text{chirp}}, \alpha_0 L) \propto \Pi(P_{\text{chirp}}) A(\alpha_0 L), \tag{7.1}$$

where Π and A would be functions that determine $\mathcal{L}$ for P_{chirp} and $\alpha_0 L$, separately. From the work shown in Ch.'s 4 and 6,

$$A(\alpha_0 L) \propto \frac{1}{e^{-\alpha_0 L}}, \tag{7.2}$$

and

$$\Pi(P_{\text{chirp}}) \propto \frac{1}{P_{\text{chirp}}}. \tag{7.3}$$

Therefore,

$$\mathcal{L}(P_{\text{chirp}}, \alpha_0 L) \propto \frac{1}{e^{-\alpha_0 L} P_{\text{chirp}}}. \tag{7.4}$$

Fortunately, if these values are constants in a system, one can fully determine $\mathcal{L}$. To do this, all one needs to do is set up their SHB spectrometer, and then send in a series of test signals that vary RF power, as was done in this research, while keeping the optical power at a constant value for a given material absorption length. Using the RMSE method, the value of $\mathcal{L}$ could be determined. In doing so, the $\mathcal{L}$-factor will have been properly calibrated. Furthermore, if the experimental setup remains unchanged then the $\mathcal{L}$-value will not need to be determined again.

Future Work

There are still avenues to explore for full characterization of the nonlinear factor. Its full response to $\alpha_0 L$ and its dependence on overlap would be required to construct an approximate expression for $\mathcal{L}$. However, this work demonstrated that a higher-order recovery can be implemented. More importantly, incorporating this new algorithm into commercial systems, like those of S2 Corporation in Bozeman, MT, will be the next step.

REFERENCES CITED

[1] FEDERAL COMMUNICATIONS COMMISSION OFFICE OF ENGINEERING AND TECHNOLOGY, "FCC ONLINE TABLE OF FREQUENCY ALLOCATIONS," Aug. 2017.

[2] NATIONAL TELECOMMUNICATIONS AND INFORMATION ADMINISTRATION OFFICE OF SPECTRUM MANAGEMENT, "FEDERAL SPECTRUM USE SUMMARY," June 2010.

[3] N. A. W. C. W. Division, *Electronic warfare & radar systems engineering handbook.* Place of publication not identified: Lulu Com, 2013. OCLC: 923875267.

[4] T. Chang, M. Tian, R. K. Mohan, C. Renner, K. D. Merkel, and W. R. Babbitt, "Recovery of spectral features readout with frequency-chirped laser fields," *Optics Letters*, vol. 30, p. 1129, May 2005.

[5] A. Amari, A. Walther, M. Sabooni, M. Huang, S. Kroll, M. Afzelius, I. Usmani, B. Lauritzen, N. Sangouard, H. de Riedmatten, and N. Gisin, "Towards an efficient atomic frequency comb quantum memory," *Journal of Luminescence*, vol. 130, pp. 1579–1585, Sept. 2010.

[6] C. Thiel, T. Bottger, and R. Cone, "Rare-earth-doped materials for applications in quantum information storage and signal processing," *Journal of Luminescence*, vol. 131, pp. 353–361, Mar. 2011.

[7] R. L. Cone, C. W. Thiel, Y. Sun, T. Bottger, and R. M. Macfarlane, "Rare-earth-doped materials with application to optical signal processing, quantum information science, and medical imaging technology," p. 82720E, Feb. 2012.

[8] T. Chang, R. K. Mohan, M. Tian, T. L. Harris, W. R. Babbitt, and K. D. Merkel, "Frequency-chirped readout of spatial-spectral absorption features," *Physical Review A*, vol. 70, Dec. 2004.

[9] M. Colice, "Broadband radio-frequency spectrum analysis in spectral-hole-burning media," *SPIE Newsroom*, 2006.

[10] R. Krishna Mohan, T. Chang, M. Tian, S. Bekker, A. Olson, C. Ostrander, A. Khallaayoun, C. Dollinger, W. Babbitt, Z. Cole, R. Reibel, K. Merkel, Y. Sun, R. Cone, F. Schlottau, and K. Wagner, "Ultra-wideband spectral analysis using S2 technology," *Journal of Luminescence*, vol. 127, pp. 116–128, Nov. 2007.

[11] V. Lavielle, I. Lorger, J.-L. Le Gouet, S. Tonda, and D. Dolfi, "Wideband versatile radio-frequency spectrum analyzer," *Optics Letters*, vol. 28, p. 384, Mar. 2003.

[12] V. Lavielle, F. De Seze, I. Lorgere, and J.-L. Le Gouet, "Wideband radio frequency spectrum analyzer: improved design and experimental results," *Journal of Luminescence*, vol. 107, pp. 75–89, May 2004.

[13] L. Menager, I. Lorgere, J.-L. Le Gouet, D. Dolfi, and J.-P. Huignard, "Demonstration of a radio-frequency spectrum analyzer based on spectral hole burning," *Optics Letters*, vol. 26, p. 1245, Aug. 2001.

[14] R. Mohan, Z. Cole, R. Reibel, Teijun Chang, K. Merkel, W. Babbit, M. Colice, F. Schlottau, and K. Wagner, "Microwave spectral analysis using optical spectral hole burning," pp. 24–27, IEEE, 2004.

[15] M. Colice, F. Schlottau, K. Wagner, R. K. Mohan, W. R. Babbitt, I. Lorgere, and J.-L. Le Gouet, "RF spectrum analysis in spectral hole burning media," p. 132, Oct. 2004.

[16] G. Gorju, A. Chauve, V. Crozatier, I. Lorgere, J. L. Le Gouet, and F. Bretenaker, "10-GHz Bandwidth RF Spectral Analyzer with MHz Resolution Based on Holography in Tm3+: YAG," pp. 1–4, IEEE, Oct. 2006.

[17] K. Merkel, Z. Cole, and W. Babbitt, "Signal correlator with programmable variable time delay based on optical coherent transients," *Journal of Luminescence*, vol. 86, pp. 375–382, Apr. 2000.

[18] C. W. Thiel, R. L. Cone, and T. Bottger, "Laser linewidth narrowing using transient spectral hole burning," *Journal of Luminescence*, vol. 152, pp. 84–87, Aug. 2014.

[19] W. R. Babbitt, Z. W. Barber, S. H. Bekker, M. D. Chase, C. Harrington, K. D. Merkel, R. K. Mohan, T. Sharpe, C. R. Stiffler, A. S. Traxinger, and A. J. Woidtke, "From spectral holeburning memory to spatial-spectral microwave signal processing," *Laser Physics*, vol. 24, p. 094002, Sept. 2014.

[20] K. D. Merkel, W. Babbitt, Z. W. Barber, and S. H. Bekker, "Extreme Wideband Photonic Cueing Receiver for Electronic Support: CSWaP and Fidelity Comparisons to an All-Digital Alternative," *Proc. GOMACTech Conf.*, pp. 11–14, 2013.

[21] "Measuring with Modern Spectrum Analyzers Educational Note," Feb. 2013.

[22] L. Allen and J. H. Eberly, *Optical resonance and two-level atoms*. New York: Dover, 1987.

[23] A. Renn, U. P. Wild, and A. Rebane, "Multidimensional Holography by Persistent Spectral Hole Burning," *The Journal of Physical Chemistry A*, vol. 106, pp. 3045–3060, Apr. 2002.

[24] J.-L. Le Gouet, I. Lorgere, F. Bretenaker, V. Lavielle, and V. Crozatier, "Atomic spectral analyzers for radio frequency signal processing," vol. 2, pp. 931–932, IEEE, 2004.

[25] I. Lorgere, V. Crozatier, G. Gorju, F. Bretenaker, and J.-L. Le Gouet, "Radio-frequency spectrum analyzers based on rare earth ion doped crystals," *Applied Physics B*, vol. 84, pp. 653–657, Sept. 2006.

[26] Aaron Dalbey and W. R. Babbitt, "Spatial-Spectral Hole Burning Readout Recovery Algorithm (by private communication)," Apr. 2010.

[27] M. Fox, *Quantum optics: an introduction*. No. 15 in Oxford master series in physics, Oxford ; New York: Oxford University Press, 2006.

[28] T. Bottger, C. W. Thiel, Y. Sun, and R. L. Cone, "Optical decoherence and spectral diffusion at 1.5 m in Er 3 + : Y 2 SiO 5 versus magnetic field, temperature, and Er 3 + concentration," *Physical Review B*, vol. 73, Feb. 2006.

[29] R. M. MacFarlane, "A study of excited state dynamics of rare earth ions in solids by coherent transients and spectral holeburning," *Journal of Luminescence*, vol. 40-41, pp. 3–6, Feb. 1988.

[30] A. E. Siegman, *Lasers*. Mill Valley, Calif: Univ. Science Books, 1986. OCLC: 14525287.

[31] P. R. Berman and V. S. Malinovsky, *Principles of laser spectroscopy and quantum optics*. Princeton, N.J: Princeton University Press, 2011. OCLC: ocn587249002.

[32] L. Mandel and E. Wolf, *Optical coherence and quantum optics*. Cambridge ; New York: Cambridge University Press, 1995.

[33] J. J. Sakurai and J. Napolitano, *Modern quantum mechanics*. Boston: Addison-Wesley, 2nd ed ed., 2011.

[34] J. I. Steinfeld, ed., *Laser and Coherence Spectroscopy*. Boston, MA: Springer US, 1978. DOI: 10.1007/978-1-4684-2352-5.

[35] Y. Sun, G. M. Wang, R. L. Cone, R. W. Equall, and M. J. M. Leask, "Symmetry considerations regarding light propagation and light polarization for coherent interactions with ions in crystals," *Physical Review B*, vol. 62, pp. 15443–15451, Dec. 2000.

[36] B. E. A. Saleh and M. C. Teich, *Fundamentals of photonics*. Wiley series in pure and applied optics, New York: Wiley, 1991.

[37] A. Yariv, *Quantum electronics*. New York: Wiley, 3rd ed ed., 1989.

[38] K. F. Riley, M. P. Hobson, and S. J. Bence, *Mathematical methods for physics and engineering*. Cambridge ; New York: Cambridge University Press, 3rd ed ed., 2006. OCLC: ocm62532900.

[39] R. V. Hogg and E. A. Tanis, *Probability and statistical inference*. Upper Saddle River, NJ: Prentice Hall, 8th ed ed., 2010.

[40] R. W. Boyd, *Nonlinear optics*. Amsterdam ; Boston: Academic Press, 3rd ed ed., 2008.

[41] D. Colton and R. Kress, *Inverse acoustic and electromagnetic scattering theory*. No. 93 in Applied mathematical sciences, New York: Springer, 3. ed ed., 2013. OCLC: 819723227.

[42] M. Abramowitz and I. A. Stegun, eds., *Handbook of mathematical functions: with formulas, graphs, and mathematical tables*. Dover books on mathematics, New York, NY: Dover Publ, 9. dover print ed., 2013. OCLC: 935935300.

[43] NKT Photonics, "Single frequency DFB fiber lasers - LASERS & FIBERS," Sept. 2017.

[44] G. K. Wertheim, M. A. Butler, K. W. West, and D. N. E. Buchanan, "Determination of the Gaussian and Lorentzian content of experimental line shapes," *Review of Scientific Instruments*, vol. 45, pp. 1369–1371, Nov. 1974.

APPENDICES

APPENDIX A

NONLINEAR RECOVERY CODE

```
% This program simulates a single Lorentzian hole, and makes
    various plots.

clear, clc, clf, close all
set(groot,'defaultLineLineWidth',2,'defaultAxesFontSize',12,'
    defaultAxesFontName','timesnewroman','defaulttextinterpreter',
    'latex')
x0 = 8;
y0 = 5;
width = 6;
height = 3;

%% Setting up the chirp
kap = 12e12;

    % Chirp rate
sr = 0.0068239900e6;
                                                        % Freq
    step size of chirp
tmax = 800e-6;
                                                              %
     Duration of chirp
p = 30;

    % A scaling factor
n = 195072;

    % The number of points one wishes to downsample to later
q = n*p*sr/2/tmax/kap;
                                                    % Another
     scaling factor
fsc = q*2*kap/sr;
                                                           %
    Sampling rate for the points to be used before downsampling
N = tmax*fsc;

    % Number of points to be used before downsampling
t = (1:N)/fsc;
                                                              %
     Timing array

% Super Gaussian to prevent aliasing
pow = 30;
num = t-N/fsc/2;
denom = N/fsc/log(2)/3.1;
```

```
ip = 1;

    % Input chirp power in mW
E0 = sqrt(ip)*exp(-((fsc*t/N-0.5)*log(2^pi)).^pow);
f0 = 0;
phi_l = 2*pi*f0*t;
phi_q = pi*kap*t.^2;
E = E0.*exp(1j*(phi_l+phi_q));
                                                    % Chirp field

%% Programming spectral hole

f = f0 + linspace(0, tmax*kap, N);
                                                % Frequency array
    defined in terms of carrier and chirp bandwidth

fh = 1000*1e6;
                                                                    %
     Location of hole
holeWidth = 1e6;
                                                                  %
    Hole Width
holeDepth = 0.3;
                                                                  %
    Hole Depth
hole = holeDepth./(1+((f-fh)/(holeWidth/2)).^2);
                                % Lorentzian absorption shape

alpha0L = 4;

    % Peak absorbance of crystal material
alpha = alpha0L*(1-hole);
                                                        % Absorbance
     in terms of hole described above
alphaRef = alpha0L*ones(1,length(alpha));
                                        % Reference beam absorbance
gamma = hilbert(alpha);
                                                          % Getting
    the aborption and dispersion from the hole
gamma0 = hilbert(alphaRef);
                                                      % Same for
    reference

absorb = 1 - exp(-alpha);
                                                        % Absorption
```

```
absorbref = 1-exp(-alphaRef);
                                                    % Background
    Absorption
hole = absorbref-absorb;
                                                        % Spectral
    Hole
hole = hole+rand(1,floor(N))*0.05e-4;
                                                % Adding noise to the
    signal

%% Detected Power

Ef = fft(E);

   % Converting to frequency domain
trans = exp(-conj(gamma)/2);
                                                    % Defining the
    transfer function
Et = ifft(trans.*Ef);
                                                                %
    Getting the output of the system
P = Et.*conj(Et);
                                                                    %
    Power spectrum of the output
trans0 = exp(-conj(gamma0)/2);
                                                % Same thing for
    the reference beam
Et0 = ifft(trans0.*Ef);
P0 = Et0.*conj(Et0);
Pdet = P-P0;

   % This should be the ringout signal
Pdet = Pdet+rand(1,floor(N))*0.05e-4;
                                                % Adding noise to the
    signal


%% Normalizating to 0-1 scale.

maxhole = max(hole);
hole = hole/maxhole;
Pdet = Pdet/maxhole;

%% Linear recovery
```

```
Prec = recovery4(N,tmax,kap,Pdet,f0);
                                        % Apply recovery


%% Pfid

Pfid = recovery4(N,tmax,kap,abs(hilbert(Pdet)).^2,f0);

%% Downsampling of arrays
hole = downsample(hole, p);
Pdet = downsample(Pdet, p);
Prec = downsample(Prec, p);
Pfid = downsample(Pfid, p);


%% Frequency Array stuff

convfac = fsc^2/N/kap;
tkapfac = 1/convfac;
f2 = t*kap*tkapfac;
                                                        % New
    frequency array
f2 = downsample(f2,p);
f2 = f2*1e-6;
f2 = f2 - 9600;
f = f*1e-6;

    % Conversion of frequency array to MHz
f = downsample(f,p);
fh = fh*1e-6;


%% Nonlinear recovery algorithm

fac = linspace(0,1,1000);
Pnew2 = zeros(length(fac),length(Pdet));

for i = 1:length(fac)
     i
     Pnew2(i,:) = Prec - Pfid*fac(i);
end

% RMSE
rmse = zeros(1,length(fac));
frlow = find(f2>=fh-15 & f2<fh-1);
```

```
frlow = frlow(1:end-1);
frhigh = find(f2>fh+1 & f2<=fh+15);

for i = 1:length(fac)
    rmse(i) = sqrt(sum((Pnew2(i,fliplr(frlow))-Pnew2(i,frhigh))
        .^2)/(length(Pnew2(i,frhigh))-1));
end
[mins, j] = min(rmse);
fac(j)

% Pnl
Pnew = Prec-Pfid*fac(j);


%% Normalization

fr = find(f>=(fh-100) & f<=(fh+100));
fr2 = find(f2>=(fh-100) & f2<=(fh+100));
nor1 = trapz(f(fr),hole(fr))/trapz(f2(fr2),Prec(fr2));
nor2 = trapz(f(fr),hole(fr))/trapz(f2(fr2),Pnew(fr2));
Prec = Prec*nor1;
Pnew = Pnew*nor2;


%% Plotting

figure(1)
hold on
plot(f, 10*log10(hole), 'k')
plot(f2, 10*log10(Prec), 'r')
plot(f2, 10*log10(Pnew), 'b')
xticks([fh-15 fh-10 fh-5 fh, fh+5 fh+10 fh+15 fh+20 fh+25])
xticklabels({'-15' '-10','-5' '\nu_H', '+5' '+10', '+15' '+20'  '
    +25'})
xlim([min(xticks) max(xticks)])
ylim([-40 0])
xlabel('Frequency (MHz)')
ylabel('Log of Amplitude (A. U.)');
h = legend('Nonlinear Recovery', 'Linear Recovery','Nonlinear
    Recovery');
set(h,'Interpreter','latex')
grid on
set(figure(1),'units','inches','Position',[x0,y0,width,height],'
    PaperPositionMode','Auto','PaperUnits','Inches','PaperSize',[
    width, height]);
```

APPENDIX B

LINEAR RECOVERY ALGORITHM

```
function out = recovery4(N, tmax, kap, data, ws)
% N data points, length of sample  time in seconds, Kappa (burned
% holebandwidth over the width of the pulse), Data being
    recovered, unknown(zero for now))

dt = tmax/N;                                                    %
    time step size as defined by input data
freq = (1/dt)*((0:N-1)-N/2)/N;                                  %
    Frequency, N points long from -1/2 to (N-1)/2N

data = fft(data);
data = fftshift(data);
recovery = exp(-1i*pi*(2*ws*freq-sign(freq).*freq.^2)/kap);     %
    Recovery defined
data = data.* recovery;                                         %
    Applying recovery
data = ifft(fftshift(data));                                    %
    Return to time domain
out = real(data);
```